Geostrophic dynamics at surfaces in the atmosphere and ocean

by

Ross Tulloch

A dissertation submitted in partial fulfillment

of the requirements for the degree of

Doctor of Philosophy

Department of Mathematics

New York University

January 2009

Shafer Smith — Advisor

Acknowledgements

This dissertation would not have been possible without the help and support of many people. First and foremost, I would like to thank my advisor, Shafer Smith. He has been an excellent teacher and mentor, and I am indebted to him for much of my understanding of geophysical fluid dynamics.

I would also like to thank a number of people whose advice has helped me along the way. Thanks to John Marshall for suggesting the Rossby wave problem in Chapter 5, providing observational data and leading that project to completion. Thanks also to Glenn Flierl, Guillaume Lapeyre and Rob Scott for interesting and inciteful discussions on surface QG dynamics in the ocean, and to David Muraki whose excellent teaching introduced me to fluid dynamics.

Time would have passed much slower were it not for my fellow CAOS and Courant students. In particular I would like to thank my officemates Paul Wright, Hantaek Bae, and Punkaj Vishe for being so jovial, and students who were both a lot of fun and a lot of help: Tom Alberts, Ethan Atkins, Christof König Beatty, Daniel Goldberg, Paul Hand, Alex Hasha, Al Momin, Caroline Muller and Daniel Shaevitz.

Without technical and administrative support this thesis would have been much more difficult. Thanks to Andrew "Destructo" Case and Joseph Hargitai for answering almost every one of my CIMS and HPC system administration questions, and to Ross Wightman for Windows support.

Finally, I would like to thank my family, who have supported me throughout my studies and enabled me to become who I am today.

Abstract

Observed dynamics near bounding upper surfaces in the atmosphere and ocean are interpreted in terms of quasi-geostrophic theory. The quasi-geostrophic equations consist of advection of linearized potential vorticity coupled with advection of temperature at the upper and lower bounding surfaces. We show that the standard vertical finite difference formulation of 3D quasi-geostrophic flow accurately represents the flow only down to a critical horizontal scale that decreases with vertical grid spacing. To overcome this constraint, we derive a surface-modal formulation which accurately and efficiently captures both the surface dynamics due to temperature anomalies on the upper and lower boundaries, and the interior dynamics due to potential vorticity anomalies, without the need for high vertical resolution.

In the atmosphere, the horizontal wavenumber spectra of wind and temperature near the tropopause have a steep -3 slope at synoptic scales and a shallow -5/3 slope at mesoscales, with a smooth transition between the two regimes from 800km to 200km. We demonstrate that when the surface temperature anomalies are resolved, quasi-geostrophic flow driven by baroclinic instability exhibits such a transition near the tropopause. The horizontal scale of transition between -3 and -5/3 slopes depends on the relative magnitudes of the mean surface temperature gradient and the mean potential vorticity gradient.

In the ocean, sea surface height anomalies measured by satellite altimetry ex-

hibit shallower spectral slopes than quasi-geostrophic theory predicts, and faster than expected westward phase propagation of sea surface height in the midlatitudes. We argue that, in some regions, the shallow spectral slopes are due to surface quasi-geostrophic dynamics, and that the westward phase propagation in the midlatitudes is indicative of a transition from a linear Rossby wave regime in the tropics to a nonlinear turbulent regime in the midlatitudes.

Contents

List of Figures

Chapter 1

Introduction

The theoretical foundations of much of geophysical fluid dynamics (GFD) were laid in the mid-20^{th} century, yet even today there are many real world observations which have proven difficult to explain using the classic GFD theories. The shape of the observed energy spectra in the atmosphere and ocean, as well as observations of westward phase propagation in the ocean are examples that will be discussed here. In each of these examples the classical theories explain only part of what is observed. We are still lacking a clear explanation of how turbulent eddies redistribute energy across spatial scales, and how waves interact with turbulence.

In the atmosphere the well known Nastrom and Gage (1985) energy spectrum, computed from data collected by commercial aircraft flying near the tropopause, obeys the classic geostrophic turbulence prediction of Charney (1971) for quasi-two dimensional (2D) flows at synoptic scales ($\gtrsim$ 1000km). However the spectrum deviates from Charney's prediction in the mesoscales, with the departure from theory occurring at a larger scale than expected ($\approx$ 800km). Therefore either Charney's theory of geostrophic turbulence is incomplete or ageostrophic dynamics

are more important than previously thought. Here we investigate the extent to which geostrophic theory can be supplemented with surface geostrophic dynamics to recover the observed spectrum.

The ocean is more difficult to observe than the atmosphere because it is less accessible and the characteristic scales are significantly smaller and slower. Observations of sea surface height (SSH) have been available since the the 1980's, but it has been difficult to get an consistent record of SSH energy spectrum. While the atmospheric spectrum of Nastrom and Gage (1985) has been validated in independent studies using independent measurements (Lindborg, 1999), the shape of the oceanic SSH spectrum appears to vary between studies (see Stammer and Böning, 1992; Stammer, 1997; Le Traon, 1993; Le Traon et al., 2008). The reason is likely a problem of limited spatial resolution. In the atmospheric midlatitudes the deformation scale is of the order of 1000-2000km and noise in aircraft measurements begins to dominate at around 2km so there is about 3 decades of bandwidth from which to measure spectral slopes. However in the oceanic midlatitudes the deformation scale is of the 100-200km and noise in satellite observations is apparent at scales as large as 100km, so the spectral bandwidth is limited. Nevertheless, observations by Le Traon et al. (2008) and numerical studies by Klein et al. (2008) and Lapeyre (2008) argue that near the ocean's surface the kinetic energy (KE) spectra has a shallow spectral slope (-5/3) near and below the deformation scale. Here we evaluate the hypothesis that surface quasi-geostrophic (SQG) dynamics dominate quasi-geostrophic (QG) dynamics at the mesoscales near the surface using a simple model that contains both.

Another observation that is only partly explained by classical theory is the westward propagation of SSH anomalies. Chelton and Schlax (1996) observed that

at low latitudes SSH anomalies typically propagate at the phase speed predicted for long, first baroclinic Rossby waves. However at higher latitudes the observed phase propagation is about twice what the classic theory predicts. The implication is that these higher latitude anomalies are either nonlinear eddies, as proposed by Chelton et al. (2007), or they are linear Rossby waves under the influence of mean flow and topography, which was proposed in a series of papers by Killworth and Blundell (2003, 2005); Maharaj et al. (2007). Here the linear proposal is tested using new surface observations and a new ocean atlas (Forget, 2008).

The rest of this chapter gives some basic background to central GFD topics that later chapters will build upon, such as baroclinic instability and geostrophic scaling, followed by an overview of the other chapters. Chapter 2 on our model formulation and simplified models contains material from Tulloch and Smith (2006) and Tulloch and Smith (2008a). Chapter 3 on the atmospheric energy spectrum is comprised mainly from material in Tulloch and Smith (2008b). Chapter 5 on the westward propagation of SSH anomalies is from Tulloch et al. (2008).

1.1 Baroclinic instability

The atmosphere and ocean are primarily energized by sunlight and tides. Tidal forcing produces fast internal waves that must be dissipated through mixing. While tides are the second largest energy source, and probably play an important role in the general circulation, we neglect them here. Heating by the sun creates a massive reserve of potential energy in both the atmosphere and ocean. Lorenz (1955) noted that only a small amount (less than one percent in the atmosphere) of this potential energy, that which is not due to vertical stratification,

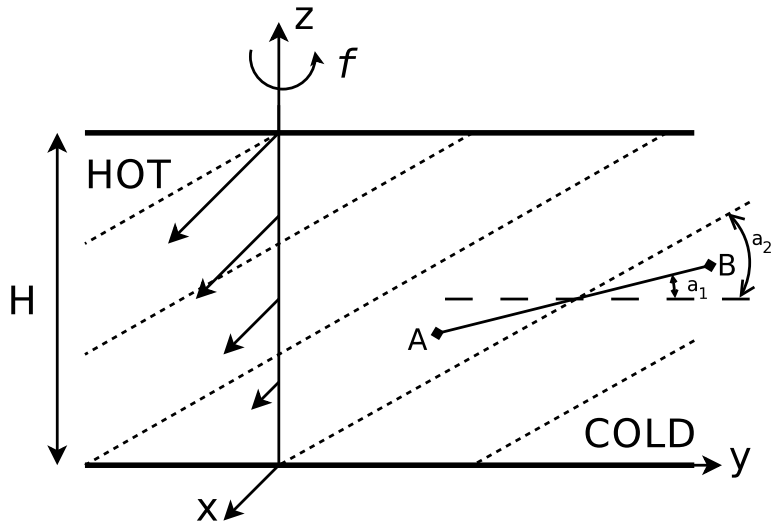

Figure 1.1: Mean state giving rise to baroclinic instability. Isotherms (dashed lines) indicate that temperature increases upwards and decreases polewards ($\hat{\boldsymbol{y}}$ direction), in thermal wind balance with a zonal velocity ($\hat{\boldsymbol{x}}$ direction) increasing upwards. Substituting parcel A with B will result in a net loss of potential energy since parcel A is warmer than parcel B. This figure was drawn based on Figure 1 of Hart (1979).

is available to be converted into kinetic energy. He further argued that the total available potential energy (APE) is generally about *ten times* larger than the total kinetic energy in the atmosphere, and that the conversion between the two is the main driver of the general circulation. Similarly, Gill et al. (1974) argued that the APE is of order *one thousand times* larger than the kinetic energy in the ocean.

Baroclinic instability, illustrated in Figure 1.1, is the dominant mechanism by which mean APE is converted into eddy APE and then eddy kinetic energy. The eddy KE then drives the general circulation in the atmosphere, *i.e.,* mean kinetic energy (Lorenz, 1955). However, less is known about the baroclinic life cycle of oceanic eddies, and the extent to which they drive the general circulation is an open

problem (see *e.g.,* Wunsch and Ferrari, 2004). The equator-to-pole temperature gradient results in slanted isotherms (dashed lines) in the atmosphere (or isopycnals in the ocean) that is steady in time. Hydrostatic and geostrophic balance then implies that this slanting is balanced by a zonal velocity shear (solid arrows). This sheared state is unstable to perturbations of the form shown, whereby if a parcel A in a warm region and a parcel B in a cool region are substituted, the center of mass decreases, which results in a net loss of potential energy. This loss of potential energy is balanced by unstable wave growth, which leads to the generation of eddies. The eddies flux heat meridionally and tend to reduce the slope of the isotherms.

Charney (1947) and Eady (1949) were the first to develop models of baroclinic instability in the atmosphere. The "Eady model" is the more analytically tractable of the two, consisting of an f-plane atmosphere ($\beta = 0$) with uniform stratification and velocity shear, bounded between rigid surfaces separated by a depth H. Eady's model develops a large scale instability that requires interaction between disturbances at the upper and lower boundaries. The "Charney model" allows for a mean potential vorticity (PV) gradient in the interior of the fluid via differential rotation ($\beta \neq 0$) and no upper boundary is required. The instability that develops is between boundary disturbances and the interior PV gradient, so it can be both large or small scale. Two further models of baroclinic instability will be considered here: those due to Phillips (1951) and Green (1960). The "Phillips model" is a two layer model that is a hybrid of the Eady and Charney models, but it allows for another type of baroclinic instability which occurs within the fluid and is due to sign changes in the PV gradient. The "Green model" is a generalization of the Phillips model to the multi-layer case which, in addition to the instabilities of the

aforementioned models, admits weakly unstable modes of large horizontal scale called "Green modes".

Baroclinic instability will play an integral part in much of this thesis. Many of the models discussed contain a large scale, time independent, baroclinically unstable "mean" velocity profile as the sole forcing. The equations considered here will all be quasi-geostrophic (see below), so the mean forcing can be thought of as obeying the appropriate equations of a larger spatial scale and slower time scale set of equations, such as the planetary geostrophic equations (Pedlosky, 1984).

1.2 Quasi-geostrophic scaling and equations

We take as our starting point the incompressible, hydrostatic, Boussinesq equations on a β-plane in the absence of external forcing or dissipation

$$\partial_t \mathbf{u} + \mathbf{u} \cdot \nabla \mathbf{u} + f\hat{\boldsymbol{z}} \times \mathbf{u} = -\nabla \Phi, \tag{1.1a}$$

$$\partial_t b + \mathbf{u} \cdot \nabla b + N^2 w = 0, \tag{1.1b}$$

$$\nabla \cdot \mathbf{u} + \partial_z w = 0, \tag{1.1c}$$

$$b = \partial_z \Phi, \tag{1.1d}$$

where $\nabla = \hat{\boldsymbol{x}}\partial_x + \hat{\boldsymbol{y}}\partial_y$, $\mathbf{u} = u\hat{\boldsymbol{x}} + v\hat{\boldsymbol{y}}$ is the horizontal velocity, w is vertical velocity, f is the Coriolis frequency, Φ is the geopotential, b is the buoyancy, and N^2 is the stratification, which is also known as the buoyancy frequency (or Brunt-Väisälä frequency). Equations (1.1a) and (1.1b) are statements of conservation of horizontal momentum and thermodynamic tracer, Equation (1.1c) is a kinematic continuity condition and (1.1d) is hydrostatic balance. Note that these equations

better approximate the ocean than the atmosphere because in the atmosphere the density scale height is of the same order as the dynamical scale height $\mathcal{H}$, whereas in the ocean the density scale height is two orders of magnitude larger (Spiegel and Veronis, 1960).

Geostrophic scaling implies $\Phi \sim f\mathcal{U}\mathcal{L}$, where $\mathcal{L}$ is the horizontal length scale, $\mathcal{U}$ is the horizontal velocity scale. In addition hydrostatic balance implies $b \sim f\mathcal{U}\mathcal{L}/\mathcal{H}$ where $\mathcal{H}$ is the height scale[1]. Quasi-geostrophic scaling then makes the following further assumptions about the flow:

1. an advective time scale $t \sim \mathcal{L}/\mathcal{U}$,

2. small Rossby number: $Ro = \mathcal{U}/(f\mathcal{L}) \ll 1$,

3. the horizontal scale is on the order of the deformation scale $L_d = N\mathcal{H}/f$, so $Ro\mathcal{L}^2/L_d^2 = \mathcal{O}(Ro)$, which when combined with hydrostatic balance implies that variations in stratification are small compared to the background stratification,

4. the β-plane approximation $\beta\mathcal{L}/f \sim \mathcal{O}(Ro)$, where β is the meridional gradient of the Coriolis frequency,

see Vallis (2006) or Pedlosky (1987) for details, or Pedlosky (1984); Vallis (1996); Muraki et al. (1999) for mathematically rigorous derivations using asymptotic expansions in Rossby number. The QG approximation was first conceived by Charney (1948) and it made numerical weather prediction possible because it effectively filters out fast, "unbalanced" wave motions. Since QG dynamics are soley controlled by the potential vorticity and higher Rossby order terms are discarded

[1]Script letters such as $\mathcal{H}, \mathcal{U}$ and $\mathcal{L}$ denote scales, while regular font letters such as f, N denote physical parameters.

($Ro \to 0$) they are often called "balanced", or the "slow manifold". However Boussinesq flows that are initially balanced have been shown to remain dominated by balanced motion for Rossby numbers up to $\mathcal{O}(1)$ when $N/f \gg 1$ (McKiver and Dritschel, 2008). Similarly, Vanneste and Yavneh (2004) argued that spontaneous generation of inertia-gravity waves by a balanced Boussinesq flow is exponentially small when at small Rossby number $Ro \ll 1$, so QG is an accurate approximation.

The equation for advection of quasi-geostrophic potential vorticity (QGPV) is obtained by cross differentiating the horizontal momentum equations, to eliminate the geopotential, then inserting the thermodynamic equation and equating $\mathcal{O}(Ro)$ terms

$$\partial_t q + J(\psi, q) + \beta \partial_x \psi = 0, \tag{1.2}$$

where $J(A, B) = \partial_x A \partial_y B - \partial_y A \partial_x B$ is the two dimensional Jacobian operator. The geostrophic streamfunction $\psi(x, y, z, t)$ is defined such that $\mathbf{u} = \nabla^\perp \psi \equiv -\partial_y \psi \hat{\boldsymbol{x}} + \partial_x \psi \hat{\boldsymbol{y}}$, and the QGPV[2] is defined as

$$q = \nabla^2 \psi + \Gamma \psi, \quad \text{where} \quad \Gamma \equiv \partial_z (f^2/N^2) \partial_z \tag{1.3}$$

is the vortex stretching operator.

We introduce into the QG equations a larger scale, steady, baroclinically unstable mean flow

$$\mathbf{U} = U(z)\hat{\boldsymbol{x}} + V(z)\hat{\boldsymbol{y}} = \hat{\boldsymbol{z}} \times \nabla \Psi, \quad W = 0,$$

[2]QGPV is also known as pseudo-potential vorticity because it is is an approximation to the Ertel potential vorticity (Ertel, 1942; Ertel and Rossby, 1949), which is conserved by the full Boussinesq equations (see Hoskins et al., 1985).

which, in an asymptotic sense, can be considered slowly varying solutions to the planetary geostrophic equations (Pedlosky, 1984). Such a mean flow gives rise to a mean QGPV gradient

$$\nabla Q = \Gamma V \hat{\boldsymbol{x}} + (\beta - \Gamma U)\hat{\boldsymbol{y}}. \tag{1.4}$$

This forcing will cause unabated energy growth if it is not damped, which is undesirable since we want to compute steady state flow statistics. Hence we also include an energy dissipation mechanism that will remove energy from the system without significantly changing its dynamics. The simplest such mechanism is bottom Ekman friction, which results in linear vorticity drag[3]. Ekman friction is rationalized by assuming there is an Ekman layer at the bottom of the fluid, which for a flat bottom gives an Ekman pumping proportional to the relative vorticity

$$w(z_B) = \delta_{Ek} \nabla^2 \psi(z_B).$$

Further assuming a rigid upper lid, so that $w = 0$ in Equation (1.1b), the QGPV equation and upper and lower boundary conditions (with mean baroclinic wind and Ekman drag) are

$$\partial_t q + J(\psi, q) + \mathbf{U} \cdot \nabla q + \mathbf{u} \cdot \nabla Q = 0, \qquad z_B < z < z_T, \tag{1.5a}$$

$$\partial_t \theta + J(\psi, \theta) + \mathbf{U} \cdot \nabla \theta + \mathbf{u} \cdot \nabla \Theta = 0, \qquad z = z_T, \tag{1.5b}$$

$$\partial_t \theta + J(\psi, \theta) + \mathbf{U} \cdot \nabla \theta + \mathbf{u} \cdot \nabla \Theta = -r \nabla^2 \psi, \qquad z = z_B, \tag{1.5c}$$

[3]More physical dissipations exist, such as quadratic drag, which is less sensitive model parameters (Grianik et al., 2004; Arbic and Scott, 2008). However, the effects of linear drag are better understood than quadratic drag (see *e.g.,* Thompson and Young, 2006; Smith and Vallis, 2002).

where θ is the buoyancy rescaled by the local Coriolis frequency $\theta \equiv b/f$, $\nabla\Theta$ is the mean thermodynamic gradient which is in thermal wind balance with the mean velocity

$$\nabla\Theta = \partial_z V\hat{\boldsymbol{x}} - \partial_z U\hat{\boldsymbol{y}}, \tag{1.6}$$

and z_T and z_B denote the top and bottom of the fluid[4].

These thermal boundary conditions result in Neumann boundary conditions for the elliptic boundary value problem for the streamfunction

$$q = \nabla^2\psi + \Gamma\psi, \qquad \text{and} \qquad \theta|_{z=z_B,z_T} = \partial_z\psi|_{z=z_B,z_T}. \tag{1.7}$$

To solve these equations in time, the QGPV and θ on the upper and lower boundaries are initialized, then the following steps are repeated:

- invert Equation (1.7) to get ψ from q, $\theta(z_T)$ and $\theta(z_B)$,
- calculate right hand side terms in Equation (1.5) (Jacobian, gradient advection, forcing and dissipation) from ψ,
- step q, $\theta(z_T)$ and $\theta(z_B)$ forward in time,

and because we assume simple horizontally periodic geometry the inversion can be done efficiently and accurately in the Fourier domain. Computing derivatives in the Fourier domain are trivial but computing the quadratic right hand side terms requires Fourier inversions and de-aliasing filters (Orszag, 1971). We also include a small scale filter in numerical simulations because Ekman friction is not scale selective (see Section A.1 of the Appendix for details of the small scale filter).

[4]The top and bottom of the fluid are defined here as $z = z_T$ and $z = z_B$ in the general context. In Chapter 3 the top and bottom are $z = H$ and $z = 0$ respectively for the atmosphere. In Chapters 4 and 5 the top and bottom are $z = 0$ and $z = -H$ in the ocean.

1.2.1 Quasi-geostrophic turbulence

Charney (1971) noted that when the boundary conditions (1.5b) and (1.5c) are neglected, the QG Equation (1.2) and the QGPV (1.3) are a three dimensional isomorphism of two dimensional (2D) turbulence. QGPV has the same functional form as vorticity $\zeta = \nabla^2\psi$ but with the addition of a vertical second derivative, and it is also horizontally advected, so all of the scaling laws that Kraichnan (1967) developed for 2D turbulence apply equally well in QG (away from boundaries). Specifically, QG conserves energy

$$\frac{dE}{dt} = \frac{d}{dt}\int \mathcal{E}(K)dK = -\int \psi\partial_t q dV = 0,$$

and enstrophy

$$\frac{dZ}{dt} = \frac{d}{dt}\int \mathcal{Z}(K)dK = \int q\partial_t q dV = 0,$$

where $K = |\mathbf{K}|$ is isotropic horizontal wavenumber[5], $\mathcal{E}(K)$ is the spectral energy density and $\mathcal{Z}(K)$ is the spectral enstrophy density[6]. Given a forcing scale K_f near the deformation scale L_d^{-1}, dimensional arguments ($\hat{q} \propto K^2\hat{\psi}$) imply that the net energy transfer must be towards large scales (small K) when spectral transfers occur. The shape of the spectrum in the inverse cascade is

$$\mathcal{E}(K) = \mathcal{C}\epsilon^{2/3}K^{-5/3}$$

[5]We will work in the Fourier and real space domains interchangeably, with the Fourier transform being applied in the horizontal directions. The streamfunction ψ is related to Fourier transform by $\psi(x,y,z,t) = \sum_{\mathbf{K}} e^{i\mathbf{K}\cdot\mathbf{x}}\hat{\psi}(\mathbf{K},z,t)$, where $\mathbf{K} = (k,\ell)$ the horizontal wavenumber vector.

[6]The specification of proper horizontal boundary conditions (such as periodic, no flow, or finite energy in an infinite domain) is required for conservation of energy and enstrophy to hold. We assume a doubly periodic domain in all of our calculations.

in the inertial range, where $\mathcal{C}$ is an $\mathcal{O}(1)$ Kolmogorov constant and ϵ [$\mathrm{m^2 s^{-3}}$] is the cascade rate. Similarly, because dimensional arguments imply

$$\mathcal{E}(K) = \mathcal{C}'\eta^{2/3}K^{-3},$$

in the inertial range of the forward enstrophy cascade[7], where η [$\mathrm{s^{-3}}$] is the cascade rate. Charney's (1971) geostrophic theory of turbulence also predicts a partition between the kinetic energy spectrum

$$\mathcal{KE}(K) = \frac{1}{2}K^2\hat{\psi}^2$$

and available potential energy spectrum

$$\mathcal{A}(K) = \frac{1}{2}\frac{f^2}{N^2}\hat{\theta}^2$$

which is proportional to the Burger number $KE/APE \sim L_d^2/\mathcal{L}^2$ when $z \sim H$, such as in the inverse cascade. In the forward cascade Charney's (1971) theory predicts equipartition between the KE and APE when $z \sim (f/N)\mathcal{L}$.

Charney (1971) realized that assuming the dynamics are "sufficiently far from walls" is a limitation near the tropopause and the ground. He postulated that frontal discontinuities at walls could produce a K^{-2} spectral slope, which could eventually give way to a $K^{-5/3}$ 3D turbulent energy cascade. He further argued that both of these regimes could be superimposed on the K^{-3} slope, tentatively giving a total spectrum of the form $AK^{-3} + BK^{-2} + CK^{-5/3}$, where A, B, and C

[7]For reference, Kraichnan (1971) computed $\mathcal{C} = 6.69$ and $C' = 2.626$. In a three dimensional forward energy cascade he computed $C = 1.40$. Kraichnan also added logarithmic corrections to the spectrum in the enstrophy cascade, but we neglect them here since they are minor and they vanish at small scales.

are constant coefficients (Charney, 1973).

1.2.2 Surface quasi-geostrophic dynamics

Complementary to Charney's geostrophic turbulence theory, Blumen (1978) proposed a turbulence model which neglected QGPV anomalies in the interior but included temperature anomalies on the upper and lower boundaries. Charney's model advects only equation (1.5a), while Blumen's model advects only equations (1.5b) and (1.5c). Blumen's model is often called "surface quasi-geostrophic" (SQG) because the dynamics are solely controlled by the surface conditions. The invariants in SQG are the volume integrated energy

$$\frac{dE_S}{dt} = \frac{d}{dt}\int \mathcal{E}_S(K)dK = \int \frac{f^2}{N^2}\psi\partial_t\theta dA = 0,$$

(note that the surface integral of $\psi\partial_t\theta$ replaced the volume integral of $-\psi\partial_t q$ by integration by parts) and the surface APE

$$\frac{dT}{dt} = \frac{d}{dt}\int \mathcal{T}(K)dK = \int \frac{f^2}{N^2}\theta\partial_t\theta dA = 0.$$

When there are spectral energy transfers the volume integrated energy must have a net upscale transfer, while the surface APE must have a net downscale transfer. Given a forward inertial range with cascade rate ϵ_T [$\mathrm{m^2 s^{-3}}$], dimensional arguments imply a forward energy spectrum

$$\mathcal{T}(K) = \mathcal{C}'_T\epsilon_T^{2/3}K^{-5/3}.$$

On the other hand an inverse cascade rate γ_T [$\mathrm{m}^3\mathrm{s}^{-3}$] gives an inverse energy spectrum

$$\mathcal{T}(K) = \mathcal{C}_T \gamma_T^{2/3} K^{-1},$$

where $\mathcal{T}(K)$ is the surface APE

$$\mathcal{T}(K) = \frac{1}{2}\frac{f^2}{N^2}\hat{\theta}^2\bigg|_{z=0}.$$

The forward energy cascade in SQG is quite different from the quasi-2D inverse energy cascade in QG turbulence. It has been the subject of rigorous math analysis (see *e.g.,* Constantin et al., 1994) since it is a physically motivated test problem for the regularity of the Navier-Stokes equations. See Held et al. (1995) for a review of SQG dynamics on the surface of a semi-infinite fluid.

Together Charney's QG and Blumen's SQG flows form a complete balanced turbulence. The Blumen dynamics are often not seen in numerical simulations either because of insufficient vertical resolution in a layered model, or because the boundary conditions are neglected in modal models which decompose the vertical structure into "neutral" modes. This vertical resolution issue of will be discussed further in Chapter 2.

1.3 Overview of the chapters

The goal of Chapter 2 is to introduce our surface-modal model (SMQG) formulation and compare it with traditional layered and modal models. The equivalence between Bretherton's (1966) handling of boundary conditions via QGPV-sheets and our streamfunction decomposition formulation is shown explicitly. Then con-

vergence is shown for both Eady-Green type linear instability and the nonlinear evolution of the Eady problem. Finally, two simplified models are described in order to illustrate the SQG energy spectrum and the interaction between surface energy and interior energy.

In Chapter 3 the SMQG formulation is truncated and applied as a model for the atmospheric energy spectrum. After discussing the atmospheric observations and previous explanations the simple two mode-two surface (TMTS) model with uniform stratification is shown to reproduce the actual spectrum surprisingly well. The TMTS spectrum reproduces the observed transition from a steep -3 slope to a shallow -5/3 slope at the surface, and the horizontal scale of transition is predicted via a theory that depends on the relative magnitudes of the surface and interior QGPV and temperature gradients.

In Chapter 4 the SMQG formulation is applied to the non-uniformly stratified oceanic problem in an attempt to interpret SSH observations in terms of QG and SQG turbulence. There is a debate in the scientific community as to what mode of variability the SSH signal represents. Typically, because of the ocean's stratification, it is assumed that the mesoscale surface signal most represents dynamics in the first baroclinic mode (Wunsch, 1997; Stammer, 1997). However recent studies that diagnosed a general circulation model (GCM) of the North Atlantic concluded that SQG dominates the first baroclinic mode in some locations (Lapeyre and Klein, 2006; Lapeyre, 2008). First, the scaling theory for the transition between interior and surface dominated dynamics from Chapter 3 is generalized to nonuniform stratification, and verified via simulations with exponential stratification in the SMQG model. Then the scaling theory is applied to a new global ocean atlas from Forget (2008) to determine which locations are likely dominated

by SQG dynamics at the surface. An example simulation for a location in the ACC is also presented as a verification of the scaling. Global baroclinic instability maps are also computed for comparison with the transition scale map.

Continuing on the theme of sea surface dynamics, Chapter 5 interprets satellite altimetric observations in terms of Rossby waves and geostrophic turbulence. By applying linear QG theory to observations of coherent westward phase propagation we determine whether the propagation is due to linear Rossby waves or nonlinear turbulence. Numerous studies indicate that observations are consistent with linear waves (see *e.g.,* Chelton and Schlax, 1996; Killworth and Blundell, 2005), while other studies argue that observations are consistent with turbulence (Chelton et al., 2007). By comparing observed phase speeds with predicted phase speeds, as well as surface drifter speeds, we argue that altimeters see wave propagation in the tropics and turbulence in the midlatitudes.

Chapter 2

Model formulation and simplifications

In this chapter the surface-modal QG (SMQG) is formulated and compared with a typical layered formulation. Then two simplified models are analyzed with a view towards understanding how surface QG dynamics can alter the energy spectra near the surface.

2.1 Layered formulation

QG is often solved using a layered formulation, which considers the fluid as a set of immiscible, uniform density layers. Pedlosky (1987) shows that a layered formulation is equivalent to a "level" model, which is a finite-difference approximation to the QGPV Equation (1.5a) for a continuously stratified fluid. Figure 2.1 illustrates the discretization at layer n of such a model. The discretized streamfunction ψ_n is defined at height z_n, the mid-depth of layer n, which has thickness δ_n. With this

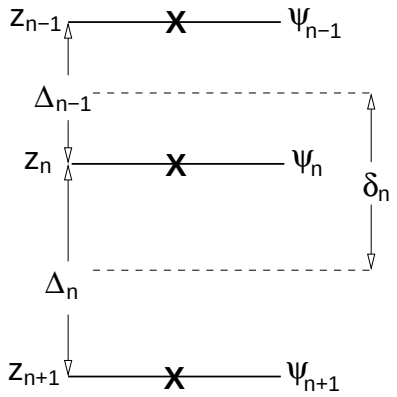

Figure 2.1: The grid used to represent vertical structure. Δ_n is the spacing between ψ_n and ψ_{n+1}, while δ_n is the distance between half spaces: $\delta_n = (\Delta_{n-1} + \Delta_n)/2$.

discretization the QGPV in layer n is given by

$$q_n = \nabla^2\psi_n + \frac{f^2\rho_0}{g}\begin{cases} \frac{1}{\delta_1}\left(\frac{\psi_2-\psi_1}{\bar{\rho}_2-\bar{\rho}_1}\right), & n=1 \\ \frac{1}{\delta_n}\left(\frac{\psi_{n-1}-\psi_n}{\bar{\rho}_n-\bar{\rho}_{n-1}} - \frac{\psi_n-\psi_{n+1}}{\bar{\rho}_{n+1}-\bar{\rho}_n}\right), & n=2\,..\,\mathcal{N}-1 \\ \frac{1}{\delta_{\mathcal{N}}}\left(\frac{\psi_{\mathcal{N}-1}-\psi_{\mathcal{N}}}{\bar{\rho}_{\mathcal{N}}-\bar{\rho}_{\mathcal{N}-1}}\right), & n=\mathcal{N} \end{cases} \tag{2.1}$$

where $\bar{\rho}_n$ is the background density profile at z_n, ρ_0 is the average density and $\mathcal{N}$ is the total number of layers[1]. Similarly, the thermodynamic variable at height z_n is given by

$$\theta_n = \frac{\psi_{n-1} - \psi_{n+1}}{\Delta_{n-1} + \Delta_n},$$

where Δ_n is the spacing between z_n and z_{n+1}. Streamfunction inversions using this discretization will have errors of order $\mathcal{O}(\delta z^2)$ in the interior and $\mathcal{O}(\delta z)$ near the boundary. When SQG dynamics prevail near the boundary vertical derivatives scale with to horizontal gradients as $\partial_z = (N/f)|\nabla|$ at length scales smaller than the deformation radius (since $\theta \sim K\psi$ in SQG), so a vertical scale δz is equivalent

[1]The number of layers $\mathcal{N}$ should not be confused with the buoyancy frequency $N^2 = -\frac{g}{\rho_0}\frac{d\bar{\rho}}{dz}$

to a horizontal length scale of $N\delta z/f$. Therefore the vertical finite differencing operator effectively includes an approximation that is accurate to $\mathcal{O}(N\delta z/f)$ so temperature dynamics at smaller horizontal scales ($K > (N/f)\delta z$) are not captured. This vertical resolution issue will be discussed more in Section 2.3, where we conclude that such a finite difference approach is valid near the deformation scale but requires high vertical resolution to properly represent horizontal scales smaller than the deformation scale.

2.2 Surface-modal formulation

The same accuracy advantages gained by representing horizontal motions spectrally can be gained by projecting the vertical structure onto appropriate stratification modes. When the surface dynamics are ignored (by explicitly or implicitly assuming $\psi_z = 0$ at the top and bottom): the problem is separable in the vertical, and the solutions to the vertical structure problem (the neutral modes) form a normal basis onto which the motion can be projected (Flierl, 1978; Hua and Haidvogel, 1986). The goal here is to construct a general framework (for arbitrary stratification) to include the surface dynamics and still retain spectral accuracy in the vertical. We want to ensure that the method preserves horizontal signals due to the surface dynamics down to the horizontally resolved scales, without the necessity of very high vertical resolution.

2.2.1 Streamfunction decomposition

The linearity of the relation between streamfunction and potential vorticity in QG allows for the decomposition of Equation (1.5) using a set of streamfunctions that

separately solve problems with $\theta(z_T) = \theta(z_B) = 0$ for the interior flow, and $q = 0$ for the surface flow. We let

$$\psi = \psi^I + \psi^T + \psi^B \tag{2.2}$$

where these functions solve

$$\nabla^2\psi^I + \Gamma\psi^I = q, \qquad \psi^I_z\,|_{z=z_T} = 0, \qquad \psi^I_z|_{z=z_B} = 0 \tag{2.3a}$$

$$\nabla^2\psi^T + \Gamma\psi^T = 0, \qquad \psi^T_z|_{z=z_T} = \theta^T, \qquad \psi^T_z|_{z=z_B} = 0 \tag{2.3b}$$

$$\nabla^2\psi^B + \Gamma\psi^B = 0, \qquad \psi^B_z|_{z=z_T} = 0, \qquad \psi^B_z|_{z=z_B} = \theta^B. \tag{2.3c}$$

Where q, θ^T and θ^B appear in Equation (1.5), they can be replaced using the above expressions, but where ψ appears explicitly (in the tendency and advection terms), all three components must be summed. Various models addressed in the literature are obtained from this set in certain limits. For example, typical modal representations amount to setting $\theta^T = \theta^B = 0$, surface quasi-geostrophy (SQG—see Held et al., 1995) sets $q = \theta^B = 0$ and $z_B \to \infty$, and Blumen's (1978) two surface-layer model sets $q = 0$. Similar decompositions have been used in the past; for example Davies and Bishop (1994) applied such a decomposition to Edge waves with interior PV distributions, and Lapeyre and Klein (2006) used it as framework through which to interpret oceanic surface signals.

Equivalence between streamfunction decomposition and PV-sheets

Our streamfunction decomposition is equivalent to the PV-sheet method of Bretherton (1966), Heifetz et al. (2004) and others, which replaces the inhomogeneous

boundary conditions in (1.7) with homogeneous ones by augmenting the potential vorticity with delta-sheets at each surface. This equivalence can be shown using the following Green's function method. Working in the spectral domain, and defining a linear operator $\underline{L} \equiv [\partial_z s \partial_z - K^2]$, where $s = f^2/N^2$ (and suppressing the dependence on time), allows Equation (1.7) to be expressed as

$$\underline{L}\hat{\psi} = \hat{q}, \quad \hat{\psi}_z(z_T) = \hat{\theta}^T, \quad \hat{\psi}_z(z_B) = \hat{\theta}^B.$$

Its associated Green's function $g(z, \xi)$ therefore satisfies

$$\underline{L}g(z, \xi) = \delta(z - \xi), \quad g_z(z_B, \xi) = g_z(z_T, \xi) = 0.$$

The streamfunction, which is obtained by integrating by parts $\int_{z_B}^{z_T} g(z, \xi)\underline{L}\hat{\psi}(\xi)d\xi$, is given by[2]

$$\hat{\psi}(z) = \int_{z_B}^{z_T} g(z, \xi)\hat{q}(\xi)\ d\xi + sg(z, z_B)\hat{\theta}^B - sg(z, z_T)\hat{\theta}^T. \tag{2.4}$$

Bretherton (1966) defined a modified PV

$$\tilde{q} = \hat{q} + s\delta(z - z_B)\hat{\theta}^B - s\delta(z - z_T)\hat{\theta}^T,$$

[2]For uniform stratification on $z \in [0, H]$, the homogeneous problem for $\hat{\psi}$ can be solved separately on the domains $0 \le z \le \xi$ and $\xi \le z \le H$ (and using that g is continuous and satisfies a jump condition), one finds

$$g(\mu, z, \xi) = \begin{cases} -\frac{N^2 H}{f^2 \mu} \cosh\left(\mu \frac{\xi - H}{H}\right) \cosh\left(\mu \frac{z}{H}\right) \operatorname{csch} \mu, & z \in (0, \xi) \\ -\frac{N^2 H}{f^2 \mu} \cosh\left(\mu \frac{z - H}{H}\right) \cosh\left(\mu \frac{\xi}{H}\right) \operatorname{csch} \mu, & z \in (\xi, H), \end{cases}$$

is the Green's function for the dynamic streamfunction $\hat{\psi}$, where $\mu = KNH/f$.

so that, with the modified PV, the streamfunction $\hat{\psi}$ solves

$$\underline{L}\hat{\psi} = \tilde{q}, \quad \hat{\psi}_z(z_T) = \hat{\psi}_z(z_B) = 0, \tag{2.5}$$

where $\tilde{q}$ is sometimes referred to as the *standardizing function* (see Butkovskii, 1982) for the boundary value problem (1.7). But the solution to (2.5) is equivalent to (2.4), since

$$\int_{z_B}^{z_T} g(z,\xi)\tilde{q}\; d\xi = \int_{z_B}^{z_T} g(z,\xi)\hat{q}(\xi)\; d\xi + sg(z,z_B)\hat{\theta}^B - sg(z,z_T)\hat{\theta}^T.$$

The integral in Equation (2.4) is $\hat{\psi}^I$ in our streamfunction decomposition formulation in Equation (2.4). Similarly, the boundary terms in (2.4) are $\hat{\psi}^B$ and $\hat{\psi}^T$ in (2.4). The advantage of using the streamfunction decomposition (2.2) is that, among all three methods, this one allows the most straightforward, unambiguous numerical implementation, and avoids the need for high-resolution finite-difference methods to capture surface effects.

2.2.2 Modal representation

We represent horizontal motions spectrally and project the vertical structure onto appropriate stratification modes,

$$\psi = \sum_{\boldsymbol{K}} \mathrm{e}^{i\boldsymbol{K}\cdot\boldsymbol{x}} \left[\hat{\psi}^T(\boldsymbol{K},t)\phi^T(K,z) + \sum_m \hat{\psi}_m(\boldsymbol{K},t)\phi_m(z) + \hat{\psi}^B(\boldsymbol{K},t)\phi^B(K,z) \right], \tag{2.6}$$

where $\hat{\psi}^T(\boldsymbol{K},t)$, $\hat{\psi}^B(\boldsymbol{K},t)$ and $\hat{\psi}_m(\boldsymbol{K},t)$ Fourier transformed variables with the vertical dependence separated out and $\phi^T(K,z)$, $\phi^B(K,z)$ and $\phi_m(z)$ are the verti-

cal modes, which are defined below[3]. The decomposition in Equation (2.3) allows for the vertical modes be computed separately and independent of time.

Interior modes

The interior modes are identical to those used in a standard modal representation of QG, as in Flierl (1978)and Hua and Haidvogel (1986). Specifically, $\phi_m(z)$ solve

$$\Gamma\phi_m = -\lambda_m^2\phi_m, \quad \partial_z\phi_m|_{z=z_T} = 0, \quad \partial_z\phi_m|_{z=z_B} = 0, \tag{2.7}$$

where the λ_m are the eigenvalues and ϕ_m are the (orthonormal) eigenfunctions.

Surface modes

The surface modes are not independent of horizontal position, but in the horizontal Fourier projection, they are separable. We can separate the dependence on $\hat{\theta}^{T,B}$ and time in the spectral form of the surface problems (2.3b) and (2.3c) by assuming $\hat{\psi}^{T,B}(\boldsymbol{K}, z, t) = \hat{\theta}^{T,B}(\boldsymbol{K}, t)\bar{\phi}^{T,B}(K, z)$, where $\bar{\phi}^{T,B}(K, z)$ are solutions to

$$\left(-K^2 + \Gamma\right)\bar{\phi}^T = 0, \quad \left.\frac{d\bar{\phi}^T}{dz}\right|_{z=z_T} = 1, \quad \left.\frac{d\bar{\phi}^T}{dz}\right|_{z=z_B} = 0 \tag{2.8}$$

and

$$\left(-K^2 + \Gamma\right)\bar{\phi}^B = 0, \quad \left.\frac{d\bar{\phi}^B}{dz}\right|_{z=z_T} = 0, \quad \left.\frac{d\bar{\phi}^B}{dz}\right|_{z=z_B} = 1, \tag{2.9}$$

[3]Note that we will use the same notation for height separated variables as for variables with height dependence but the z dependence will be suppressed, *e.g.,* $\hat{\psi}^T(\boldsymbol{K}, z, t)$ is the top surface streamfunction with height dependence and $\hat{\psi}^T(\boldsymbol{K}, t)$ is the top surface streamfunction without height dependence.

respectively. The un-barred functions $\phi^{T,B}$ (the modes) in (2.6) are then

$$\phi^T = \frac{\bar{\phi}^T(K,z)}{\bar{\phi}^T(K,z_T)} \quad \text{and} \quad \phi^B = \frac{\bar{\phi}^B(K,z)}{\bar{\phi}^B(K,z_B)}.$$

The surface streamfunction components in Equation (2.6) are evaluated at the positions of the upper and lower boundaries, $\hat{\psi}^T(\boldsymbol{K},t) = \hat{\psi}^T(\boldsymbol{K},z_T,t)$ and $\hat{\psi}^B(\boldsymbol{K},t) = \hat{\psi}^B(\boldsymbol{K},z_B,t)$, as are $\hat{\theta}^T$ and $\hat{\theta}^B$, and so the inversion between them is most easily expressed in terms of the $\bar{\phi}$ functions

$$\hat{\psi}^T(\boldsymbol{K},t) = \bar{\phi}^T(K,z_T)\hat{\theta}^T(\boldsymbol{K},t), \qquad \hat{\psi}^B(\boldsymbol{K},t) = \bar{\phi}^B(K,z_B)\hat{\theta}^B(\boldsymbol{K},t).$$

The vertical structure of the problem is now expressed in terms of the functions $\phi^T(K,z)$, $\phi_m(z)$ and $\phi^B(K,z)$, with Fourier coefficients $\hat{\psi}^T$, $\hat{\psi}_m$, and $\hat{\psi}^B$, and the full streamfunction is reconstructed as in (2.6). As an example, in the Eady problem discussed in Section 2.3.2, the correspondence to the general functions derived here is

$$\bar{\phi}^T = \frac{H\cosh\left[\mu(z-z_B)/H\right]}{\mu\sinh\mu} \quad \text{and} \quad \bar{\phi}^B = \frac{H\cosh\left[\mu(z-z_T)/H\right]}{\mu\sinh\mu},$$

where $H = z_T - z_B$ and $\mu = KNH/f$ is the magnitude of the horizontal wavenumber scaled by the deformation length.

The projected mean velocity

The mean velocity $\boldsymbol{U}(z)$ must also be projected onto interior and surface components $\boldsymbol{U}(z) = \boldsymbol{U}^T(z) + \boldsymbol{U}^I(z) + \boldsymbol{U}^B(z)$. To simplify the notation we combine the top and bottom mean velocities into a single surface velocity $\boldsymbol{U}^S(z) = \boldsymbol{U}^T(z) + \boldsymbol{U}^B(z)$.

Since the shear of the surface component must be constant $\Gamma \boldsymbol{U}^S = \text{constant}$, it solves the following elliptic problem

$$\Gamma \boldsymbol{U}^S = \frac{f^2}{H}\left[\frac{\nabla^\perp \Theta(z)}{N^2(z)}\right]\Big|_{z_B}^{z_T}, \quad \frac{d\boldsymbol{U}^S}{dz}(z_T) = \nabla^\perp \Theta^T, \quad \frac{d\boldsymbol{U}^S}{dz}(z_B) = \nabla^\perp \Theta^B,$$

where $\nabla^\perp = (-\partial_y, \partial_x)$. Therefore the mean surface velocity is

$$\boldsymbol{U}^S(z) = \frac{1}{H}\int^z N^2(z')\left[(z'-z_B)\frac{\nabla^\perp \Theta^T}{N^2(z_T)} - (z'-z_T)\frac{\nabla^\perp \Theta^B}{N^2(z_B)}\right] dz'.$$

The interior component of the mean velocity contains no surface gradients so it projects onto the interior modes, so the total mean velocity is

$$\boldsymbol{U}(z) = \boldsymbol{U}^S(z) + \sum_m \phi_m(z)\boldsymbol{U}_m. \tag{2.10}$$

The projected QG equations

The SMQG advection equations are obtained by multiplying (1.5a) by ϕ_n/H and integrating vertically (*i.e.,* projecting onto mode n) to get

$$\begin{aligned}\partial_t \hat{q}_n + \sum_m \Big[\hat{J}(\langle\hat{\psi}\rangle_{mn}, \hat{q}_m) + i\boldsymbol{K}\cdot\Big(\langle\hat{\psi}\rangle_{mn}\lambda_m^2 \boldsymbol{U}_m + \langle\boldsymbol{U}\rangle_{mn}\hat{q}_m\Big)\Big] \\ + i\left(k\beta - \boldsymbol{K}\cdot\Gamma\boldsymbol{U}^S\right)\langle\hat{\psi}\rangle_n = 0,\end{aligned} \tag{2.11}$$

where $\Gamma\boldsymbol{U}^S = \text{constant}$, $\hat{J}$ is shorthand notation for the double summation over horizontal wavenumbers involving the Jacobian terms and the projection operators

are defined as

$$\langle\cdot\rangle_n = \frac{1}{H}\int_{z_B}^{z_T} \cdot\ \phi_n\ dz, \quad \langle\cdot\rangle_{mn} = \frac{1}{H}\int_{z_B}^{z_T} \cdot\ \phi_n\phi_m\ dz.$$

For example

$$\langle\hat{\psi}\rangle_{mn} = \langle\phi^T\rangle_{mn}\hat{\psi}^T + \langle\phi^B\rangle_{mn}\hat{\psi}^B + \sum_\ell \langle\phi_\ell\rangle_{mn}\hat{\psi}_\ell,$$

$$\langle\boldsymbol{U}\rangle_{mn} = \langle\boldsymbol{U}^S\rangle_{mn} + \sum_\ell \langle\phi_\ell\rangle_{mn}\hat{U}_\ell.$$

The advection equations at each of the surfaces are obtained by evaluating (1.5b) at $z = z_T$ and (1.5c) at $z = z_B$

$$\partial_t\hat{\theta}^T + \hat{J}(\hat{\psi}|_{z=z_T}, \hat{\theta}^T + \Theta^T) + i\boldsymbol{U}(z_T)\cdot\boldsymbol{K}\hat{\theta}^T = 0, \tag{2.12a}$$

$$\partial_t\hat{\theta}^B + \hat{J}(\hat{\psi}|_{z=z_B}, \hat{\theta}^B + \Theta^B) + i\boldsymbol{U}(z_B)\cdot\boldsymbol{K}\hat{\theta}^B = rK^2\hat{\psi}|_{z=z_B}, \tag{2.12b}$$

Note that evaluations of the streamfunction and mean zonal velocities in (2.12) are the full streamfunction as written in (2.6).

Model algorithm

The full equations of motion can be evolved in time by first solving Equations (2.7), (2.8) and (2.9) for the vertical structure, initializing $\hat{q}$, $\hat{\theta}^T$ and $\hat{\theta}^B$, and then repeating the following four steps:

- invert $\hat{q}$ to get $\hat{\psi}^I$, $\hat{\theta}^T$ to get $\hat{\psi}^T$, and $\hat{\theta}^B$ to get $\hat{\psi}^B$,
- construct $\hat{\psi}$ using Equation (2.2)
- calculate right hand side terms (*i.e.,* the Jacobians, forcing and dissipation),

- step $\hat{q}$, $\hat{\theta}^T$, and $\hat{\theta}^B$ in time.

2.3 Convergence of layered QG and the surface-modal formulation

A standard finite difference QG model with only two vertical levels is isomorphic to the Phillips model (Pedlosky, 1987). Yet when the vertical resolution is increased, keeping stratification and shear constant, the finite difference model should approach a representation of the Eady model. Here we explicitly show that this is the case, up to a horizontal wavenumber that depends on the vertical resolution of the model. Since temperature θ in the QG approximation is the vertical derivative of the streamfunction $\delta\psi/\delta z$, where δz is the vertical grid spacing, and vertical and horizontal scales are linked by the Prandtl ratio N/f, horizontal scales are only accurately represented at wavenumbers sufficiently smaller than $k_{\delta z} = f/(N\ \delta z)$. Surface effects, dominated by temperature advection, are therefore absent from low vertical resolution QG simulations, and in general, only partially represented down to scales of order $\ell_z = N\delta z/f$. An analogous argument was made by Solomon and Lindzen (2000), who demonstrated the necessity of sufficient resolution to model the barotropic instability of a point jet (see also Lindzen and Fox-Rabinovitz, 1989; Fox-Rabinovitz and Lindzen, 1993).

2.3.1 Linear instability convergence

First we consider Eady-Green type instabilities (Green, 1960) which have the following configuration: β-plane, uniform stratification and (zonal) shear, and the fluid is bounded by rigid surfaces separated by a depth H. The mean interior

QGPV gradient is $\partial_y Q = \beta$ and the mean temperature gradient is independent of depth $\partial_y \Theta(z_T) = \partial_y \Theta(z_B)$. Therefore the linearization of Equation (1.5) reduces to

$$\begin{aligned} \partial_t q + U\partial_x q + v\beta = 0, \qquad & z_B < z < z_T, \\ \partial_t \theta + U\partial_x \theta + v\partial_y \Theta = 0, \qquad & z = z_B, z_T, \end{aligned}$$

which upon substituting a wave solution of the form $\mathrm{e}^{-i(kx-\omega t)}$ becomes

$$\omega \hat{q} = k[U(z)\hat{q} + \beta\hat{\psi}], \qquad z_B < z < z_T, \tag{2.14a}$$

$$\omega \hat{\theta} = k[U(z)\hat{\theta} + \partial_y \Theta \hat{\psi}], \qquad z = z_B, z_T, \tag{2.14b}$$

where $U(z) = [z - (z_T + z_B)/2] \cdot \partial_y \Theta$. In the layered formulation the vortex stretching operator is discretized as in Equation (2.1) which creates an $\mathcal{N} + 2$ linear eigenvalue problem, with the growth rate given by $\omega_i = \max[\mathfrak{Im}(\omega)]$ at each value of the zonal wavenumber k and PV gradient β ($\partial_y \Theta = 1$ is held constant, and $f\mathcal{L}/NH = 1$). See Appendix A.2 for the equivalent linearization using the surface-modal formulation. Figure 2.2 shows the growth rates (ω_i) for the layered formulation on the (k, β)-plane as the number of layers in the discretization is increased, $\mathcal{N} = 2, 10, 30, 50$. With just 2 layers, only the Phillips instability is present at deformation scales, and large values of β inhibit it. As the number of layers is increased, the deformation scale Eady instability at $\beta = 0$ becomes better resolved and weak "Green" (long-wave) instabilities fill out the small k, large β regions. Strong Charney instabilities develop at small scales near $z = z_B$ and $z = z_T$. As $\mathcal{N}$ increases the peak Charney growth rate converges to the line

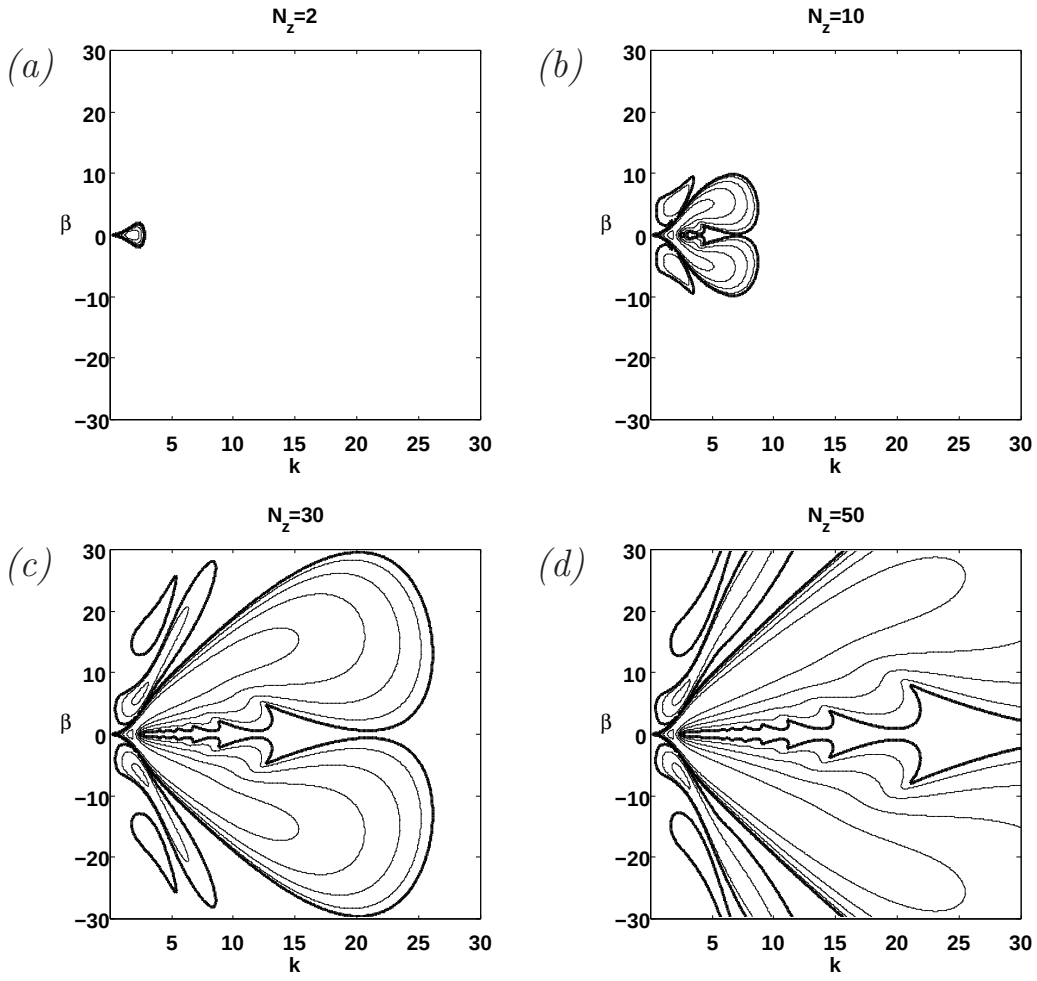

Figure 2.2: Contours of growth rate ω_i in a typical layered formulation for the Eady-Green type instability. Growth rate is plotted against nondimensional zonal wavenumber k and nondimensional planetary vorticity gradient β for $\mathcal{N} = 2, 10, 30$ and 50 layers. The thick contour is $\omega_i = 0.05$, and the contour intervals are 0.05.

$k = \pm 0.83\beta$ for $k \gg 1$ (Green, 1960).

Figure 2.3 shows the growth rates for a linearization of a typical modal formulation (Flierl, 1978), for $\mathcal{N} = 2, 10, 30, 50$ interior modes, neglecting the surface modes in Equation (A.9c). Although the modal solution without surface modes converges to the layered instability, it does so slowly. For any given number of layers and modes $\mathcal{N}$ the instabilities differ at the largest resolved k and β values. Also note that short wave cutoff of the Eady instability (where $\beta = 0$) emerges very slowly as the number of modes is increased because numerical instabilities arise between the vertical modes.

The Eady-Green instability for the SMQG formulation (with both interior and both surface modes) is plotted in Figure 2.4 with $\mathcal{N} = 2, 10, 30, 50$ interior modes. Including surface modes gives explicit Green and Charney modes for nonzero β regardless of the number of interior modes, which means dynamics near the surfaces can be explicitly resolved with only a few vertical modes. A more detailed analysis of surface-modal instabilities with $\mathcal{N} = 2$ is given in Chapter 3.

2.3.2 Nonlinear Eady turbulence

Next we show, using an Eady configuration, that the nonlinear dynamics in the layered formulation converge to the dynamics of a model controlled solely by surface dynamics. The Eady configuration takes $\beta = 0$, uniform stratification and shear, and the fluid is bounded by rigid surfaces separated by a depth H. The mean interior QGPV gradient is $\partial_y Q = 0$ and the mean surface temperature gradients are equal $\partial_y \Theta(z_T) = \partial_y \Theta(z_B)$, thus $q = 0$ and the motion is determined by temperature advection on the boundaries. The remaining equations from (2.12)

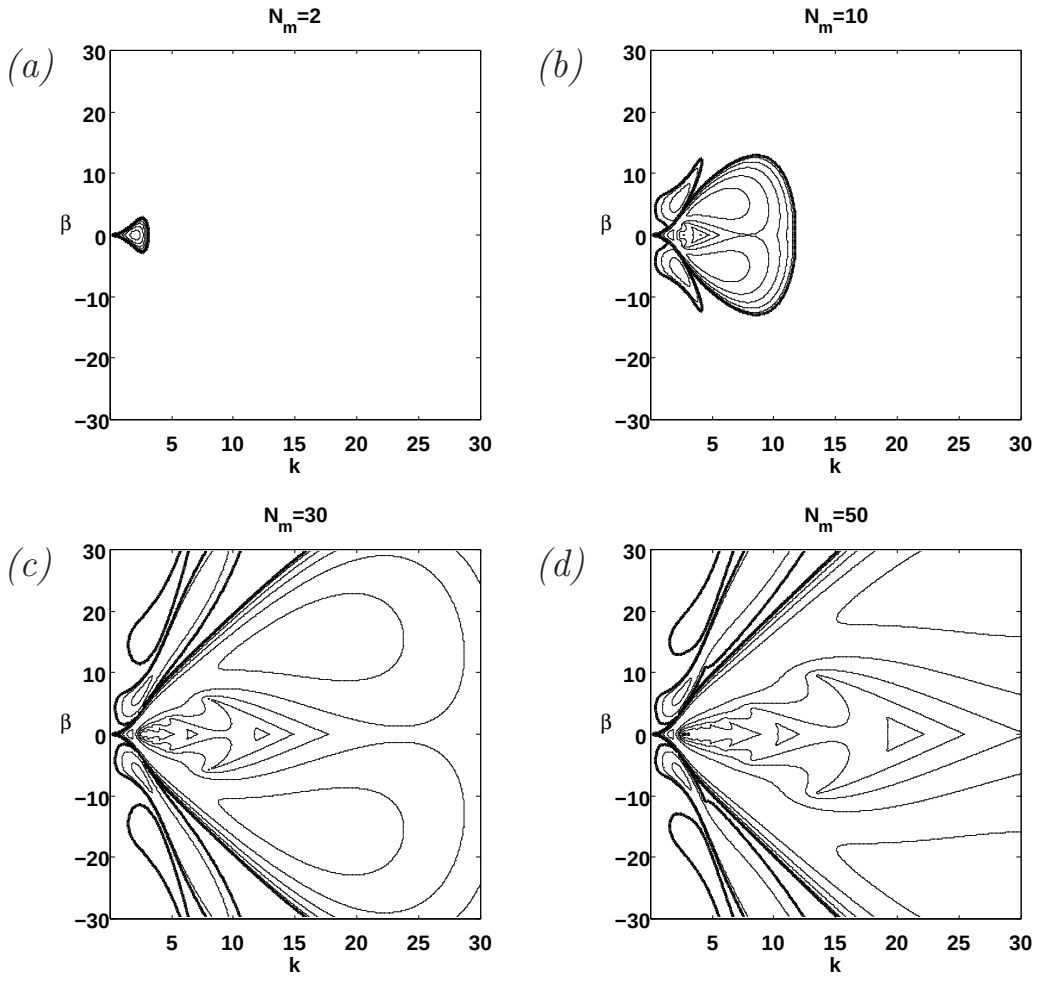

Figure 2.3: Contours of growth rate ω_i in a typical modal formulation for the Eady-Green type instability. Growth rate is plotted against nondimensional zonal wavenumber k and nondimensional planetary vorticity gradient β for $N_z = 2, 10, 30$ and 50 layers. The thick contour is $\omega_i = 0.05$, and the contour intervals are 0.05.

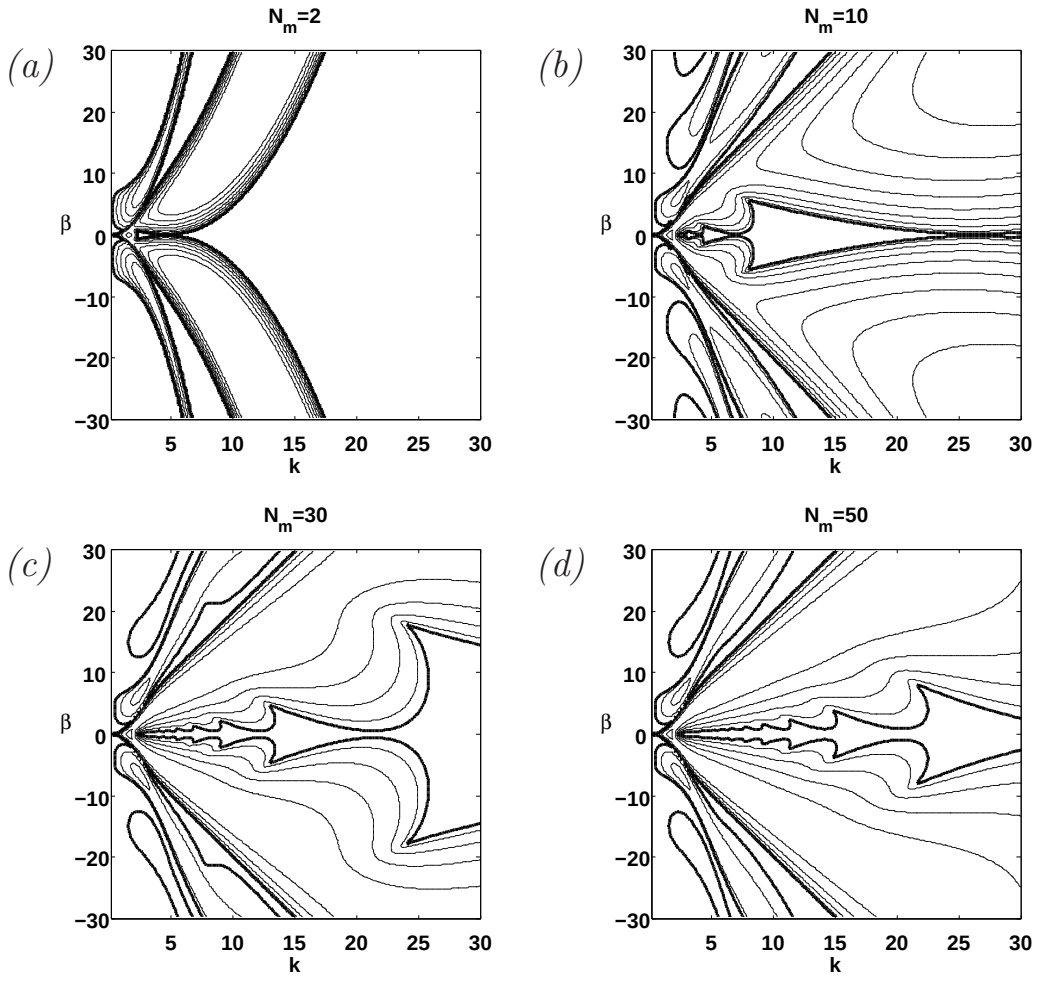

Figure 2.4: Contours of growth rate ω_i in the SMQG formulation for the Eady-Green type instability. Growth rate is plotted against nondimensional zonal wavenumber k and nondimensional planetary vorticity gradient β for $N_z = 2, 10, 30$ and 50 layers. The thick contour is $\omega_i = 0.05$, and the contour intervals are 0.05.

are (in Fourier space)

$$\partial_t \hat{\theta} + \hat{J}(\hat{\psi}, \hat{\theta}) + ik(U\hat{\theta} + \hat{\psi}\partial_y \Theta) = 0, \qquad \text{at} \qquad z = z_T, z_B$$

and the temperature-streamfunction inversion relation is given by

$$\hat{\psi}(\boldsymbol{K}, z, t) = \frac{H}{\mu \sinh \mu} \left[\cosh\left(\mu \frac{z - z_B}{H}\right) \hat{\theta}^T(\boldsymbol{K}, t) - \cosh\left(\mu \frac{z - z_T}{H}\right) \hat{\theta}^B(\boldsymbol{K}, t) \right],$$

where $\mu = KNH/f$. We refer to this model as the "Blumen model" (Blumen, 1978).

One can understand the turbulent dynamics of the Eady model by considering the advection equations at each surface in the limits of large and small scales separately. At the upper boundary the streamfunction is

$$\hat{\psi}(\boldsymbol{K}, z_T, t) = \frac{H}{\mu} \left[\frac{\hat{\theta}^T(\boldsymbol{K}, t)}{\tanh \mu} - \frac{\hat{\theta}^B(\boldsymbol{K}, t)}{\sinh \mu} \right],$$

so at large scales ($\mu \ll 1$), both $\sinh \mu$ and $\tanh \mu$ are approximately μ, which means that $\hat{\psi}(\boldsymbol{K}, z_T, t) \simeq (H/\mu^2) \left[\hat{\theta}^T(\boldsymbol{K}, t) - \hat{\theta}^B(\boldsymbol{K}, t) \right] \equiv (H/\mu^2) \Delta\hat{\theta}$. A similar relation arises at the bottom boundary, giving $\hat{\psi}(\boldsymbol{K}, z_B, t) \simeq \hat{\psi}(\boldsymbol{K}, z_T, t)$. Subtracting the upper and lower advection equations, one has

$$\partial_t \Delta\hat{\theta} + \hat{J}(\hat{\psi}, \Delta\hat{\theta}) + ikU\Delta\hat{\theta} \simeq 0$$

so the equation for the temperature difference between the two surfaces is isomorphic to 2D vorticity flow since $-\Delta\hat{\theta} = -\mu^2\hat{\psi}/H$, *i.e.,* $-(f/N)^2\Delta\hat{\theta}/H = -K^2\hat{\psi}$, in this limit. On the other hand, at small scales ($\mu \gg 1$), $\sinh \mu \to \infty$ and $\tanh \mu \sim 1$,

so that $\hat{\psi}(\boldsymbol{K}, z_T, t) \simeq (H/\mu)\hat{\theta}^T(\boldsymbol{K}, t)$ (similarly at the bottom), and each surface obeys SQG dynamics independently of the other surface.

In between these scale limits, where $\mu \sim 1$, baroclinic instability pumps energy into the eddying flow. Thus the small-scale limit is governed by the direct cascade, while the large-scale limit is controlled by the inverse cascade. Surface potential and kinetic energies in the inverse cascade of baroclinic turbulence and in the SQG direct cascade are all expected to obey a -5/3 slope, thus in non-linear Eady turbulence *there should be no spectral break in the surface kinetic energy spectra, and a -5/3 surface spectrum should dominate all scales.* But there should be a horizontal scale dependence on the interior flow. At large scales, temperature signals at each surface "see" the other surface, yielding a quasi-barotropic flow, so the interior spectrum should also approach a -5/3 slope. At small scales, the temperature signals are trapped near their respective surfaces, and so the interior spectrum should decay with depth and horizontal wavenumber.

We run a series of simulations, using two discretizations with the Eady mean state: (I) using the layered formulation with full vertical resolution and the finite difference operator given in equation (2.1), and (II) the "Blumen model", which advects only the upper and lower temperature fields. The calculations are performed in a spectral domain, with wavenumber 1 just filling the domain. The nonlinear terms are calculated using a de-aliased fast Fourier transform. Forward cascades are dissipated using the exponential cutoff filter described in Appendix A.1. The horizontal resolution of the simulations is $K_{\max} = 255$, or 512^2 in grid space. To preserve the dynamics and spectral slopes, the slow inverse cascades are not dissipated.

Figure 2.5 shows the results of the simulations using the layered QG formu-

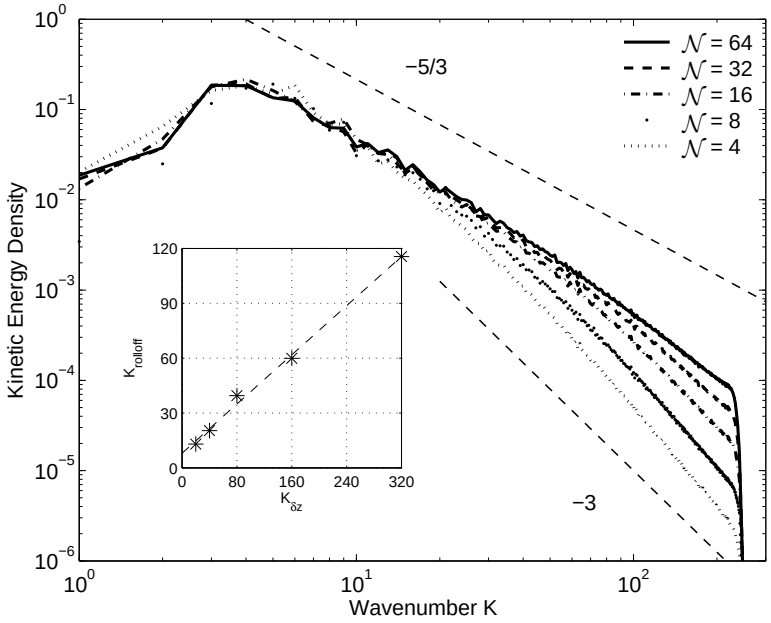

Figure 2.5: Kinetic energy density versus wavenumber magnitude K in the top layer of a series of Eady-forced QG simulations (with $\mathcal{N} = 4, 8, 16, 32, 64$ layers, $\beta = 0$, $U_z = 1$ and (nondimensional) deformation wavenumber $K_d = f\mathcal{L}/NH = 5$. Since there is no large-scale dissipation, the spectra shown are normalized by baroclinic generation rate and then averaged in time between $t = 4.5$ and $t = 5$ for each simulation. The inset shows measured roll-off wavenumbers (where the spectral slope is $K^{-7/3}$) versus the prediction $K_{\delta z} = f/(N\delta z)$. The best fit line $K_{-7/3} = 0.34K_{\delta z} + 8$.

lation. The kinetic energy density $K^2|\hat{\psi}|^2$ is plotted versus K at the top level z_1 for simulations with increasing vertical resolution: $\mathcal{N} = 4, 8, 16, 32$ and 64 levels. All of the simulations have the same nondimensional deformation scale $K_d = f\mathcal{L}/NH = 5$ and seed energy $E(t = 0) = 10^{-3}$) centered around wavenumber magnitude $K_0 = 10$. The energy grows due to Eady baroclinic instability, leading to a dual cascade. The peak linear growth rate is near $1.6K_d \approx 8$ and there is no baroclinic growth at wavenumbers above $2.4K_d \approx 12$. Since there is

no large scale drag to halt the cascade and equilibrate the motion, we show a partial time average ($t = 4.5$ to $t = 5$ in nondimensional time) of the KE density, normalized by $\epsilon^{2/3}$, where $\epsilon = Uf^2/HN^2(\overline{v\theta}|_{z=z_T} - \overline{v\theta}_{z=z_B})$ is the baroclinic energy generation rate, in order to compare the different vertical resolutions. For the two layer case (not shown), the spectra approach -3 slopes at large wavenumbers. However, as the vertical resolution of the vertically discretized simulations increases, the spectra approach a -5/3 slope up to a wavenumber that increases with vertical resolution.

Plotted in the inset of Figure 2.5 are "roll-off" wavenumbers K_{rolloff} (defined to be where the spectral slope of the KE spectrum drops to $K^{-7/3}$) against $K_{\delta z} = f/(N\delta z)$ for each $\delta z = H/\mathcal{N}$. The dependence of K_{rolloff} on $K_{\delta z}$ is roughly linear with a best fit slope of 0.34 (indicated by the dashed line), which means that in order to resolve a wavenumber $K_{\max}$, a vertical grid scale spacing $\delta z \leq 0.34 f/(NK_{\max})$ is required.

The kinetic energy spectra at depths throughout the flow for both the 64-level simulation (dashed lines) and the Blumen model simulation (solid lines) are shown in Figure 2.6. The Blumen simulation is normalized and averaged in the same way as the vertically discrete interior QG solution, and only three of its levels are plotted. The 64 level simulation is clearly a good representation of the nonlinear Eady model at this horizontal resolution; at higher horizontal resolutions, however, the spectrum will fail to resolve smaller horizontal scales unless its vertical resolution is increased.

The implied resolution requirements are similar to those suggested by Barnier et al. (1991), who argued that it is necessary to horizontally resolve the smallest baroclinic deformation scale. By contrast, here the vertical resolution must be suf-

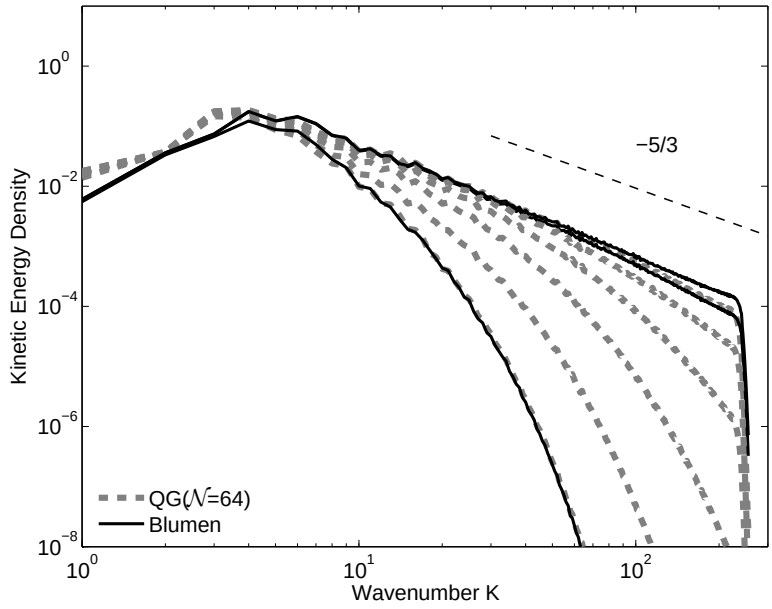

Figure 2.6: Comparison of kinetic energy density in the Blumen model versus the standard QG formulation with 64 layers. The dashed gray lines are KE density at the mid-depths of layers z_1, z_2, z_4, z_8, z_{16} and z_{32} in the layered QG model, while the solid black lines are KE density at $z = 0$, $z = z_1$ and $z = z_{32}$ in the Blumen model.

ficiently fine in order for those horizontally included scales to accurately represent the surface temperature dynamics.

2.4 Simplified models

Now we will consider two simplified models in order to understand the interaction between the surface and interior dynamics. The first model is a finite depth SQG (fSQG) model with passive interior and bottom dynamics, which shows the transition from 2D dynamics at large scales to (infinite depth) SQG-like dynamics at small scales. The second is a model with an SQG surface mode $\hat{\theta}^T$ and a

barotropic interior mode $\hat{q}_0$, which shows how interior and surface spectra coexist with each other.

2.4.1 Finite depth SQG

The simplest surface QG model is obtained when one takes $q = 0$ in (1.5a) and $\theta^B = 0$ in (1.5c), as considered by Tulloch and Smith (2006) and Muraki and Snyder (2007). In order to isolate the depth limited uniform PV flow, one must also assume that β, $\nabla\Theta$, and $\boldsymbol{U}_m$ conspire to make $\nabla Q = 0$ to prevent instabilities from energizing q and θ^B. The simplest approach is to set them all to zero and independently force θ^T by a function $\mathcal{F}$. Then the equation of motion is

$$\partial_t \hat{\theta}^T + \hat{J}(\hat{\psi}^T, \hat{\theta}^T) = \mathcal{F} - \mathcal{D}, \tag{2.15}$$

where the streamfunction $\hat{\psi}^T$ is

$$\hat{\psi}^T(\boldsymbol{K}, t) = \frac{H}{\mu \tanh \mu} \hat{\theta}^T, \tag{2.16}$$

and $\mathcal{D}$ represents some form of drag. At large scales ($\mu \ll 1$) the temperature is related to the streamfunction like $\hat{\theta}^T \simeq H^{-1}\mu^2\ \hat{\psi}^T$, while at small scales, or $\mu \gg 1$, the inversion is approximately $\hat{\theta}^T \simeq H^{-1}\mu\ \hat{\psi}^T$. Thus the relation between the streamfunction and the advected temperature transitions from a QG/2D-like inversion at large scales, to an SQG-like inversion at small scales, with the transition occurring at the wavenumber $\mu = 1$ (*i.e.,* at the deformation wavenumber). A snapshot of the flow is plotted in Figure 2.7, which shows that the large scales resemble a two dimensional flow, conserving filamentary vorticity, while at the

small scales there is significant roll-up of secondary vortices.

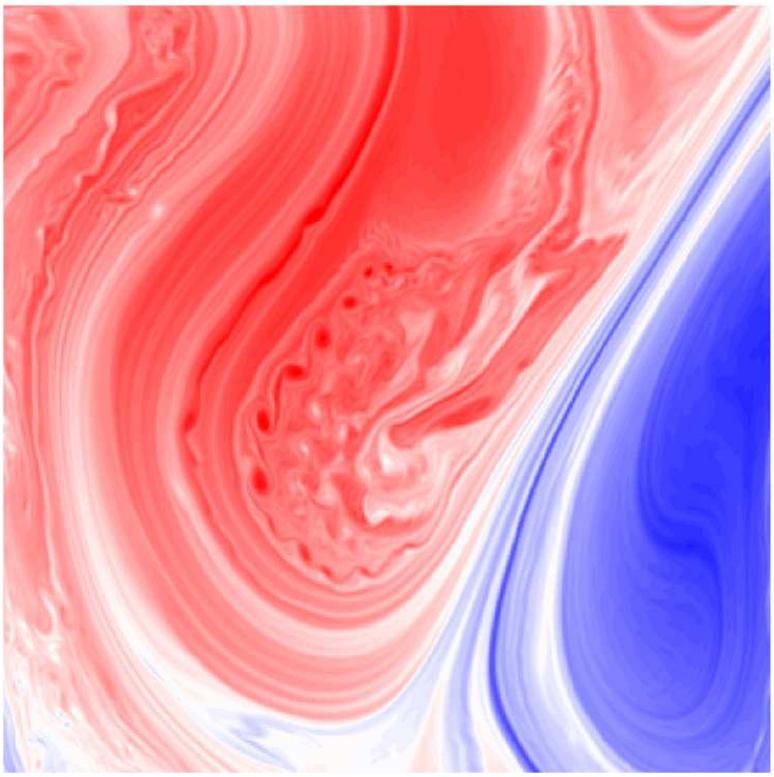

Figure 2.7: Snapshot of a piece of a fSQG temperature field with color axis varying from -1 (blue) to +1 (red).

Barotropic instability

The large scale filamentary and small scale roll-up features in Figure 2.7 can be understood by comparing the barotropic instability of a 2D vorticity filament with an fSQG temperature filament. Following (Held et al., 1995), we note that the Charney-Stern-Pedlosky criterion (Pedlosky, 1987) requires a sign change in in $\partial_y \theta$ in order for instability to develop. The simplest such configuration that is unstable

is a Gaussian filament

$$\Theta^T = B_0 \, \mathrm{e}^{-(y/\mathcal{L})^2}. \tag{2.17}$$

To compute the instability of this filament we linearize Equation (2.15) about the mean state Θ^T, then insert a zonal wave solution of the form $\mathrm{e}^{\mathrm{i(kx-\omega t)}}$:

$$-\omega\hat{\theta}^T + kU(y)\hat{\theta} + k\hat{\psi}\partial_y\Theta^T = 0,$$

which, when the y-dependence is discretized with a centered finite differences, becomes a generalized eigenvalue problem for the growth rate.

Figure 2.8 shows the barotropic growth rates for various fluid depths H given the initial state in Equation (2.17) (with $f/N = 1$). The zonal wavenumber k is scaled by the length scale $\mathcal{L}$ and the growth rate scales with $B_0\mathcal{L}^{-1}$. The growth rate for a Gaussian filament of vorticity ζ in 2D flow,

$$\zeta = Z_0 \, \mathrm{e}^{-(y/\mathcal{L})^2},$$

where Z_0 is the magnitude of the vorticity, is also plotted in Figure 2.8 (solid black line). The key point, as noted by Held et al. (1995), is that the 2D growth rate scales with Z_0 and not with $\mathcal{L}$, so while filaments are created in 2D turbulence, they conserve vorticity and are dominated by large scale shears and strain. Conversely, SQG filaments conserve temperature, but the vorticity and unstable growth rate increase as the filament is stretched, scaling as $B_0\mathcal{L}^{-1}$. In fSQG the growth rate scales like SQG when $\mu > 1$ and like 2D (divided by H) when $\mu < 1$, so the growth rates for $H \geq 1$ in Figure 2.8 are non-dimensionalized by $B_0\mathcal{L}^{-1}$ and the growth rate for $H = 0.1$ is non-dimensionalized by B_0H^{-1}. The fSQG instability spans

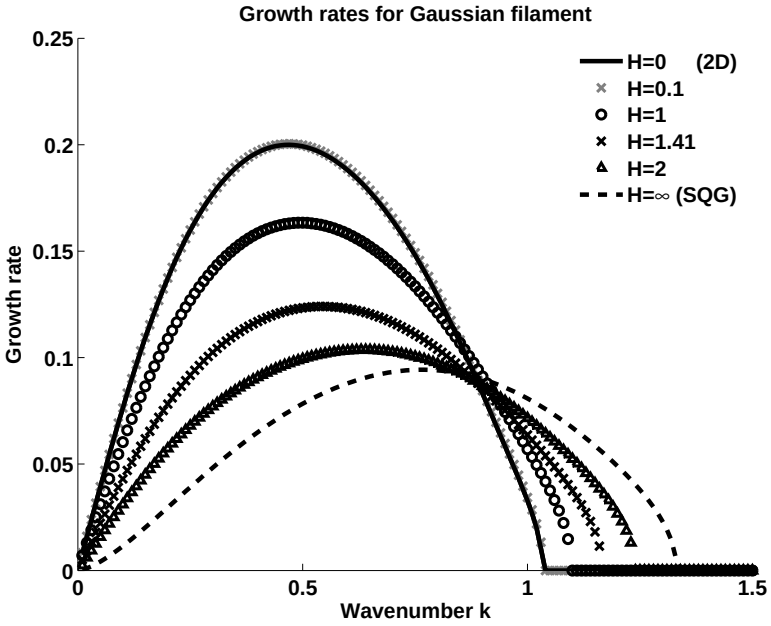

Figure 2.8: Growth rates for a Gaussian temperature filament for fluid depths $H = 0$ (two dimensional), finite H (fSQG), and $H = \infty$ (SQG). The wavenumber is nondimensionalized by $\mathcal{L}^{-1}$, growth rates are non-dimensionalized by $B_0\mathcal{L}^{-1}$ for SQG and fSQG (when $H \geq 1$), by Z_0 for 2D, and by $B_0\mathcal{H}^{-1}$ for $H = 0.1$.

the region between 2D and SQG, with the $H = 0.1$ growth rate indistinguishable from 2D.

Energy spectrum

The forward cascades of Equation (2.15) results in spectral slopes that can be predicted as follows. We define spectral densities of the streamfunction at the surface $\mathcal{P}(K)$, total volume integrated energy $\mathcal{E}_S(K)$ and available potential energy

at the surface $\mathcal{T}(K)$ as

$$\int \mathcal{P}(K)\ dK = \frac{1}{2}\overline{(\hat{\psi}^T)^2}^S,$$
$$\int \mathcal{E}_S(K)\ dK = \frac{1}{2}\frac{f^2}{N^2}\overline{\hat{\psi}^T\hat{\theta}^T}^S,$$
$$\int \mathcal{T}(K)\ dK = \frac{1}{2}\frac{f^2}{N^2}\overline{(\hat{\theta}^T)^2}^S,$$

where overlines indicate integrals over the surface. The densities are related by

$$\mathcal{E}_S(K) = \frac{f^2}{N^2}H^{-1}\mu\tanh\mu\ \mathcal{P}(K),$$
$$\mathcal{T}(K) = \frac{f^2}{N^2}\left(H^{-1}\mu\tanh\mu\right)^2\ \mathcal{P}(K)$$

The rate of energy dissipation in the inertial range due to the forward potential energy cascade is approximately

$$\epsilon_T \simeq \mathcal{T}(K)K\ \tau^{-1}(K) = \text{constant},$$

where $\tau(K)$ is the turbulent timescale which is related to the streamfunction spectrum by $\tau(K) \simeq [K^5\mathcal{P}(K)]^{-1/2}$. Therefore the kinetic energy spectrum is

$$K^2\mathcal{P}(K) = C_T\epsilon_T^{2/3}\left[\tanh\mu\right]^{-4/3}K^{-5/3} \simeq \begin{cases} C_T\epsilon_T^{2/3}K_t^{4/3}\,K^{-3}, & \mu \ll 1 \\ C_T\epsilon_T^{2/3}\,K^{-5/3}, & \mu \gg 1, \end{cases} \tag{2.19}$$

the potential energy spectrum is

$$\mathcal{T}(K) = C_T\epsilon_T^{2/3}\left[\tanh\mu\right]^{2/3}K^{-5/3} \simeq \begin{cases} C_T\epsilon_T^{2/3}K_t^{-2/3}\,K^{-1}, & \mu \ll 1 \\ C_T\epsilon_T^{2/3}\,K^{-5/3}, & \mu \gg 1, \end{cases}$$

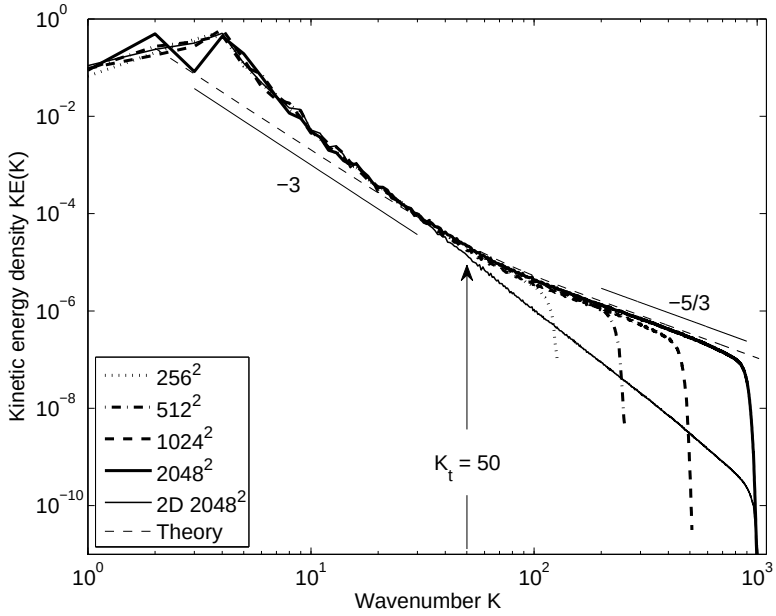

Figure 2.9: fSQG kinetic energy spectra at $z = 0$ with $K_t = 50$, computed at different horizontal resolutions. The thin solid line shows a calculation of regular two-dimensional turbulence for reference, and the thin dashed line is the theoretical spectrum (2.19), with constant chosen to match the large scale spectra.

and the volume integrated energy spectrum is

$$\mathcal{E}_S(K) = C_T \epsilon_T^{2/3} \frac{f}{N} \big[\tanh \mu\big]^{-1/3} K^{-8/3} \simeq \begin{cases} C_T \epsilon_T^{2/3} K_t^{4/3} H\, K^{-3}, & \mu \ll 1 \\ C_T \epsilon_T^{2/3} K_t H\, K^{-8/3}, & \mu \gg 1. \end{cases}$$

Figure 2.9 shows the kinetic energy spectra of a series of simulations with increasing resolution (256^2 to 2048^2) for nondimensional transition wavenumber $K_t = f\mathcal{L}/NH = 50$, where the length scale $\mathcal{L}$ represents the size of the domain. The forcing $\mathcal{F}$ injects energy at $K = 4$ while linear drag $\mathcal{D} \sim \hat{\theta}$ dissipates large scale energy, and a cutoff filter acts to dissipate enstrophy at the highest wavenumbers. The thin solid line is the corresponding KE spectrum for 2D turbulence and

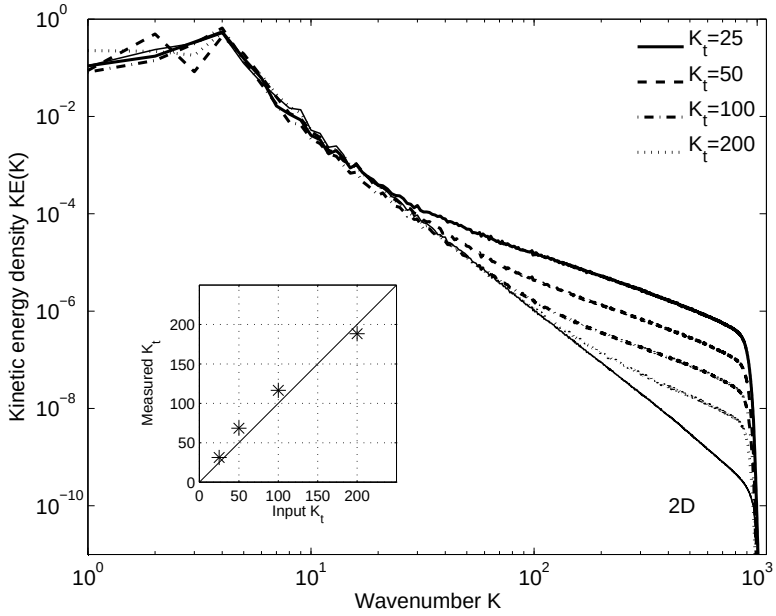

Figure 2.10: fSQG kinetic energy spectra $\mathcal{KE}(K)$ at $z = 0$ with $K_t = 25$, 50, 100, and 200 at 2048^2 resolution. The thin solid line is the spectrum from a simulation of standard two-dimensional turbulence, shown for reference. The inset plot shows the measured transition wavenumber compared to the input value K_t. See text for details.

the thin dashed line shows the predicted spectrum in (2.19). Figure 2.10 shows the kinetic energy spectra for a series of simulations with increasing K_t, with the forcing normalized for each so that $K_t \int \hat{\psi}^T \mathcal{F}(K) dK = 1$. The inset shows measured transition wavenumbers, defined as the wavenumber where the slope becomes shallower than $K^{-7/3}$ (a somewhat arbitrary choice) versus K_t.

The fSQG spectra decay with height away from the surface where $\hat{\theta}^T$ is defined. Retaining the height dependence in Equation (2.19),

$$\mathcal{KE}(K, z) = K^2 \mathcal{P}(K) \left[\phi^T(K, z)\right]^2$$

allows one to compute the theoretical spectral slope as a function of height and

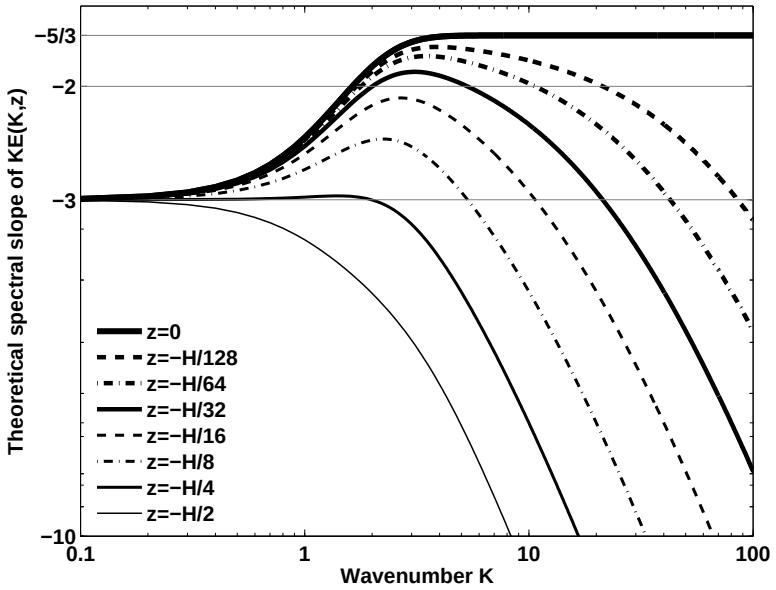

Figure 2.11: Theoretical spectral slopes expected of the fSQG kinetic energy spectrum $\mathcal{KE}(k)$ at heights $z = 0$, $-H/128$, $-H/64$, $-H/32$, $-H/16$, $-H/8$, $-H/4$, and $-H/2$ with $K_t = 1$.

wavenumber magnitude[4]

$$\frac{d}{d\log K}\log[\mathcal{KE}(K,z)] = -\frac{5}{3} + \frac{4}{3}\mu\left[\tanh\mu - \coth\mu\right] + 2\mu\left[\left(\frac{z}{H}+1\right)\tanh\mu\left(\frac{z}{H}+1\right) - \tanh\mu\right],$$

which is plotted against wavenumber K for various heights below the surface in Figure 2.11. The deformation scale is at $K = 1$ (note we have taken $z \in [-H, 0]$ here). All heights except the mid-depth experience some spectral shallowing before eventually decaying at large wavenumbers. The -2 slope is included because fron-

[4]Note that

$$\frac{d}{d\log K}\log[\mathcal{KE}(K,z)] = \frac{K}{\mathcal{KE}}\frac{d}{dK}\mathcal{KE},$$

and that $\mathcal{KE}(K,z) \sim K^{-1/3}[\bar{\phi}^T(K,0)]^{4/3}[\phi^T(K,z)]^2$.

togenesis is thought to produce spectra with -2 slopes, and the difference between -5/3 and -2 is often indistinguishable in observational data.

In summary, depth limited uniform PV flow predicts a transition scale between K^{-3} and $K^{-5/3}$ spectral slopes at wavenumber $K_t = f\mathcal{L}/NH$, which being near the Rossby deformation scale, is larger than the observed atmospheric transition (Nastrom and Gage, 1985).

2.4.2 Independently forced surface and interior dynamics

The uniform potential vorticity model in the previous section can be supplemented with interior vorticity dynamics which results in a superposition of the K^{-3} forward enstrophy cascade of the interior modes and the $K^{-5/3}$ forward energy cascade of the surface mode. Setting $\theta^B = 0$ in (1.5c) but retaining nonzero, barotropic QGPV in (1.5a), $q = q_0$, gives

$$\begin{aligned} \partial_t \hat{\theta}^T + \hat{J}(\hat{\psi}|_{z=z_T}, \hat{\theta}^T) &= \mathcal{F}_\theta - \mathcal{D}_\theta, \quad z = z_T \\ \partial_t \hat{q}_0 + \hat{J}(\langle\hat{\psi}\rangle, \hat{q}_0) &= \mathcal{F}_q - \mathcal{D}_q, \quad z_B < z < z_T \end{aligned}$$

where

$$\hat{\psi}|_{z=z_T} = \hat{\psi}^T + \hat{\psi}_0, \qquad \langle\hat{\psi}\rangle = \frac{\tanh\mu}{\mu}\hat{\psi}^T + \hat{\psi}_0,$$

$\hat{\psi}^T$ is given by (2.16) and $\hat{q}_0 = -K^2\hat{\psi}_0$. In this truncation the inversion treats q as if it is just relative vorticity. Figure 2.12 shows the spectral densities of kinetic energy at the boundary in a series of simulations as the magnitude of $\mathcal{F}_q$ is varied while other parameters are held constant ($K_d = f\mathcal{L}/NH = 25$). In particular, $\mathcal{F}_\theta$ is fixed at 0.04 and $\mathcal{D}_\theta$ and $\mathcal{D}_q$ are fixed linear drags on each advected variable. The effect of larger interior forcing is to increase the total energy

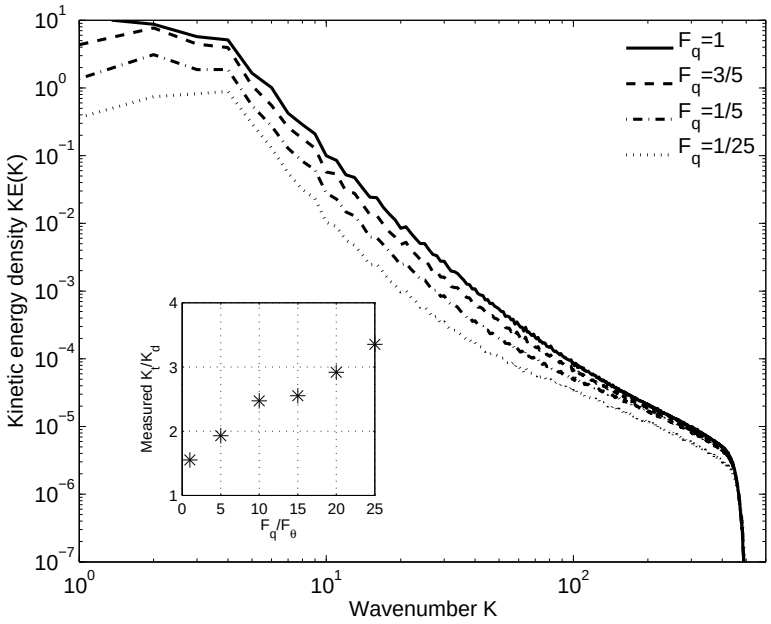

Figure 2.12: Kinetic energy densities at $z = 0$ for surface thermal forcing rate set to 0.04 and interior vorticity forcing rate set to 0.04 (dotted), 0.2 (dash-dot), 0.6 (dashed) and 1 (solid). Inset: Transition wavenumber estimates obtained by measuring where $\mathcal{KE}(k) \sim k^{-7/3}$.

and push the transition wavelength to smaller scale. This superposition of an interior driven K^{-3} forward enstrophy cascade and a surface driven $K^{-5/3}$ forward energy cascade is illustrated in the schematic diagram in Figure 2.13. Surface and interior instabilities may act independently, producing coexisting, superposed forward cascades of surface energy and interior enstrophy. The interior enstrophy cascade dominates at large scales, but yields to the sub-dominant shallow surface energy cascade at wavenumber K_t. In the next chapter we will investigate the factors which set K_t. We will see that including non-uniform potential vorticity solves the problem seen in the fSQG model where the transition wavelength was too large (if depth of the fluid is taken as $H \sim 10$km, the height of the tropopause).

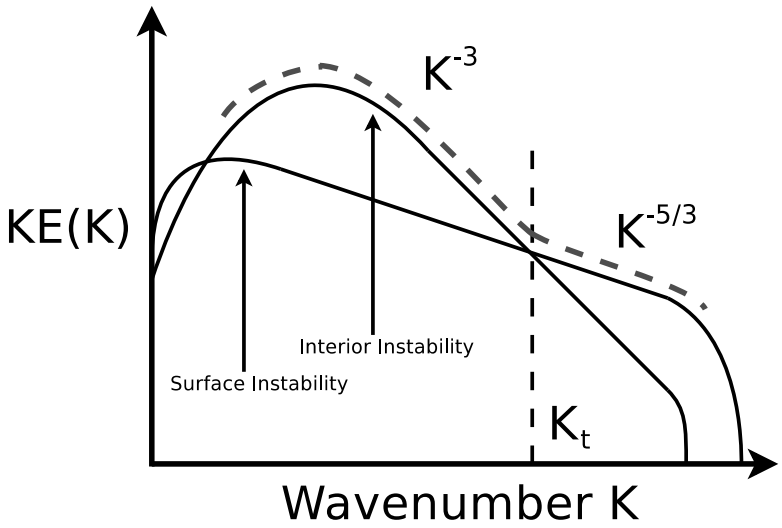

Figure 2.13: Schematic diagram of the coexistence of a forward K^{-3} interior driven enstrophy cascade and a forward $K^{-5/3}$ surface energy cascade, with the total KE at the surface transitioning from a steep slope to a shallow slope at wavenumber K_t.

2.5 Summary

We formulated the solution of the full QG equations in terms of vertical interior and surface modes which solve the associated elliptic inversion problems (2.3). Truncating the interior modes to a computationally manageable set yields an efficient and accurate representation of the full system at all depths.

Next we demonstrated that given Eady forcing and sufficient vertical resolution then the solution given by the layered QG formulation with standard vertical finite differencing for the vortex stretching term converges to the solution given by the Blumen model which explicitly excludes PV driven dynamics. This result is consistent with the Bretherton (1966) argument that a temperature layer is

equivalent to a delta sheet of PV.

Finally we described two simplified models which illustrate interactions between surface dyanmics and interior dynamics. When forced at large scales, depth limited uniform PV flow produces two dimensional dynamics at scales larger than the deformation scale and surface dynamics at scales smaller than the deformation scale. This system is not subject to baroclinic instability by itself. Adding a barotropic vorticity component to such a flow adds the possibility of truncated Charney baroclinic instability between temperature gradients on the boundary and the Coriolis gradient β. However this instability appears to only energize the surface flow and not the interior flow. If both the barotropic flow and the surface flow are energized at large scales then the enstrophy cascade of the barotropic flow cascades forward at K^{-3} and the surface temperature cascades forward at $K^{-5/3}$. The kinetic energy spectrum at the surface is then the superposition of those two spectra, resulting in a transition between K^{-3} and $K^{-5/3}$ that depends on the relative strength of the vorticity forcing to the surface temperature forcing.

Chapter 3

Surface-modal model applied to the atmosphere: the energy spectrum near the tropopause

Here we specialize the SMQG framework to include just enough complexity to address the observed atmospheric energy spectra, at the transition to sub-synoptic scales. The simple model advects the barotropic and baroclinic interior flow, and the upper and lower surface temperatures. In spectral space, the vertical structures for the four variables are separable from their time-dependent parts. Assuming constant stratification N^2, these modes can be easily computed analytically. The resulting model is very similar to one developed by G. Flierl (2007, personal communication), with some differences, but to our knowledge these are the only examples of fully nonlinear, forward model implementations using the decomposition approach. This two-mode, two-surface model (hereafter referred to as the TMTS model) is effectively a hybrid of the Phillips and Eady models, and so can

represent baroclinic instability generated from barotropic-baroclinic interactions (as in the standard two-layer Phillips model), surface-surface interactions (as in the Eady model), and from interactions between either surface and the interior (as in the Charney model of baroclinic instability).

The TMTS model is designed to understand the observed atmospheric energy spectrum at sub-synoptic scales; a corollary is that high vertical resolution is not needed to understand the transition to a shallow spectrum, so long as surface dynamics are explicitly represented. On the other hand, the model may be deficient for applications that require a more realistic representation of the vertical structure of eddy fluxes at the synoptic and planetary scale.

This Chapter is organized as follows. In Section 3.1 observations and previous explanations of the atmospheric energy spectrum are discussed. In Section 3.2 the TMTS model is derived based on the SMQG formulation discussed in Chapter 2 and solutions to the associated (truncated) linear instability problem are presented. The results of a series of nonlinear simulations are presented in Section 3.3, and a theory for the transition scale that is consistent with both simulated and observed data is proposed. Successes and shortcomings of the theory are discussed in Section 3.4.

3.1 Nastrom-Gage/MOZAIC Observations

The horizontal kinetic energy and potential temperature variance spectra near the tropopause, observed during the Global Atmospheric Sampling Program (GASP) and documented in Nastrom and Gage (1985), exhibit a shallow plateau at the largest wavelengths (10,000–3000 km), a steep K^{-3} spectral slope on synoptic

scales ($\approx$ 3000–1000 km), followed by a smooth transition (at a wavelength of about 450 km) to a shallow $K^{-5/3}$ spectral slope on the mesoscales ($\approx$ 200–10 km). The large and synoptic scale parts of the spectra are consistent with stirring by baroclinic instability near the Rossby deformation wavelength, feeding a forward cascade of enstrophy with a K^{-3} slope, as predicted by Charney's theory of geostrophic turbulence (Charney, 1971). The mesoscale shallowing, however, does not fit easily into this picture; the robustness of the synoptic scale slope and its consistency with geostrophic turbulence theory make the mesoscale spectral slope difficult to explain.

The key figure from Nastrom and Gage (1985) (their Figure 3) plots power density spectra of the zonal wind (u^2), meridional wind (v^2) and the potential temperature (θ^2) as functions of horizontal wavenumber (meridional wind and potential temperature are offset by 1 and 2 orders of magnitude, respectively). Below wavelengths of about 5000 km, the zonal and meridional wind spectra are nearly identical, implying isotropic kinetic energy (KE, equal to $(u^2+v^2)/2$) in the synoptic scales and below. The potential temperature spectrum exhibits the same spectral slopes and spectral break, but is about half the magnitude of the spectra of the winds. The APE, equal to $(g/2N\theta_0)^2\theta^2$, where g is gravity, N is the buoyancy frequency and θ_0 a reference potential temperature, is therefore very nearly in equipartition with the kinetic energy[1]. In the K^{-3} range, equipartition between KE and APE at each scale is also consistent with the predictions of geostrophic turbulence[2]. High-resolution general circulation and weather forecasting models

[1]Using typical upper tropospheric values $\theta_0 = 300$ K, $N = 10^{-2}$ s^{-1}, and $g = 9.8$ ms^{-2}, APE $\sim 2\,\theta^2$, and so the dimensional prefactor just accounts for the drop in magnitude of the potential temperature relative to the winds.

[2]In quasi-geostrophic theory, KE/APE $\sim (Nh_e/f\ell_e)^2$, where ℓ_e and h_e are the (variable) horizontal and vertical scales, respectively, of the eddying motion. Charney argued that, neglecting the influence of boundaries or inhomogeneities in the stratification, the forward cascade of po-

yield similar results, with equipartition in the -3 range, and a shallowing to $-5/3$ in the mesoscales (Hamilton et al., 2008; Takahashi et al., 2006; Skamarock, 2004; Koshyk and Hamilton, 2001)

Recent observations from the MOZAIC program (Marenco et al., 1998) have been shown to give identical kinetic energy spectra to the GASP data (Lindborg, 1999). The MOZAIC velocity (u^2 and v^2) and temperature (θ^2) spectra are recomputed here and plotted in Figure 3.1 in the same format as Figure 3 of (Nastrom and Gage, 1985). The meridional velocity and temperature spectra are shifted to the right by one and two decades for clarity. The computed spectra u^2, v^2 and θ^2 are plotted in red, green, and magenta respectively. The solid black line is Lindborg's best fit curve $E(K) = d_1 K^{-5/3} + d_2 K^{-3}$, where $d_1 = 9.1 \times 10^{-4}$ and $d_2 = 3 \times 10^{-10}$, and is the same in each variable. The black dashed curves correspond to best fit approximations, by visual inspection, assuming a spectrum of the form $E(K) = c_1 K^{-5/3} + c_2 K^{-2} + c_3 K^{-3}$ as proposed by Charney (1973). For u^2, the approximating coefficients are $c_1 = 7 \times 10^{-4}$, $c_2 = 1.4 \times 10^{-5}$, and $c_3 = 2.2 \times 10^{-10}$. The ratios between c_1 and c_2 are such that the $K^{-5/3}$ contribution begins to dominate the K^{-2} contribution at 800km. Similarly, the ratios of c_2 to c_3 indicate that K^{-3} dominates K^{-2} down to 400km. Therefore if there is any K^{-2} contribution to u^2 it is negligible. For v^2, the coefficients are $c_1 = 8 \times 10^{-4}$, $c_2 = 1.2 \times 10^{-5}$, and $c_3 = 3.5 \times 10^{-10}$, which means that K^{-3} dominates K^{-2} down to 200km and $K^{-5/3}$ dominates K^{-2} at scales smaller than 1800km.

The temperature spectrum θ^2 has a different shape, with coefficients $c_1 = 1.5 \times 10^{-4}$, $c_2 = 1.8 \times 10^{-5}$, and $c_3 = 0.5 \times 10^{-10}$, indicating that neither K^{-3}

tential enstrophy should be isotropic in the space $(x, y, Nz/f)$. Thus, in the forward cascade, each scale of eddy motion will maintain a constant aspect ratio $\ell_e/h_e \sim N/f$, independent of scale, so KE/APE ~ 1.

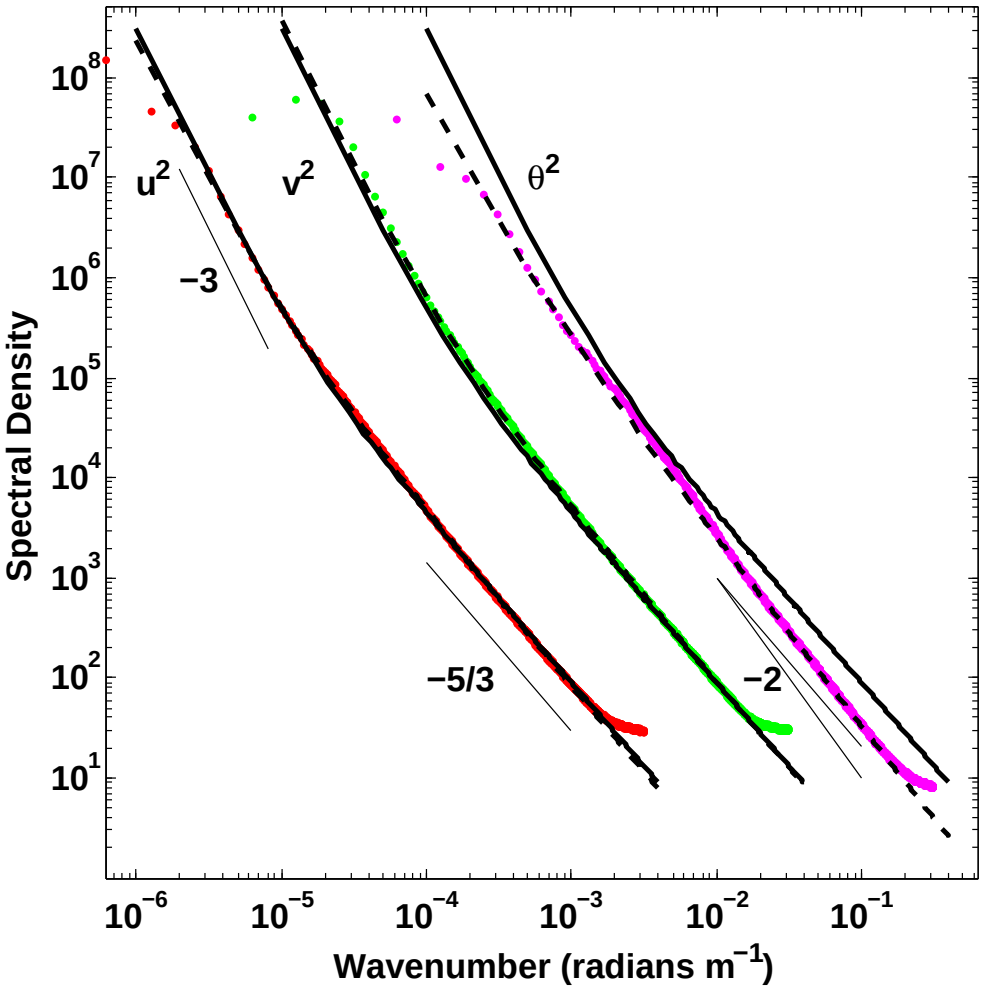

Figure 3.1: The MOZAIC zonal and meridional velocity spectra (with units m^3s^{-2}) and the potential temperature spectrum (with units $°K^2m\ rad^{-1}$). Solid black lines are Lindborg's best fit curve, dashed black lines are best fit lines (see text for details).

nor $K^{-5/3}$ are a better fit than K^{-2} in the mesoscales. This apparent K^{-2} temperature dependence may be an artifact of the data processing methods. Aircraft flights occasionally make abrupt altitude or pressure changes which affects potential temperature much more than velocity. Nastrom and Gage (1985) computed their large scale spectral ranges independently of their small scale spectral ranges, and took care to smooth over adjacent flight segments, which was not done here. All the spectra shown in Figure 3.1 were computed using 5000km flight segments[3]. Rob Scott (2008, personal communication) has also computed the MOZAIC velocity spectra, but not the temperature spectra, and suggested that the temperature spectra might be sensitive to changes in altitude within flights and between different flights. In any case, we will assume here that the temperature spectrum in Nastrom and Gage (1985) is correct.

3.1.1 Previous explanations of observed spectrum

Numerous theories for the mesoscale spectrum have been suggested over the past two decades (Lilly, 1989; Vallis et al., 1997; Dewan, 1979; VanZandt, 1982; Koshyk et al., 1999; Tung and Orlando, 2003a; Lindborg, 2005; Kitamura and Matsuda, 2006). Tung and Orlando (2003a) summarize all these theories, and put forward their own. Tulloch and Smith (2006) also revisit the proposed mechanisms for the mesoscale shallowing, and propose a new one, based on the finite-depth SQG (fSQG) model that captures many aspects of the observations. The model is motivated by the following observations: (i) the near-universality of the spectrum in different parts of the world implies that synoptic scale baroclinic instability is

[3]The majority of flights were in the mid-latitudes, only flights longer than 5000km were considered and segments were only used if the maximum pressure was less than 300mb.

likely the forcing of both the K^{-3} and $K^{-5/3}$ ranges of the spectrum (Tung and Orlando, 2003a), (ii) the $K^{-5/3}$ part of the spectrum is due to a forward energy cascade (Cho and Lindborg, 2001; Tung and Orlando, 2003b), and (iii) both the K^{-3} and $K-5/3$ parts of the spectrum belong to the same inertial range with the transition determined by relative magnitudes of the energy and enstrophy fluxes (Tung and Orlando, 2003a). The physical mechanism proposed is that advection of temperature perturbations at the tropopause leads to a forward cascade of temperature variance, resulting in $K^{-5/3}$ kinetic and potential energy spectra at mesoscales, as predicted by surface quasi-geostrophic theory (SQG, Blumen, 1978; Held et al., 1995). This is rationalized by the analysis of Juckes (1994), who showed that tropopause temperature anomalies account for about 80% of the tropospheric eddy field. The novel aspect of Tulloch and Smith (2006) was the demonstration that by limiting surface quasi-geostrophic flow to a finite depth, a natural transition scale emerges, and when the flow is forced at large scale, the kinetic energy spectrum is -3 at scales larger than this transition and $K^{-5/3}$ below it. The transition length scale ($\sim NH/f$) is the scale above which the surface signals can 'feel' the lower boundary. The large-scale limit is that of barotropic flow, and so follows the predictions of two-dimensional turbulence, while the small-scale limit, where the vertical extent of temperature signals is much less than H, is that of surface quasi-geostrophic flow.

The fSQG model is compelling because it leads to a forward cascade of vortical energy, consistent with observations (Cho and Lindborg, 2001; Cho et al., 1999), and the cascade can be generated by large-scale forcing such as baroclinic instability, ubiquitous throughout the midlatitudes, thereby accounting for the universality of the spectra (Nastrom and Gage, 1985). Taken as complete, however, the

model has the following deficiencies: (i) it fails to explain the available potential energy spectrum at synoptic scales (finite-depth surface quasi-geostrophic flow has no significant potential energy at large scales); (ii) it predicts a transition scale that is larger than that observed; and (iii) it predicts an evanescent spectrum at small scales when moving down into the troposphere (mid-level spectral observations in the troposphere are rare, but there is no evidence for evanescent decay of energy). These deficiencies, it is shown here, are removed when interior potential vorticity anomalies are included in the flow.

3.2 Baroclinic model

To generate a numerical model that will aid understanding of the atmospheric energy spectrum, the following simplifying assumptions are made: (i) horizontal boundary conditions are taken to be periodic, consistent with the assumption of horizontal homogeneity in the synoptic scales and below; (ii) the vertical structure of the interior flow can be represented with the gravest two standard vertical modes (barotropic and baroclinic); (iii) the stratification N^2 is constant in the troposphere and infinite above, so that the tropopause itself is a rigid lid (this assumption can be relaxed to a finite stratification jump following Juckes, 1994); and (iv) the mean velocity is zonal, horizontally constant and projects onto the baroclinic and surface modes (with no barotropic component).

3.2.1 Truncated equations

Modal representation

Assumption (i) allows a Fourier representation in the horizontal, so the full streamfunction can be written as in Equation (2.6). Assumption (ii) allows for the expansion of the interior part in modes $\hat{\psi}^{\mathrm{I}}(\boldsymbol{K}, z, t) = \hat{\psi}^{\mathrm{bt}}(\boldsymbol{K}, t) + \hat{\psi}^{\mathrm{bc}}(\boldsymbol{K}, t)\phi(z)$ where $\phi(z)$ is the first baroclinic mode, i.e. the gravest, non-constant eigenfunction solution to[4]

$$\Gamma\phi = -\lambda^2\phi, \quad \frac{d\phi}{dz}(0, H) = 0. \tag{3.1}$$

It is straightforward, but cumbersome, to use more vertical modes in the interior. With assumption (iii), the mode is

$$\phi(z) = \sqrt{2}\cos\left(\frac{\pi z}{H}\right), \quad \lambda = \frac{\pi f}{NH}. \tag{3.2}$$

Note for future reference that $\langle\phi\rangle = \langle\phi^3\rangle = 0$ and $\langle\phi^2\rangle = 1$, where $\langle\cdot\rangle = H^{-1}\int_0^H \cdot\, dz$ is shorthand for a vertical average.

Recall that in the spectral domain, the surface inversion problems (2.8) and (2.9) have a time independent vertical structure, and so

$$\hat{\psi}^T(\boldsymbol{K}, z, t) = \hat{\psi}^T(\boldsymbol{K}, t)\phi^T(K, z)$$

and

$$\hat{\psi}^B(\boldsymbol{K}, z, t) = \hat{\psi}^B(\boldsymbol{K}, t)\phi^B(K, z).$$

Unlike the interior modes, the surface modes depend on the magnitude of the

[4]The subscripted mode numbers in (2.6) have been dropped here to simplify the notation since there is only one non-constant vertical mode. Also, we have set $z_B = 0$ and $z_T = H$.

wavevector, K. Note also that $\phi^T(H) = 1$ and $\phi^B(0) = 1$, so that $\hat{\psi}^T(\boldsymbol{K}, H, t) = \hat{\psi}^T(\boldsymbol{K}, t)$ and $\hat{\psi}^B(\boldsymbol{K}, 0, t) = \hat{\psi}^B(\boldsymbol{K}, t)$. Since N^2 is constant, the solutions are easily computed; they are

$$\phi^T(z) = \cosh\left(\mu \frac{z}{H}\right) \operatorname{sech} \mu,$$
$$\phi^T(z) = \cosh\left(\mu \frac{z-H}{H}\right) \operatorname{sech} \mu,$$

recall that $\mu = KNH/f$.

Given the surface modes, the top and bottom temperature fields are related to the streamfunction by

$$\hat{\theta}^T(\boldsymbol{K}, t) = \quad \frac{\mu}{H} \tanh \mu \ \hat{\psi}^T(\boldsymbol{K}, t), \tag{3.4a}$$
$$\hat{\theta}^B(\boldsymbol{K}, t) = -\frac{\mu}{H} \tanh \mu \ \hat{\psi}^B(\boldsymbol{K}, t). \tag{3.4b}$$

Expanding the potential vorticity in interior modes

$$\hat{q}(\boldsymbol{K}, z, t) = \hat{q}^{\mathrm{bt}}(\boldsymbol{K}, t) + \hat{q}^{\mathrm{bc}}(\boldsymbol{K}, t)\phi(z)$$

yields

$$\hat{q}^{\mathrm{bt}}(\boldsymbol{K}, t) = -K^2 \ \hat{\psi}^{\mathrm{bt}}(\boldsymbol{K}, t) \tag{3.5a}$$
$$\hat{q}^{\mathrm{bc}}(\boldsymbol{K}, t) = -K^2 \frac{\mu^2 + \pi^2}{\mu^2} \ \hat{\psi}^{\mathrm{bc}}(\boldsymbol{K}, t). \tag{3.5b}$$

Given the potential vorticity and surface temperature fields, (3.4) and (3.5) can be inverted to give the four streamfunction components, and the full streamfunction is summed as in (2.6). The prognostic equations for the barotropic and baroclinic

potential vorticity components in (3.5) are derived by expanding the streamfunction and potential vorticity in (1.5a) using (2.6) and (3.5), then projecting onto the barotropic mode by integrating in the vertical, and onto the baroclinic mode by integrating ϕ times the expression. Each surface temperature equation is obtained by evaluating the full advecting streamfunction (2.6) at the vertical level of the surface of interest.

Mean field projections

The last step is to project the mean velocity onto the truncated vertical representation. The mean zonal velocity must in general satisfy (1.4) in the interior and (1.6) at the upper and lower boundaries (but we set $V = 0$), and to be consistent with the dynamic variables q and θ we decompose the mean zonal velocity into interior and surface components $U(z) = U^I(z) + U^S(z)$. The relationships among the mean fields, however, are somewhat different than that between the eddy fields, due to the fact U is independent of x and y (i.e. mean relative vorticity is neglected, consistent with the assumption of local homogeneity). Assumption (iv) gives us that $U^I = U^{\rm bc}\phi(z)$, where $\phi(z)$ is given by (3.2). Derivatives of U^I evaluated at 0 and H vanish and therefore U^S must satisfy the boundary conditions, given arbitrary mean temperature gradients Θ^T_y and Θ^B_y (where subscript y denotes the meridional derivative). We thus demand that the surface component solves

$$\Gamma U^S = A, \qquad \frac{dU^S}{dz}(H) = -\Theta^T_y, \qquad \frac{dU^S}{dz}(0) = -\Theta^B_y.$$

In analogy with the decomposition of the eddy components in (2.2), (2.8) and (2.9), one might expect to demand that $\Gamma U^S = 0$. However, this can only be satisfied if $\Theta^T_y = \Theta^B_y$ (therefore it would also be impossible to separate U^S into

$U^T + U^B$). Instead, here we demand that the right hand side, A, be a constant, and that the vertical mean of the surface velocity vanish, $\langle U^S \rangle = 0$. The result is that

$$A = \left(\frac{f^2}{HN^2} \right) \Delta\Theta_y, \quad \Delta\Theta_y \equiv \Theta_y^T - \Theta_y^B,$$

which vanishes only when upper and lower temperature gradients are equal, and

$$U^S(z) = -\Theta_y^B \left(z - \frac{H}{2} \right) + \Delta\Theta_y \left(\frac{z^2}{2H} - \frac{H}{6} \right). \tag{3.6}$$

The full mean velocity is therefore $U(z) = U^{\rm bc}\phi(z) + U^S(z)$. [A Green's function approach to the mean velocity problem is illustrated in Appendix A.3.]

That $A \neq 0$ means that the surface velocity field U^S induces an interior mean PV gradient; the total mean potential vorticity gradient is therefore

$$Q_y = \beta - \Gamma U = \beta + L_{\rm D}^{-2} \left[H\Delta\Theta_y + \sqrt{2}\pi^2 U^{\rm bc} \cos\left(\frac{\pi z}{H} \right) \right], \tag{3.7}$$

where $L_{\rm D} = NH/f$ is the deformation scale and (3.2) was used (note that the first baroclinic deformation wavenumber, defined in (3.2), is $\lambda = \pi/L_{\rm D}$).

TMTS evolution equations

Putting all the prior results together, the full set of spectral prognostic equations can now be written

$$\partial_t \hat{\theta}^T + \hat{J}(\hat{\psi}|_{z=H}, \hat{\theta}^T) + ik\left[U(H)\hat{\theta}^T + \Theta_y^T \hat{\psi}|_{z=H}\right] = 0, \tag{3.8a}$$

$$\partial_t \hat{\theta}^B + \hat{J}(\hat{\psi}|_{z=0}, \hat{\theta}^B) + ik\left[U(0)\hat{\theta}^B + \Theta_y^B \hat{\psi}|_{z=0}\right] = rK^2 \hat{\psi}|_{z=0}, \tag{3.8b}$$

$$\begin{aligned}\partial_t \hat{q}^{\mathrm{bt}} + \hat{J}(\langle\hat{\psi}\rangle, \hat{q}^{\mathrm{bt}}) + \hat{J}(\langle\phi\hat{\psi}\rangle, \hat{q}^{\mathrm{bc}}) \\ + ik\left[\langle\phi U\rangle\hat{q}^{\mathrm{bc}} + (\beta - \Gamma U^S)\langle\hat{\psi}\rangle + \lambda^2 U^{\mathrm{bc}}\langle\phi\hat{\psi}\rangle\right] = 0,\end{aligned} \tag{3.8c}$$

$$\begin{aligned}\partial_t \hat{q}^{\mathrm{bc}} + \hat{J}(\langle\phi\hat{\psi}\rangle, \hat{q}^{\mathrm{bt}}) + \hat{J}(\langle\phi\phi\hat{\psi}\rangle, \hat{q}^{\mathrm{bc}}) \\ + ik\left[\langle\phi U\rangle\hat{q}^{\mathrm{bt}} + \langle\phi\phi U\rangle\hat{q}^{\mathrm{bc}} + (\beta - \Gamma U^S)\langle\phi\hat{\psi}\rangle + \lambda^2 U^{\mathrm{bc}}\langle\phi\phi\hat{\psi}\rangle\right] = 0\end{aligned} \tag{3.8d}$$

where $\hat{J}$ is shorthand for the sum over wavenumbers of the Jacobian terms, and the streamfunction evaluated at the upper and lower surfaces, respectively, is

$$\begin{aligned}\hat{\psi}|_{z=H} &= \hat{\psi}^{\mathrm{bt}} - \sqrt{2}\hat{\psi}^{\mathrm{bc}} + \hat{\psi}^T + \hat{\psi}^B \operatorname{sech}\mu \\ \hat{\psi}|_{z=0} &= \hat{\psi}^{\mathrm{bt}} + \sqrt{2}\hat{\psi}^{\mathrm{bc}} + \hat{\psi}^T \operatorname{sech}\mu + \hat{\psi}^B.\end{aligned}$$

The vertical integrals and projections of the total streamfunction and mean shear onto the baroclinic mode (e.g. $\langle\phi\hat{\psi}\rangle$) are derived and stated in the Appendix A.4.

Equations (3.8) sacrifice the ability to represent high vertical modes of the interior flow, but retain an accurate description of surface motions, even when such motions have very small vertical penetration into the interior. The projection onto a truncated set of interior modes, plus surface modes, allows for a compact model that can be numerically integrated with much greater efficiency than a high-

vertical resolution gridded model. The goal in developing this model is twofold: (1) to derive a simple model that retains all basic types of baroclinic instability, and (ii) to demonstrate that augmentation of the two-layer model with surface modes is sufficient to explain the spectrum of energy in the atmospheric mesoscales.

3.2.2 Linear instabilities

Assuming horizontally constant, baroclinic zonal mean flow, the quasi-geostrophic equations (1.5) are linearly unstable to small perturbations under at least one of the following conditions (Charney and Stern, 1962; Pedlosky, 1964): (i) $Q_y = 0$, and Θ_y^T and Θ_y^B are both nonzero and have the same sign (as in the model of Eady, 1949); (ii) Q_y changes sign in the interior and the boundary gradients are zero (as in the model of Phillips, 1951); or (iii) $Q_y \neq 0$ and either the upper surface gradient has the same sign, or the lower surface gradient has the opposite sign as Q_y (as in the model of Charney, 1947). The standard two-layer model of Phillips admits only instabilities of the second type, yet has arguably been more widely used than either the Charney or Eady model, due to it's analytical tractability, wide parameter range possibilities, inclusion of β and the ease with which it can be numerically simulated. The TMTS model (3.8) derived in section 2 is intended to retain those positive features of the two-layer model while additionally admitting the two missing instability types (i and iii). Here we have the following goals: to demonstrate that all of types (i-iii) are captured in the two-mode, two-surface model; and to compute the linear instability of the flow that will be used to drive the nonlinear turbulence simulations presented in Section 3.3.

To compute the baroclinic instability of the TMTS model, the nonlinear terms

are neglected and a normal-mode wave solution is assumed:

$$(\hat{\psi}^T, \hat{\psi}^B, \hat{\psi}^{\rm bt}, \hat{\psi}^{\rm bc}) = \mathfrak{Re}\ \boldsymbol{\varphi} \exp[-i\omega t],$$

where $\boldsymbol{\varphi} = (\hat{\varphi}^T, \hat{\varphi}^B, \hat{\varphi}^{\rm bt}, \hat{\varphi}^{\rm bc})$ and the meridional wavenumber ℓ is set to 0. Specifically, we solve the eigenvalue problem $c\boldsymbol{\varphi} = \mathsf{A}\boldsymbol{\varphi}$ where A is a 4×4 matrix (given in Appendix A.5) and $c = \omega/k$. The growth rate $\omega_i = kc_i$ of unstable modes depends on β, the magnitude of the internal velocity shear $U^{\rm bc}$, and on the boundary temperature gradients $\Theta_y^{T,B}$. We nondimensionalize the parameter space of the problem with horizontal length-scale $L_{\rm D}$, vertical length scale H and a velocity-scale U_0. Horizontal wavenumbers K are already expressed nondimensionally as $\mu = KL_d$ almost everywhere they appear. The nondimensional Coriolis gradient is $\tilde{\beta} \equiv \beta L_d^2/U_0$ and the velocity parameters of the problem are $U^{\rm bc}/U_0$ and $(H/U_0)\Theta_y^{T,B} = -(H/U_0)U_z^{T,B}$.

Figures 3.2 and 3.3 show numerically-computed growth rates and amplitudes of eigenfunctions of the linearized TMTS model as functions of μ and $\tilde{\beta}$. Figure 3.2a shows the growth rates given equal, nonzero boundary temperature gradients $(H/U_0)\Theta_y^T = (H/U_0)\Theta_y^B = -1$, and zero interior shear, $U^{\rm bc} = 0$. The Eady problem corresponds to the line $\tilde{\beta} = 0$, and along this line, $\max(\omega_i)L_d/U_0 \approx 0.31$, as expected. For $\tilde{\beta} \neq 0$ boundary gradients interact with $Q_y = \beta$ in the interior which results in Charney type instabilities at small scales and a truncated Green (1960) mode at large scales (see also Lindzen, 1994, who considered the effects of altering the mean state to retain 0 interior PV with β). Figure 3.2b shows the amplitudes, as functions of height, that correspond to the fastest growing modes at various locations in the $(\mu, \tilde{\beta})$ plane, as indicated by symbols in Figure 3.2a.

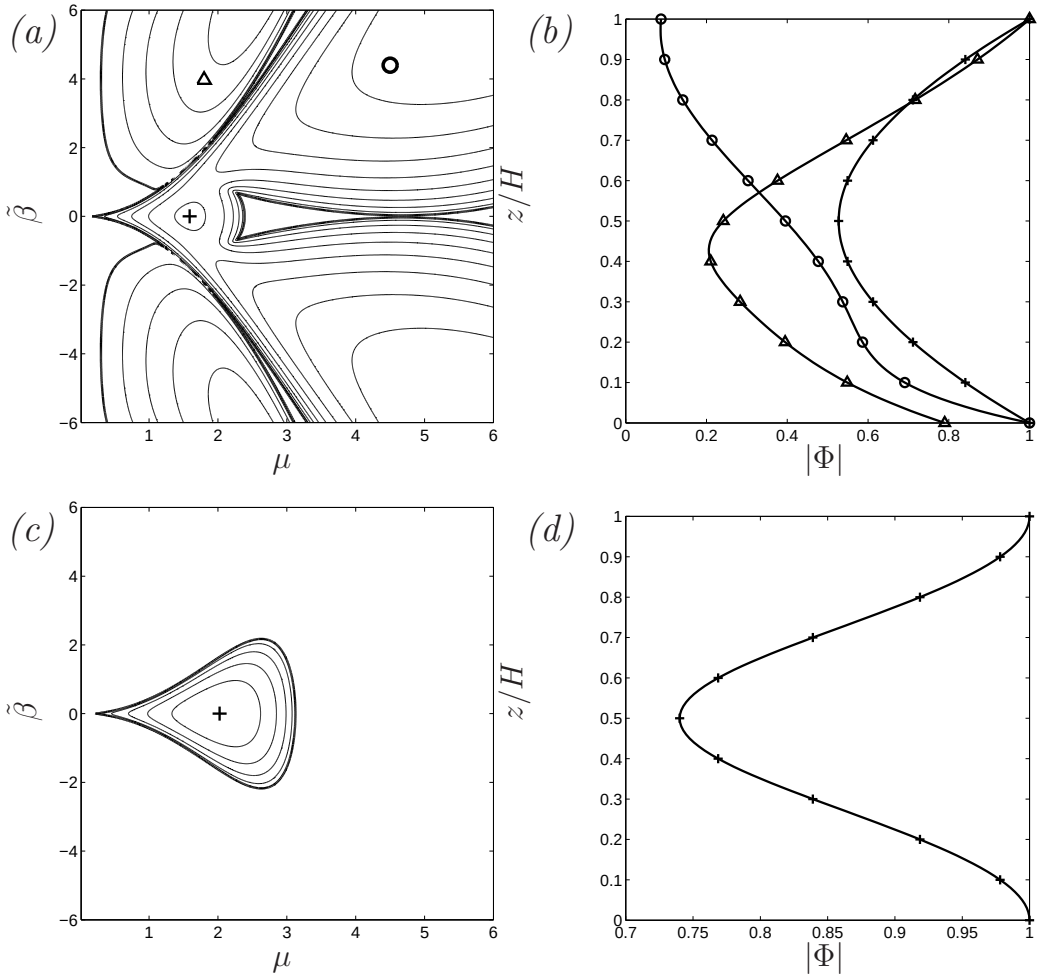

Figure 3.2: Growth rates versus nondimensional β and zonal wavenumber are plotted for (a) an Eady like instability (when $\beta = 0$) with only mean surface gradients and (c) a Phillips type instability with only mean interior gradients. Contour values are vary linearly from 0.05 (thick line) to 0.4 at 0.05 intervals. Note that growth rates have been nondimensionalized by U_0/L_d. (b) Amplitudes of particular eigenfunctions for the Eady instability and for (d) the Phillips instability.

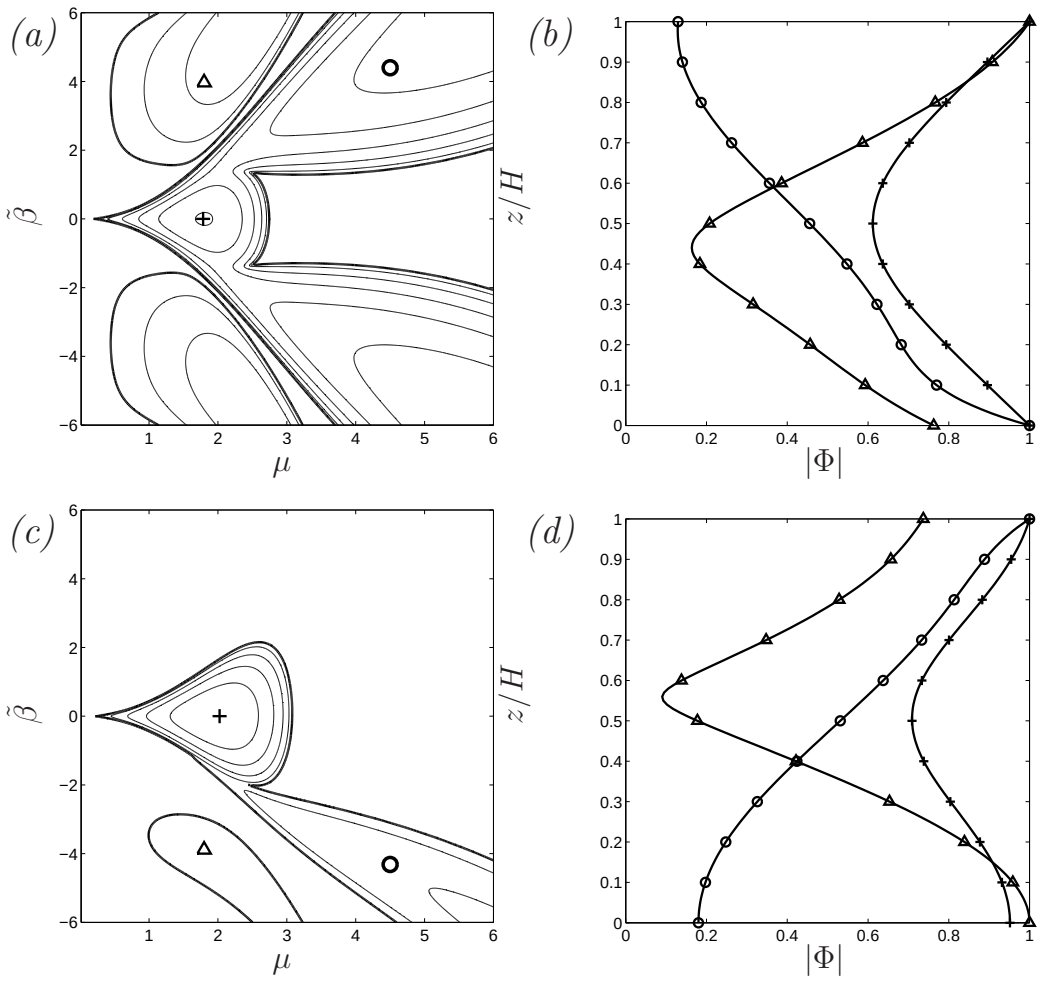

Figure 3.3: Growth rates and eigenfunctions as in Fig. 3.2 but for mixed surface and interior mean gradients. (a) Equal surface and interior mean gradients. (c) Linear instabilities for the parameters used in the nonlinear simulations in section 3.3.

The plus symbol, for example, corresponds to the location of maximum growth in the Eady problem ($\tilde{\beta} = 0$), and has the expected symmetric amplitude, peaked at the boundaries ($\cosh \mu z/H - (U_0/\mu c) \sinh \mu z/H$). The triangle is located in the Green-mode region, and has a vertical structure that is comparable to Figure 6 of Green (1960). The circle is in the bottom Charney-mode region and its vertical structure is, likewise, comparable to that expected for the Charney problem (see, e.g. Pedlosky, 1987, figure 7.8.5).

Figure 3.2c shows the growth rates for the pure interior shear problem, with $\Theta_y^T = \Theta_y^B = 0$ and $U^{\rm bc}/U_0 = -1/(\sqrt{2}\pi)$ and Figure 3.2d shows its vertical structure. This is the standard two-mode Phillips problem with $\max(\omega_i) L_d/|U^{\rm bc}| = (\sqrt{2} - 1)\pi$, and so the chosen value of $U^{\rm bc}/U_0$ gives $\max(\omega_i) L_d/U_0 = 1 - 1/\sqrt{2} = 0.29$, which is close to the maximum growth rate for the Eady problem. As expected, there is no long-wave cutoff for $\beta = 0$; for large enough $\tilde{\beta}$, instability is suppressed; and the amplitude is peaked at the boundaries, but is large throughout the depth of the fluid. Figure 3.3a shows the growth rate for equally weighted surface and interior forcing $(H/U_0)\Theta_y^T = (H/U_0)\Theta_y^B = -1$ and $U^{\rm bc}/U_0 = -1/(\sqrt{2}\pi)$; comparison to Figure 3.2a shows that the effect of the interior shear in this case is primarily to suppress growth at small scales, for small values of $\tilde{\beta}$. The vertical structure of the amplitudes for the three apparent peaks are similar to those in figures 3.2a-b, except that the amplitude corresponding corresponding to the $\tilde{\beta} = 0$ instability is larger. Figure 3.3c shows the growth rate for a mean state with an upper-surface temperature gradient $(H/U_0)\Theta_y^T = -1/2$, a vanishing lower-surface temperature gradient, and an interior shear $U^{\rm bc}/U_0 = -4/(\sqrt{2}\pi)$, four times larger than the interior shear used in panel a. This mean state is used in the central nonlinear simulation discussed in the next section. Removing the bottom temperature

gradient has suppressed the large-scale Green modes, and left only type-(iii) (Charney) instabilities at small scales. The asymmetry at small scales occurs because the upper-surface temperature gradient and the interior PV gradient must be of the same sign (consider the PV gradient in Equation (3.7)).

3.3 Nonlinear simulations

Here we report on the results of a series of simulations made with the fully nonlinear TMTS model (3.8), using parameters relevant to the midlatitude atmosphere. In all cases, we set the dimensional parameters $U_0 = H = 1$, and $L = 2\pi$, so that wavenumber 1 fills the domain. In the primary series, the interior shear and bottom temperature gradient are held constant at $U^{\rm bc} = -4/(\sqrt{2}\pi)$ and $\Theta_y^B = 0$, respectively, but the upper-surface temperature gradient is varied from $\Theta_y^T = -1/4$ to -2. The model is pseudo-spectral, fully de-aliased, and is run at a maximum resolution equivalent to 2048^2 grid-points ($K_{\rm max} = 1027$). The model deformation wavenumber $K_{\rm D} = 1/L_{\rm D} = 2$, to allow a wide forward cascade. The Coriolis gradient is set to $\tilde{\beta} = \beta L_{\rm D}^2/U_0 = 1$ and the Ekman drag is $r/U_0 \approx 0.18$ (the drag is varied slightly with Θ_y^T in to keep the energy injection rate nearly constant among the runs). The baroclinic growth rates for the mean states in this series of simulations are all nearly the same as shown in Figure 3.3c (which corresponds to the case with $\Theta_y^T = -1/2$). A highly scale-selective exponential cutoff filter, as described in Appendix A.1 absorbs the forward cascade (it is explicitly restricted to act only on wavenumbers $K > 2K_{\rm max}/3$, but in fact only affects a much smaller range of wavenumbers close to $K_{\rm max}$).

Figure 3.4 shows snapshots of the PV and temperature at the upper surface for

the simulation with $\Theta_y^T = -1/2$. Panel (a) shows the entire PV field, (b) shows the entire temperature field, while panels (c) and (d) show finer pictures of the fields inside the dashed boxes of the upper panels. At large scales the PV and temperature are anti-correlated and dominated by the PV, while at small scales the surface dynamics are revealed: small-scale vortices (due to secondary roll-up of filaments, Held et al., 1995) are wide-spread in the temperature field, and appear to actively stir the PV. The anti-correlation between PV and temperature is consistent with Lapeyre and Klein (2006), who show that if the forcing of interior PV and surface temperature are the same, then the anomalies will be strongly correlated or anti-correlated, depending on Q_y and Θ_y, even if they are not advected by exactly the same flow.

Figure 3.5 shows the total kinetic energy spectrum (for the same run with $\Theta_y^T = -1/2$), after equilibration and averaged over many eddy turnover times, at the top surface $E(K, z = H) = K^2|\hat{\psi}(H)|^2$ as well as the components that contribute to the total kinetic energy, plotted against horizontal wavenumber. The dash-dot line is the barotropic kinetic energy $K^2|\hat{\psi}^{\rm bt}|^2$, which is driven primarily by the interior shear $U^{\rm bc}$ and has a steep K^{-3} slope as a result of enstrophy cascading to small scales. The dashed line is the spectrum of the available potential energy (APE) at the upper surface, which is equal to the kinetic energy of the surface streamfunction $K^2|\hat{\psi}^{\rm t}|^2$ because the small scales are dominated by SQG dynamics at the surface (see, e.g., Gkioulekas and Tung, 2007a, for a derivation of equipartition between KE and APE in SQG turbulence) and cascades forward with a shallow $K^{-5/3}$ slope, which is proven rigorously for SQG turbulence by Gkioulekas and Tung (2007b). The solid line is the total kinetic energy spectrum at the upper surface, which is apparently a superposition of the barotropic and

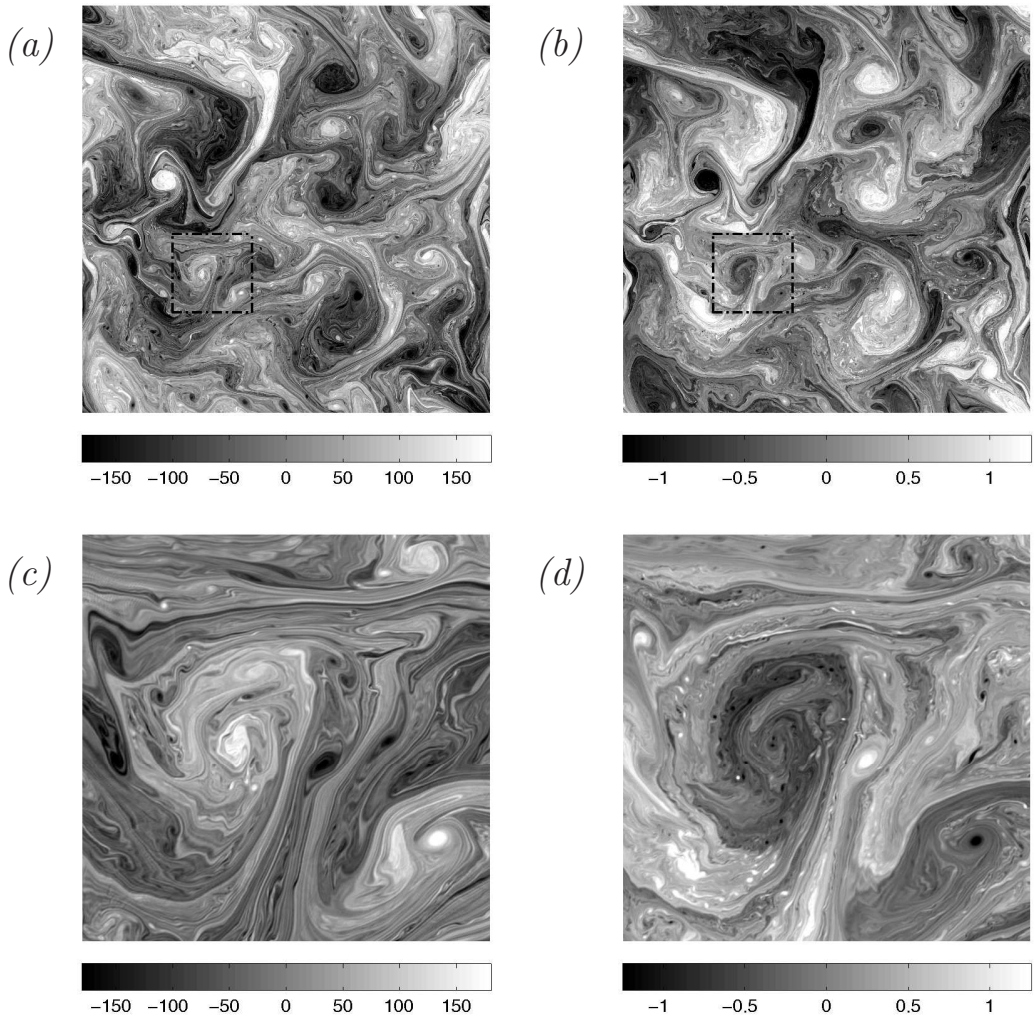

Figure 3.4: Snapshots of PV and temperature at the top surface for the $\Theta_y^T = -.5$ case. At large scales (a) $q(H)$ and (b) θ^T are anti-correlated and driven by the PV dynamics. At small scales (c) $q(H)$ is dominated by the dynamics of vortices present in (d) θ^T.

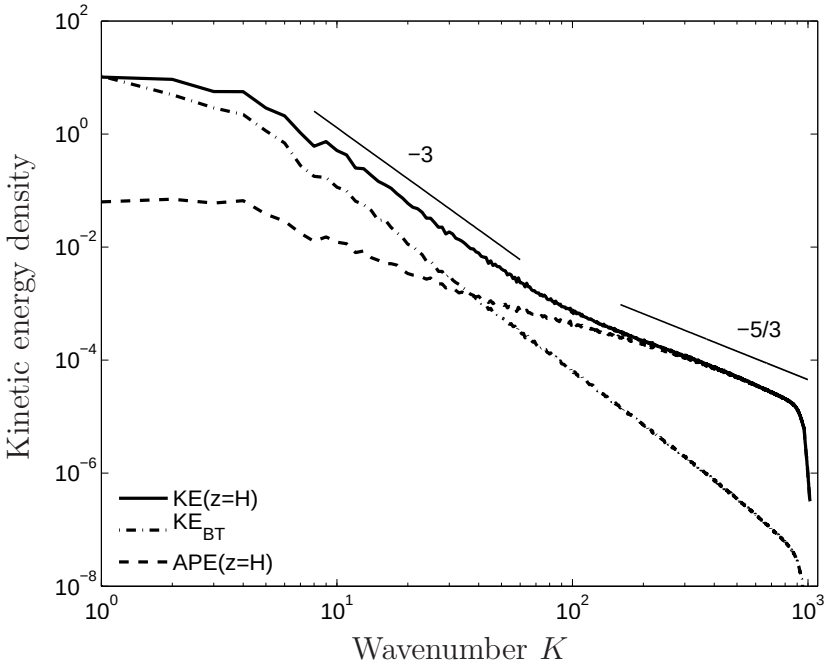

Figure 3.5: Energy densities as a function of horizontal wavenumber for the $\Theta_y^T = -.5$ simulation. The kinetic energy density at the top surface (thick solid) exhibits a transition from -3 where barotropic kinetic energy (dash-dot) dominates to $-5/3$ at $k \approx 100$ as the variance of temperature (long dashed) begins to dominate the forward cascade.

surface-induced spectra (with some influence from the baroclinic kinetic energy at large scales), perhaps as expected from the PV and temperature fields in Figure 3.4. There is a transition from K^{-3} interior-dominated dynamics to $K^{-5/3}$ surface-dominated dynamics at a wavenumber dependent on the relative energy levels in the surface and interior modes, which in turn depend on the relative strengths of the surface and interior baroclinic forcing. We also note that, because the interior dynamics in the numerical model are truncated at only the first baroclinic mode, the interior APE is concentrated at $z = H/2$, and so the simulated APE lacks a K^{-3} slope at large scales at or near the upper surface.

3.3.1 Transition scale dependence on the surface and interior gradients

Figure 3.6 shows the upper-surface kinetic energy spectra for each of the series of simulations in which Θ_y^T is varied from $-1/4$ to -2. It is apparent that the

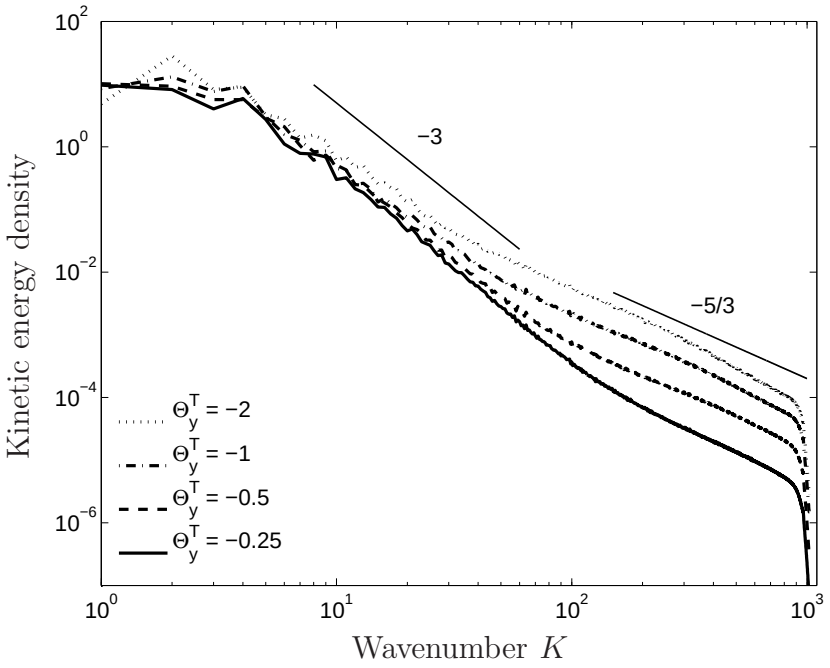

Figure 3.6: Kinetic energy spectra at $z = H$ with $\Theta_y^T = -2, -1, -0.5$, and -0.25, $U^{\rm bc} = -4/(\pi\sqrt{2})$ and $H = 1$ at 2048^2 resolution. Thin lines are $K^{-5/3}$ and K^{-3} for reference. The small scale spectra are approximately $11K^{-5/3}$, $5K^{-5/3}$, $1.5K^{-5/3}$, and $0.45K^{-5/3}$.

transition scale between the steep large-scale spectrum and the shallow small-scale spectrum is controlled by Θ_y^T. The particular dependence of the transition scale on the parameters of the problem can be understood as follows. The upper-level

energy spectrum in the forward enstrophy cascade has the form

$$\mathcal{E}(K) = \mathcal{C}_E \eta^{2/3} K^{-3},$$

where the rate of enstrophy transfer at $z = H$ is

$$\eta = -Q_y(H)\ \overline{vq}|_{z=H} \equiv \kappa_q Q_y(H)^2.$$

The overbar denotes a horizontal average, $\mathcal{C}_E$ is a Kolmogorov constant, and we have defined a PV diffusivity κ_q. The cascade of temperature variance at the upper surface leads to an available potential energy spectrum of the form

$$\mathcal{A}(K) = \mathcal{C}_A \epsilon^{2/3} K^{-5/3}$$

where the relevant energy flux is

$$\epsilon = -\frac{f^2 \Theta_y^T}{N^2}\ \overline{v\theta^T}|_{z=H} \equiv \kappa_\theta \left(\frac{f\Theta_y^T}{N} \right)^2.$$

Here we have defined a second diffusivity κ_θ for the temperature, and a second Kolmogorov constant for the temperature cascade.

Assuming equal diffusivities $\kappa_q \simeq \kappa_\theta$ and Kolmogorov constants $\mathcal{C}_E \simeq \mathcal{C}_A$, and solving for the wavenumber where the two cascades are equal, one finds the upper-level transition wavenumber

$$K_{\text{trans}} \simeq \frac{N}{f} \left| \frac{Q_y(H)}{\Theta_y^T} \right|. \tag{3.9}$$

It is instructive to rewrite this expression as

$$K_{\text{trans}} \simeq \left| L_{\text{C}}^{-1} + L_{\text{D}}^{-1} \frac{U_z(0) - U_z(H) - \sqrt{2}\pi^2 U^{\text{bc}}/H}{|U_z(H)|} \right|, \tag{3.10}$$

where (1.4), (1.6) and (3.7) were used to replace the PV and temperature gradients with shears and

$$L_{\text{C}} = \frac{f}{N} \frac{|U_z(H)|}{\beta}$$

is the Charney length (see, e.g. Pedlosky, 1987). The second expression for K_{trans} now has a form similar to that of the transition wavenumber found by Tulloch and Smith (2006), $L_{\text{D}}^{-1} = f/NH$, except that here (pulling out a factor f/N) there are two vertical scales, added in reciprocal: the Charney depth ($h_{\text{C}} = fL_{\text{C}}/N$) and a second term corresponding to the fluid depth H times the relative ratio of surface to total shears. In the limit of no interior or bottom shear, and assuming $h_{\text{C}} \ll H$, the vertical scale is just the Charney depth, and $K_{\text{trans}} \simeq L_{\text{C}}^{-1}$. In the limit of $\beta = 0$, the transition scales with the inverse deformation scale, and if additionally $U_z(H) \gg U^{\text{bc}}/H$, then the vertical scale is H ($K_{\text{trans}} \simeq L_{\text{D}}^{-1}$), as found in the simpler model of Tulloch and Smith (2006).

The scaling prediction (3.10) is tested against the "measured" transition wavenumbers for all simulations performed (including a third series identical to the second series, except the bottom temperature gradient is held fixed at $\Theta_y^B = 5$) in Figure 3.7 (see caption for details of the transition scale computation). The theory apparently captures the variation of transition scale with surface shear quite well. There is a bias towards under-predicting the measured transition wavenumber when K_{trans} is small, which is perhaps due to halting scale (or drag) effects in the numerical model, which are not accounted for in the theory. We also check here

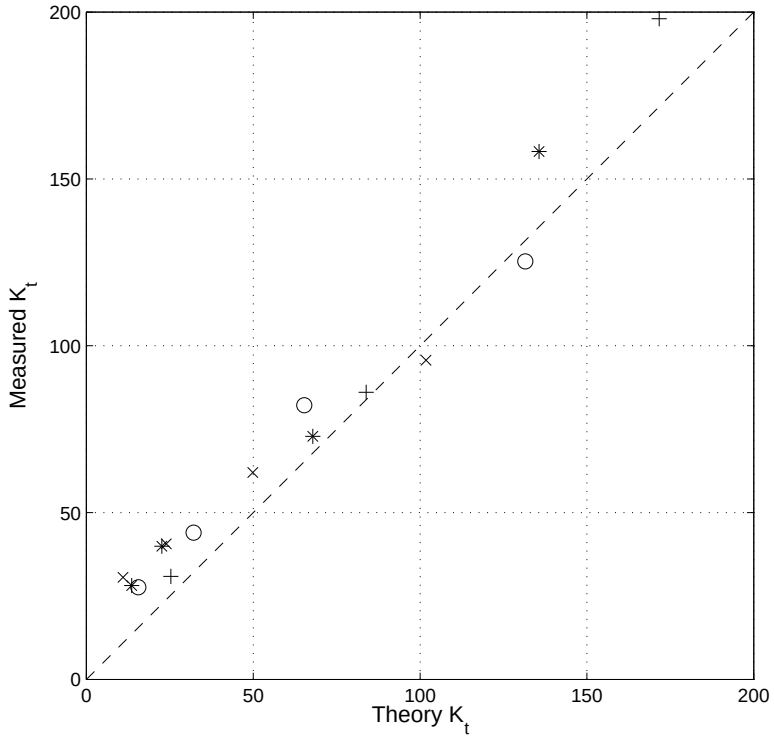

Figure 3.7: The measured transition wavenumber for all simulations, defined as where the slope is $k^{-7/3}$, compared with the prediction from (3.10). We set $L = 2\pi$, $U_0 = H = 1$ for all runs. Asterisks: $\Theta_y^T = \Theta_y^B = \{-5, -3, -1, -.5\}$, $U^{\rm bc} = -1$, $\tilde{\beta} = 3$, $K_{\rm D} = 4$; Pluses: same as asterisks but $\Theta_y^T = -5$ for each; Circles: $\Theta_y^T = \{-2, -1, -.5, -.25\}$, $\Theta_y^B = 0$, $U^{\rm bc} = -4/(\sqrt{2}\pi)$, $\tilde{\beta} = 1$, $K_{\rm D} = 2$; X's: $\Theta_y^T = \{-2, -1, -.5, -.25\}$, $\Theta_y^B = 0$, $U^{\rm bc} = -.7$, $\tilde{\beta} = 3$, $K_{\rm D} = 2$.

that the results are independent of horizontal resolution. Figure 3.8 shows the resulting surface energy spectra for a series of simulations in which all parameters are held constant ($\Theta_y^T = -0.5$), but horizontal resolution is successively reduced. The

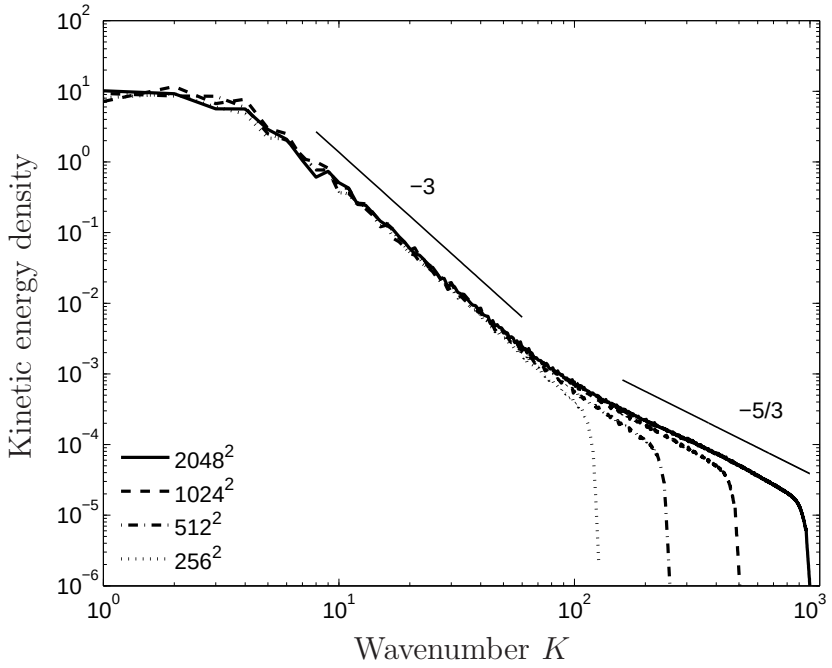

Figure 3.8: Kinetic energy spectra at $z = H$ with $\Theta_y^T = -.5$ and $K_\mathrm{D} = f\mathcal{L}/NH = 2$, computed at different horizontal resolutions.

results confirm that the transition from K^{-3} to $K^{-5/3}$ is independent of numerical resolution, as well as small scale filtering.

We can check that the surface energy exhibits an inertial range cascade by computing the energy flux directly, as a function of wavenumber. For the series of simulations in which the upper-surface temperature gradient is varied, the surface

fluxes of available potential energy,

$$\epsilon(K) = \frac{f^2}{N^2} \int_0^K \hat{\theta}^T \hat{J}(\hat{\psi}, \hat{\theta}^T)\, dK',$$

are shown in Figure 3.9. The fluxes are constant, as suggested.

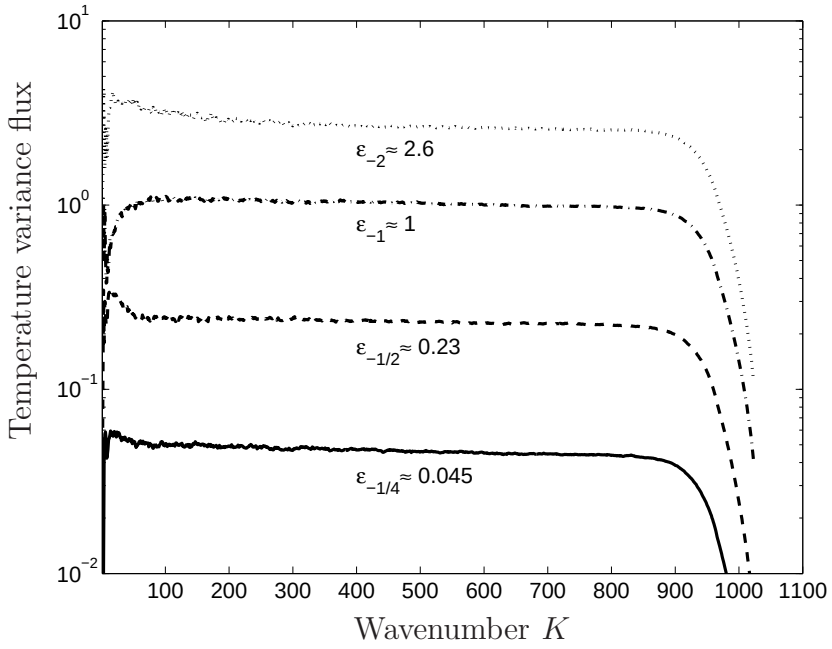

Figure 3.9: Measured temperature variance fluxes for $\Theta_y^T = -2, -1, -0.5$, and -0.25 are $\epsilon \approx 2.6, 1, 0.23$, and 0.045 respectively. Approximate values of Kolmogorov's constant for these transfer fluxes are $C_T \approx 5.8, 5, 4, 3.6$ respectively, which are obtained from measuring the magnitude of the $K^{-5/3}$ part of the spectra in Figure 3.6.

3.3.2 Atmospheric parameters

Using long term monthly mean data from NCEP reanalysis simulations, a mean wind profile is computed by averaging data from 45°N temporally and zonally. The

meridional potential temperature gradients from the 1000 mb and 200 mb data (corresponding to $H \simeq 9.7$ km) are computed from zonal and temporal averages at the same latitude, from which the mean upper and lower level shears are inferred from thermal wind balance, and the profile U^S is then computed from the shears. The interior first baroclinic mean zonal wind is then approximately the difference between the NCEP data profile and the surface induced zonal wind. The resulting surface shears are $U_z(H) = 5.6 \times 10^{-4}$ s^{-1} and $U_z(0) = 2.1 \times 10^{-3}$ s^{-1}, and the interior baroclinic velocity is $U^{\rm bc} = -2.6$ m s^{-1}, corresponding to an interior shear $\sqrt{2}\pi^2 U^{\rm bc}/H = 3.7 \times 10^{-3}$ s^{-1}. Using a typical stratification $N = 10^{-2}$ s^{-1}, one finds $L_{\rm C} = 360$ km, $L_{\rm D} = NH/f = 950$ km, and so Eq. (3.10) gives $K_{\rm trans} \simeq 1/77$ km^{-1} (or transition wavelength $\simeq 480$km) as the transition wavenumber predicted by our scaling theory, which is quite near the observed atmospheric transition wavelength of about 450 km.

These values are used in a simulation, the results of which are shown in Figure 3.10. Panel (a) shows the spectra of kinetic energy at the upper surface, the available potential energy, and the barotropic kinetic energy. The structure is similar to the spectra in Figure 3.5. The bottom axis is the dimensional wave*length*, for comparison with the Nastrom-Gage spectrum presented in Figure 3.1. The transition wavelength in the simulation is near 300 km, somewhat smaller than that predicted above (and smaller than the observed transition wavelength), but is consistent with the bias of under-predicting the transition wavenumber when $K_{\rm trans}$ is small, as shown in Figure 3.7 and discussed above. Note that we have made coarse approximations in choosing our atmospheric parameters by averaging zonally at a particular latitude and pressure level, so it is not surprising that there is a discrepancy. The overall energy level of our simulation is higher than

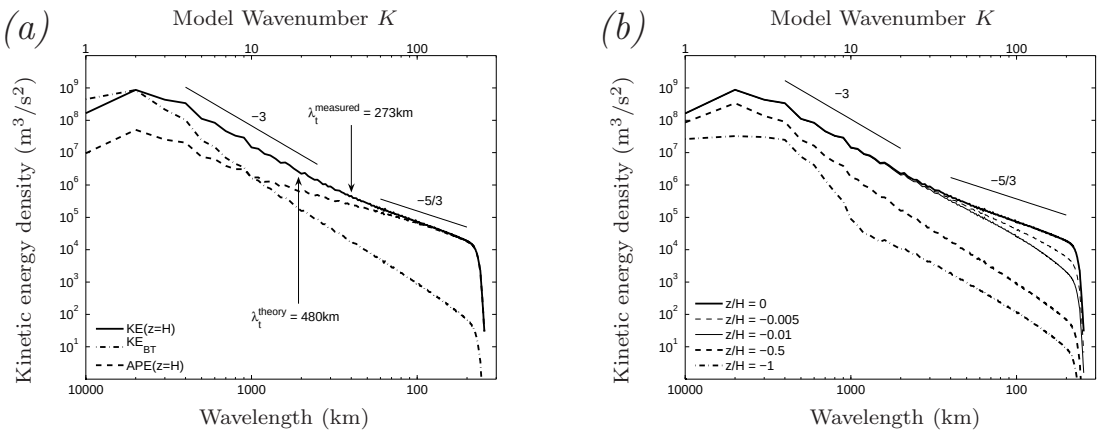

Figure 3.10: (a) The spectra using zonally and temporally averaged winds from NCEP at 45°N. Shown are the kinetic energy at the top surface (solid), the barotropic kinetic energy (dash-dot), and the variance of potential temperature at the top surface (dashed). (b) Kinetic energy spectra at different height values for the same run.

the observed level, and the temperature variance is less. However, it should be restated that this is an idealized, doubly-periodic model, designed to represent one aspect of the turbulent structure of the synoptic- and meso-scales. The large-scale forcing and dissipation are crudely represented, and the interior flow is truncated to include only two vertical modes.

Cho and Lindborg (2001) found the spectral energy flux in the MOZAIC data to be $\epsilon = 6\times10^{-5}$ m^2 s^{-3} just above the tropopause, while Dewan (1997) notes that observed stratospheric energy fluxes range from 1×10^{-6} to greater than 1×10^{-4} m^2 s^{-3}. For comparison, we compute the flux from this atmospheric-parameter run and find the spectral flux of available potential energy at the surface to be $\epsilon = 8 \times 10^{-5}$ m^2 s^{-3} which is within the observed range.

Lastly, note that the surface energy is expected to decay away from the surface, over a depth scale proportional to KN/f, for $K > K_{\text{trans}}$. Below this scale depth, the interior spectrum should be dominated by the K^{-3} slope interior dy-

namics. Figure 3.10b shows plots of the spectra at various heights at and below the upper surface. The structure is remarkably similar to that found by Hamilton et al. (2008) (see also Takahashi et al., 2006) in very high-resolution global circulation simulations, however it stands in contrast with the simulations of Skamarock (2004)and Skamarock and Klemp (2008). The source of the discrepancies between those sets of simulations are not clear at present.

3.4 Conclusions

We have demonstrated that a balanced model that properly represents surface buoyancy dynamics will produce a robust forward cascade along its boundaries, with a spectrum that exhibits a shallowing from K^{-3} to $K^{-5/3}$ slope, consistent with the observed atmospheric kinetic energy spectrum. The TMTS model consists of four streamfunction modes: the barotropic and baroclinic interior modes due to potential vorticity in the interior and top and bottom surface modes due to potential temperature on the boundaries. The full streamfunction is a superposition of these modes because the associated inversion problems are linear. Depending on what baroclinic forcing is applied all three of the classical baroclinic instability types (Charney, Eady, and Phillips) can be excited. The transition scale in this model is set by the ratio between the horizontal temperature gradients at the upper and lower boundaries and the internal shear since these are the drivers of energy generation for the boundary and interior spectral cascades. Using midlatitude atmospheric parameters and mean gradients (at least as well as such can be represented in this truncated model) produces a transition scale near the observed scale.

The forward energy cascade near the vertical boundaries has implications in both the atmosphere and ocean. In the atmosphere, as we have shown here, the surface modes may be responsible for the transition from steep to shallow slope in the kinetic energy cascade. In the ocean where stratification and shear are surface intensified, the surface modes likely have a more significant impact on the full flow.

The proposed model is still incomplete. In particular it produces insufficient potential energy near the surface at large-scales — the GASP data shows potential and kinetic energy with nearly identical spectra at large and small scales, whereas the truncated model produces a weak APE spectrum at large scales. This is likely the result of our severe truncation of vertical modes. Observations of the atmospheric energy spectra at mid-tropospheric depths are sparse, but those that do exist show a spectral slope of kinetic energy a little steeper than K^{-2} (Gao and Meriwether, 1998). The model proposed here, by contrast, produces an interior (mid-depth) spectrum with a slope with a minimum approaching K^{-3}. The model is also free of divergent modes, which may play a role in the energy spectrum at some scale, although observations suggest that vorticity dominates divergence at least down to 100km (Lindborg, 2007).

Simple extensions to the model could yield more accurate results. For example, we assumed an infinite jump in stratification at the tropopause with no motion in the stratosphere. A model with a finite stratification jump at the tropopause and a free stratosphere could be derived following Juckes (1994).

Chapter 4

Surface-modal model applied to the ocean: transition scale and baroclinic instability

In Chapter 3, the SMQG formulation was truncated and applied to the atmospheric energy spectrum. Here the full SMQG formulation will be applied to oceanic stratification in order to determine whether the ocean's surface dynamics are dominated by interior QG dynamics or surface QG dynamics.

The stratification in much of the world ocean consists of a shallow, unstratified (or weakly stratified) surface mixed layer above a highly stratified thermocline, which is above a deep, weakly stratified abyss. The dynamics of the mixed layer occur on the sub-mesoscales, so they are therefore smaller than what is considered here and beyond the scope of quasi-geostrophic models (see *e.g.,* Fox-Kemper et al., 2008, for a treatment of mixed layer dynamics). The presence of surface intensified stratification in the ocean, *i.e.,* the thermocline, has implications on

the vertical structure of the flow that develops. In particular, Stammer (1997) noted that spatial autocorrelation of SSH is proportional to the deformation radius. Also, Wunsch (1997) looked at the vertical partition of kinetic energy from current meters and argued that the surface kinetic energy is dominated by the first baroclinic mode. Analysis by Fu and Flierl (1980) and simulations of freely evolving QG turbulence by Smith and Vallis (2001) also indicate that, when there is surface intensified stratification, energy accumulates in the first baroclinic mode as energy cascades upscale from high horizontal wavenumbers and high vertical modes.

Based on the above findings, the ocean surface mesoscales are typically thought to be dominated by the first baroclinic mode. Scott and Wang (2005) observed an inverse cascade in the surface KE spectral flux, which had previously been thought of as being indicative of barotropic turbulence. Scott and Arbic (2007) later realized that, at larger scales than the deformation scale, as long as the total spectral flux (KE+APE) in the first baroclinic mode is positive then the KE spectral flux can be negative. However, such spectral flux directions are also consistent with SQG fluxes (Capet et al., 2008). In addition studies using GCM simulations (Klein et al., 2008), observations of SSH spectra (Le Traon et al., 2008), and analysis (Lapeyre and Klein, 2006; Lapeyre, 2008) argue that the surface mesoscales are dominated by the surface QG mode in many locations of the ocean. The simulations of Klein et al. (2008) show equal KE and APE spectra with shallow $K^{-5/3}$ spectral slopes at deformation scales near the surface and spectral fluxes that are consistent with SQG dynamics (Capet et al., 2008). Lapeyre (2008) decomposes the simulation of Klein et al. (2008) into surface and interior modes using a method analogous to our surface-modal decomposition in Section 2.2 and

finds that the SQG mode dominates the first baroclinic mode in most of the active regions of the Atlantic.

In this chapter we seek to address the question of which modes dominate the ocean's surface. In Section 4.1 the interactions between surface and interior modes in the SMQG model with surface intensified stratification are investigated using freely decaying turbulence simulations. In Section 4.2, we verify our scaling for the horizontal wavenumber of transition between interior dominated and surface dominated dynamics, Equation (3.9), for nonuniform stratification. Finally, in Section 4.3 the transition scaling is applied to the ocean atlas of Forget (2008) to diagnose our transition scale K_t for the world ocean.

4.1 Freely decaying energy cycle

Smith and Vallis (2001) verified the work of Fu and Flierl (1980) which argued that, for surface intensified stratification, energy in high baroclinic modes or horizontal wavenumbers should transfer to the first baroclinic mode, and deformation scale horizontal wavenumbers, before decaying to the barotropic mode. In this section we seek to extend Section 5 of Smith and Vallis (2001), which only looked at the energy cycle of interior QG modes, using the SMQG model to simulate the interaction between surface and interior modes.

We will consider two initial energy configurations:

1. the surface mode energized at larger than deformation scales with negligible interior energy in the third baroclinic mode (BC3),

2. the surface mode and BC3 similarly energized at the third deformation scale λ_3.

In each case, the energized modes are initialized with a Gaussian ring of energy in Fourier space, with radius K_0 and random phase. The simulations each contain 4 interior modes, 256^2 horizontal resolution, and the stratification has an exponential form

$$N^2(z) = \frac{\exp(z/\delta_c)}{\delta_c F}, \tag{4.1}$$

where $z \in [-1, 0]$, $\delta_c = 1/20$ and $F = 15$, which gives nondimensional deformation wavenumbers $\lambda_{1,2,3} = 22, 48, 75$. The Coriolis gradient is $\beta = 25$ in both cases, so that they may be compared with Simulation I (Figure 8) in Smith and Vallis (2001).

Figure 4.1 shows time slices of the kinetic energy spectrum $\mathcal{KE}(K, M)$ contoured against horizontal wavenumber (abscissa) and vertical mode number (ordinate), where M is the mode. The large scale initial energy is centered at around nondimensional wavenumber $K_0 = 5$ and the contours values are $4^\alpha \times 10^{-5}$, for $\alpha = \{1, 2, 3, 4, 5, 6i\}$ (in all plots). The format of the plot is analogous to Figures 7 and 8 from Smith and Vallis (2001) but with the addition of the surface modes. Note that 'B' stands for the bottom surface mode (which contains no energy), 'T' stands for the top surface mode, and 'BT' is the interior barotropic mode. The large scale top surface energy initially spreads mostly downscale, but some energy is also transferred to the barotropic mode[1]. By $t = 2.22$, some energy is also transferred into the first baroclinic mode, which then spreads to the deformation scale ($\lambda_1 = 22$)

Figure 4.2 shows snapshots analogous to Figure 4.1 but with the initial energy at small horizontal scales, near λ_3, and split between the surface mode and BC3.

[1]Note that while the spectral flux of KE, as defined below in Equation (4.2), is negative in an SQG flow, there is a compensating energy transfer from APE into KE which drives the KE downscale, see Capet et al. (2008) for details.

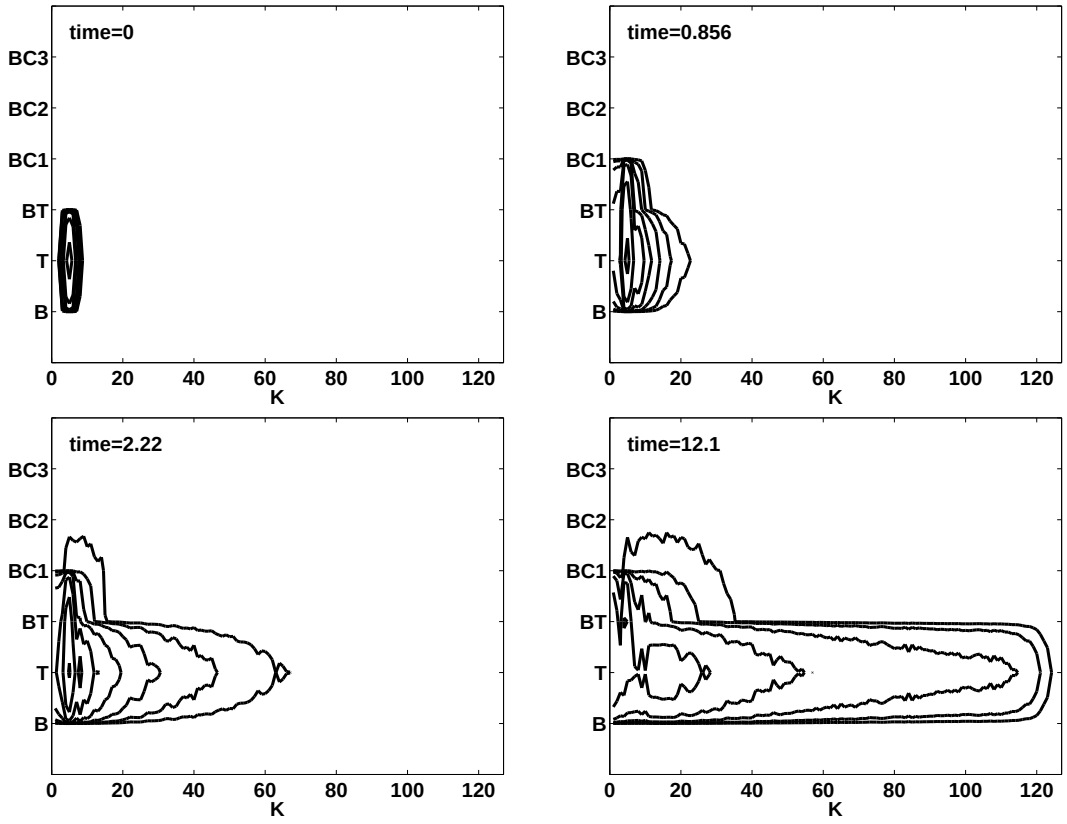

Figure 4.1: Evolution of freely decaying kinetic energy spectrum $\mathcal{KE}(K, M)$ as a function of horizontal wavenumber K (abscissa) and vertical mode M (ordinate) when most of the initial energy is in the surface mode at large scales. The

At time $t \approx 0.07$ the forward enstrophy cascade of the interior modes sends a small fraction of the energy in BC3 downscale, while the inverse energy cascade sends some energy upscale within BC3 and the rest is transferred to BC1 (with a small amount in BC2 and BT near the initial wavenumber). Most of the inverse cascade then proceeds within BC1. Meanwhile, the surface mode appears to be largely unaffected by the interior dynamics, the two finally merge at large scales in the BT mode. Note that transfers between the surface mode and higher baroclinic modes are difficult to diagnose in this simulation because there is little energy in the higher baroclinic modes.

A proposed schematic of the surface-interior interaction is shown in Figure 4.3, which is an adaptation of Figure 12 of Fu and Flierl (1980). Energy in interior modes tends to flow from from high horizontal and vertical wavenumbers towards low horizontal and vertical wavenumbers, with much of the inverse cascade at small scales occurring in the first baroclinic mode. The dashed lines show the surface-modal interactions. The surface modes primarily interact with the first baroclinic mode near the deformation scale. At small scales the surface-modal energy propagates downscale. On the other hand, at large scales, the surface modes act like, and interact with, the barotropic mode. In Section 2.4.1, we saw for uniform stratification, where $\lambda_j = j\pi f/NH$ for $j = \{1, 2, \ldots\}$, that the top surface mode "sees the bottom" for $K < K_t = f/NH$, and acts like infinite depth SQG for $K > f/NH$. In essence, the surface modes mimic the barotropic mode for $K < K_t$, the first baroclinic mode for $K_t < K < \lambda_1$, and the j^{th} baroclinic mode for $\lambda_{j-1} < K < \lambda_j$ for $j = \{2, 3, \ldots\}$. This is because for wavenumbers near λ_j, the j^{th} baroclinic mode has an inversion relation that is approximately linear,

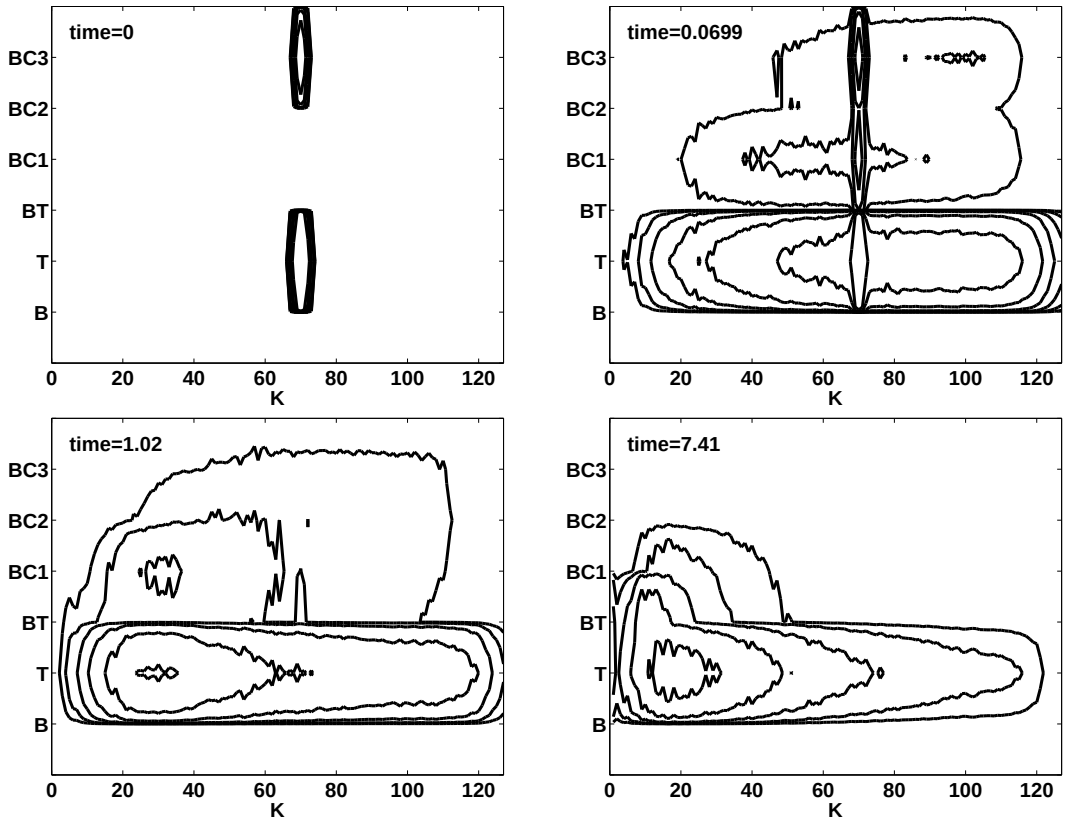

Figure 4.2: Evolution of freely decaying kinetic energy spectrum $\mathcal{KE}(K, M)$ as a function of horizontal wavenumber K (abscissa) and vertical mode M (ordinate) when initial energy is split between the surface mode and BC3 at small scales near λ_3.

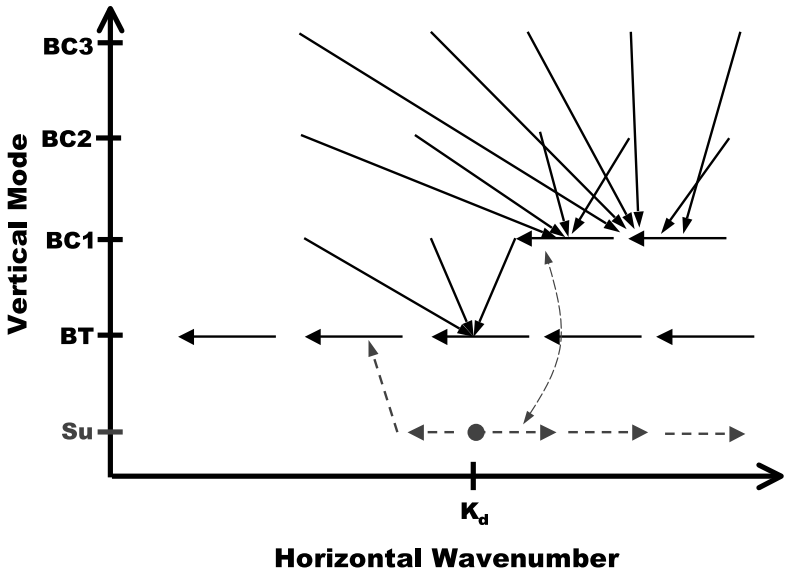

Figure 4.3: Most likely energetic transfer paths for exponential stratification as a function of interior and surface modes, and horizontal scale (adapted from Fu and Flierl, 1980). Solid lines show the interior interactions and dashed lines show the proposed surface and surface-interior interactions.

i.e.,

$$\hat{q}_j = -(K^2 + \lambda_j^2)\hat{\psi}_j \approx -2\lambda_j K\hat{\psi}_j \qquad \text{for} \qquad \mathrm{K} \approx \lambda_\mathrm{j},$$

so (ignoring interactions between modes) there is an SQG-like K^1 dependence between the advected scalar $\hat{q}_j$ and the streamfunction $\hat{\psi}_j$. But at wavenumbers above λ_j the the j^{th} baroclinic mode is dominated by its vorticity, *i.e.,*

$$\hat{q}_j \approx -K^2 \qquad \text{when} \qquad \mathrm{K} > \lambda_\mathrm{j},$$

so it acts like the barotropic mode with respect to energy cascades. Figure 4.4, described in the next section, illustrates how the vertical structure of the surface mode correlates with the vertical structure of the interior modes as a function of

wavenumber.

4.2 Forced-dissipative simulation

Here we consider a nonlinear simulation with baroclinic forcing and (ocean-like) exponential stratification in order to verify the transition wavenumber scaling in Equation (3.9), for non-uniform stratification. We choose exponential stratification of the form in Equation (4.1) for validation because it has analytical streamfunction inversion relations, so we can invert surface buoyancy exactly, without any numerical degradation due to vertical resolution. The streamfunction inversion relations contain Bessel functions, and are written explicitly in Appendix A.6. The simulation has 256^2 horizontal resolution, 4 interior modes, and parameters $\delta_c = 0.1$, $F = 1$, $\beta = 1.5$, drag $r = 0.1$.

Figure 4.4 shows the interior modes (left panel) and the upper surface mode $\phi^T(K, z)$ at wavenumbers $K = \{\lambda_1/10, \lambda_1, \lambda_2, \lambda_3\}$, where $\lambda_1 = 4$, $\lambda_2 = 9$, and $\lambda_3 = 14$. Near the surface, the surface modes at these wavenumbers decay at a similar rate as the baroclinic modes, but the surface modes monotonically decrease to zero.

The baroclinic forcing for the simulation is a zonal flow with exponential decay in the vertical $U(z) = \exp(z/\delta_U) - \delta_U$, where $\delta_U = 0.1$. To evaluate the dependence of the transition scale on the baroclinic forcing, we vary the temperature gradient at the top from $\Theta^T_y = -1$ to $\Theta^T_y = -6$. Figure 4.5 shows the contribution of U^S from Equation (2.10) to the total zonal velocity for each of these surface temperature gradients. The surface gradient contributes about half of the total zonal velocity when $\Theta^T_y = -6$. Note that in practice the SMQG model only sees

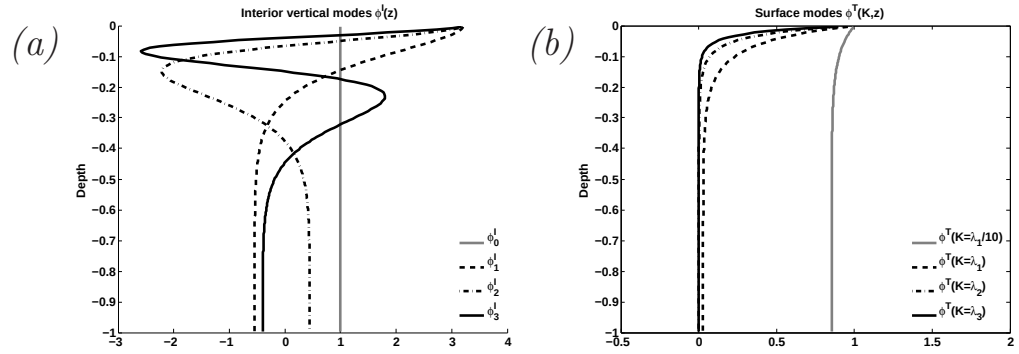

Figure 4.4: (a) Interior modes for forced dissipative simulation with exponential stratification (with $F = 1$ and $\delta_c = 0.1$). (b) Surface mode $\phi^T(K, z)$ at wavenumbers $K = \lambda_1/10$ (gray solid line), λ_1 (dashed line), λ_2 (dash-dotted line), and λ_3 (black solid line).

the projection of $U(z)$ onto the 4 interior modes and the surface modes, so the total zonal velocity is not exactly constant in each of the simulations.

Before considering the dependence on Θ_y^T we examine the energy spectra and fluxes for the case with $\Theta_y^T = -4$. The modal components of the kinetic energy spectra at the surface in the equilibrated flow are shown in Figure 4.6. In this configuration the first baroclinic (gray solid line) and surface mode (black dashed) dominate at the deformation scale, and the surface mode dominates the small scales. The barotropic mode (gray dashed line) is diminished, likely because the exponential stratification strongly inhibits vorticity at the bottom. This has the effect of reducing the slope of the K^{-3} portion of the total KE spectrum (black solid line).

Figure 4.7 shows the total KE and APE spectra at heights varying from the surface to mid-depth. In both the KE and APE spectra, the transition to $K^{-5/3}$ at small scales is limited to depths near the surface, consistent with finite depth SQG

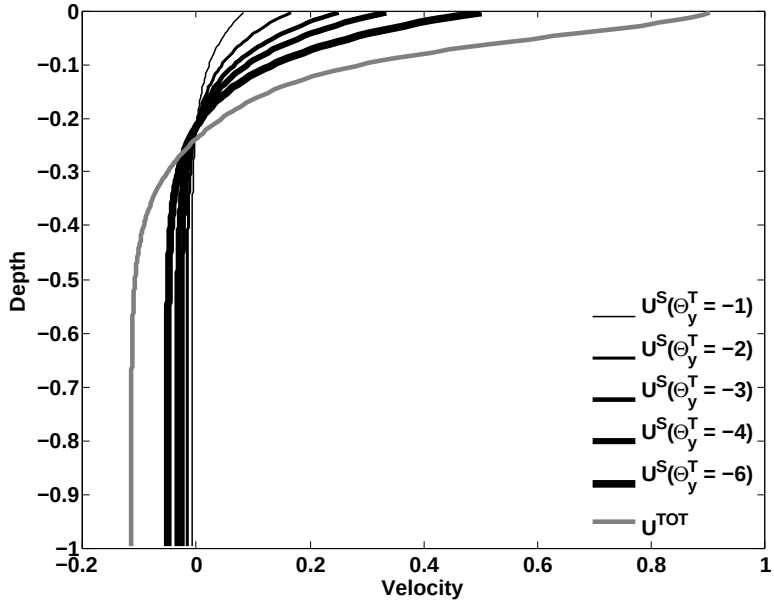

Figure 4.5: Total mean zonal velocity (gray line) and surface contributions U^S to the total. The surface temperature gradient Θ_y^T is increased from -1 to -6 (thin to thick black lines).

with uniform stratification. The surface APE is shallow at all scales because there are no interior contributions to the APE at the surface in SMQG. This explains why the surface value of APE (thick black line) is less than the values just below the surface.

Following the notation of Capet et al. (2008), the KE spectral flux at the surface is defined as

$$\Pi_u(K) = -\int_K^\infty \left\langle \Re\left[\hat{\mathbf{u}}^* \cdot (\widehat{\mathbf{u}\cdot\nabla\mathbf{u}})\right]\right\rangle dK', \tag{4.2}$$

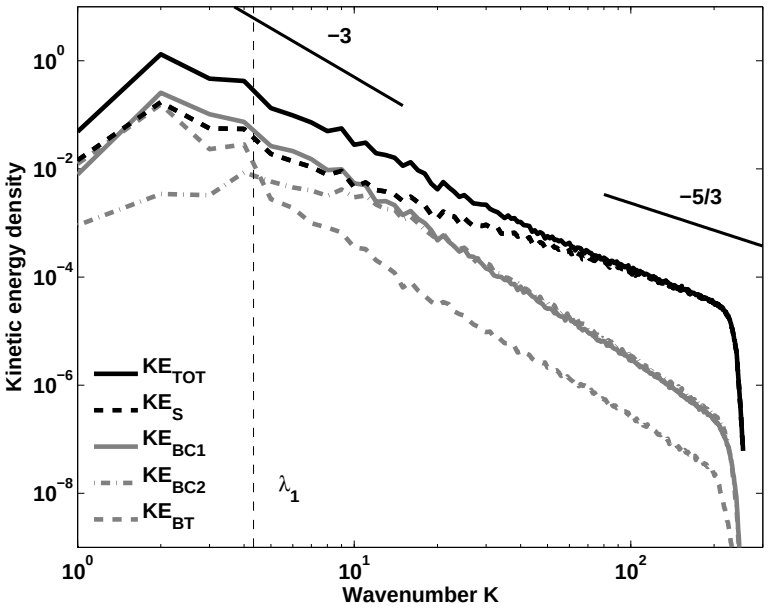

Figure 4.6: Kinetic energy spectra of the interior modes (gray lines), the surface mode (dashed black line) and the total KE at the surface (solid black line) with exponential stratification and $\Theta_y^T = -4$.

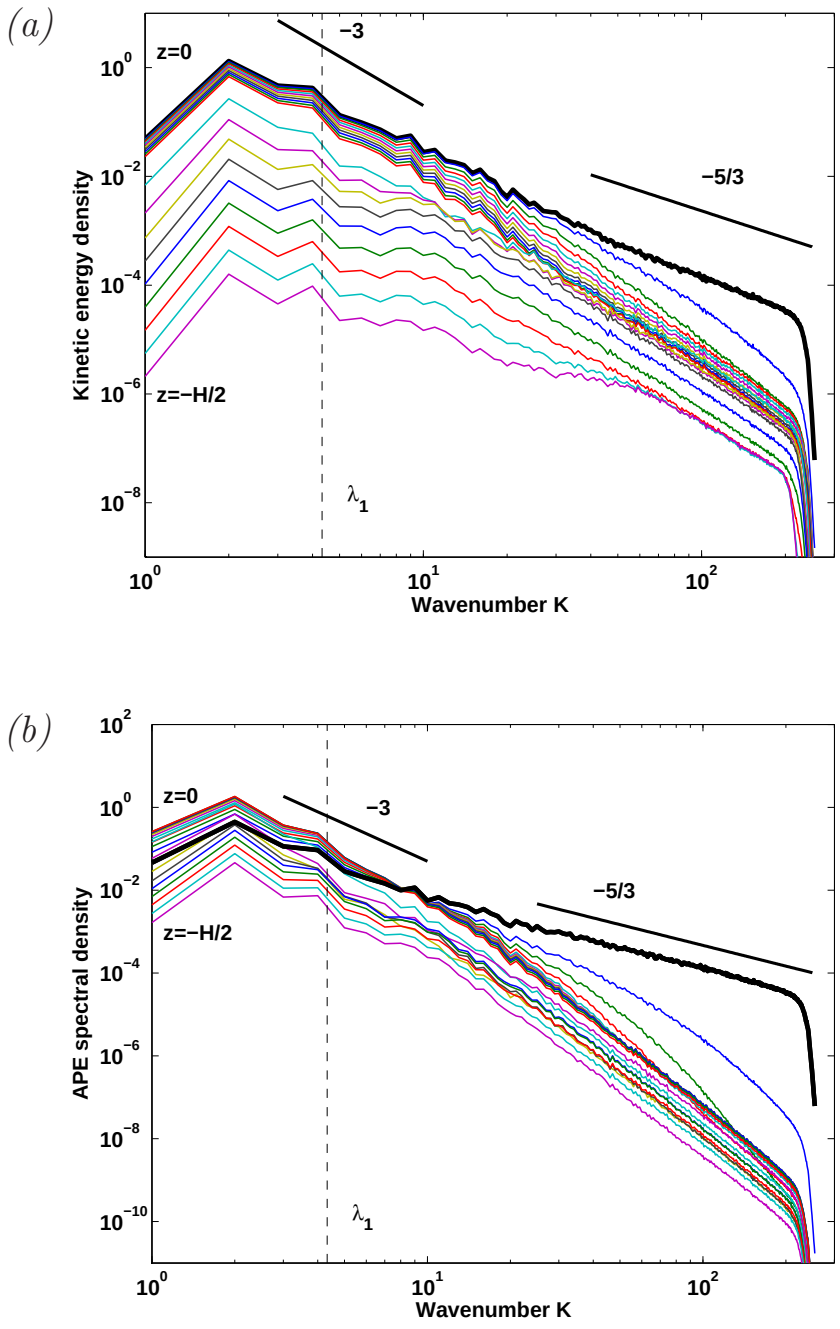

Figure 4.7: (a) Total Kinetic energy spectra at surface (thick black line) and at various depths below the surface: $z/H = -j/100$ for $j = \{1, 2, \ldots, 10\}$ and $z/H = -j/20$ for $j = \{2, 3, \ldots, 10\}$. (b) APE spectra at the same heights.

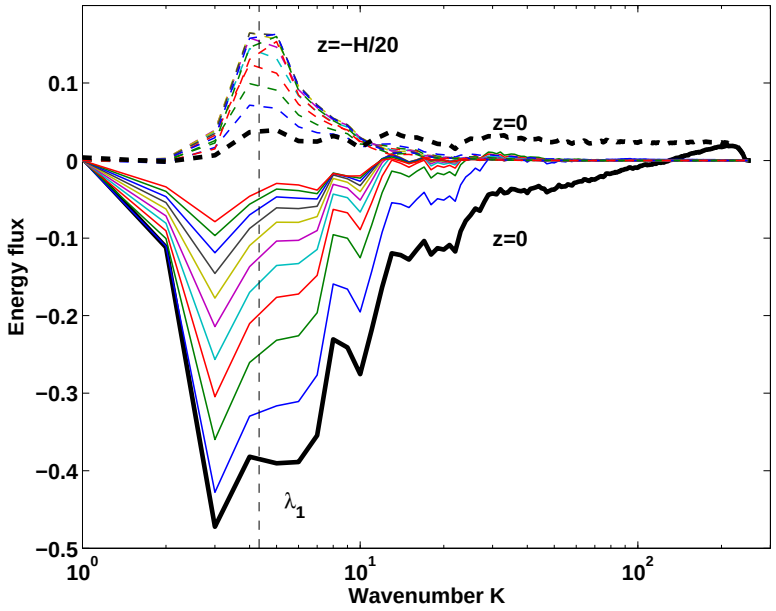

Figure 4.8: Spectral fluxes of KE (solid lines) and APE (dashed lines) at the surface (thick black lines) and at $z/H = -j/100$ for $j = \{1, 2, \ldots, 10\}$. The vertical dashed line indicates the deformation wavenumber.

and the APE spectral flux is defined as

$$\Pi_\theta(K) = -\int_K^\infty \left\langle \Re\left[\hat{\theta^T}^* \cdot \widehat{(\mathbf{u}\cdot\nabla\theta^T)}\right]\right\rangle dK'. \tag{4.3}$$

where $\langle\cdot\rangle$ denotes isotropic averaging and all velocities are evaluated at the surface. Figure 4.8 shows the KE and APE spectral fluxes at various depths near the surface. Both the inverse KE flux and direct APE flux are peaked near the first baroclinic wavenumber λ_1. Also, at large horizontal scales, the KE flux decays away from the surface while the APE flux grows away from the surface. The growth in APE flux away from the surface is likely due to interior APE. The surface APE flux begins to dominate near $K = 10$, which is also where the surface

APE dominates the spectrum in Figure 4.7(b).

4.2.1 Transition scale

In Section 3.3.1 we derived Equation (3.9) for the transition wavenumber given competing forward enstrophy (due to Q_y) and energy (due to Θ_y^T) cascades at the surface when the stratification is uniform. Here we test this scaling with highly non-uniform stratification, by refining Equation (3.9)

$$K_{\text{trans}} = \frac{N(z_T)}{f} \left| \frac{Q_y(H)}{U_z^T} \right|, \tag{4.4}$$

so that the surface stratification is taken into account.

Figure 4.9 shows the transition between K^{-3} scaling and $K^{-5/3}$ scaling as the temperature gradient is varied from $\Theta_y^T = -1$ to $\Theta_y^T = -6$, holding all other parameters constant. Although the exponential stratification suppresses the barotropic mode, the transition wavenumber scales as predicted. There is a bias towards larger than expected wavenumbers, however it does not appear to be wavenumber dependent. Since the deformation scale is close to the domain scale, the bias is probably related to domain or drag affects.

4.3 Applying the theory to ocean observations

Next we apply our transition wavenumber scaling to real ocean data. We use the ocean atlas of Forget (2008) which is essentially a mapping of Argo drifter data and satellite altimetric data using the MITgcm to interpolate onto a $1^\circ \times 1^\circ$ grid. While mixed layer dynamics are beyond the scope of the following QG calculations,

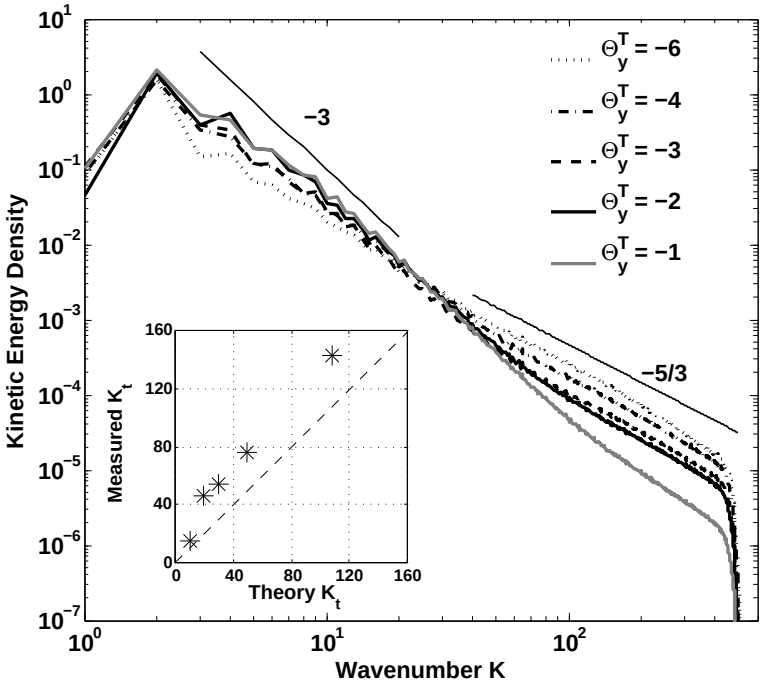

Figure 4.9: Transition wavenumber for various values of Θ_y^T.

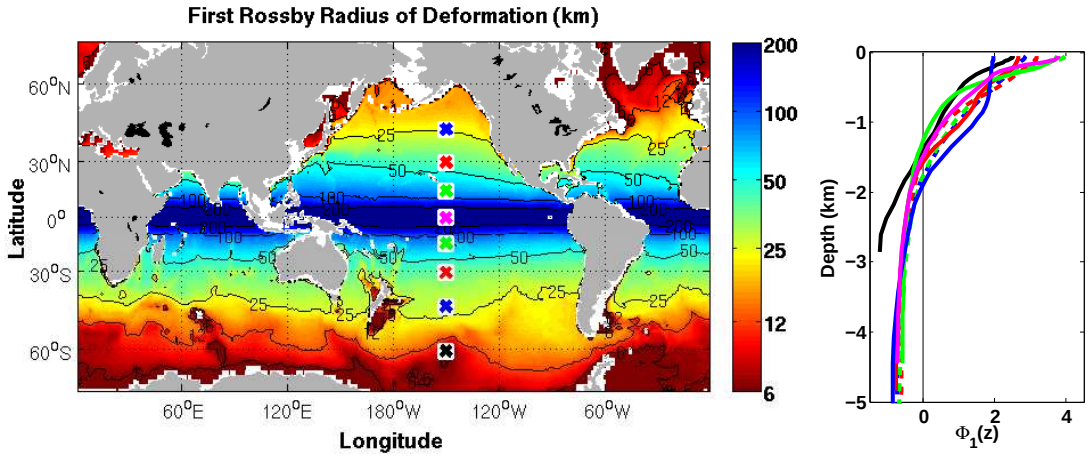

Figure 4.10: (Left panel) Map of first internal deformation *radius*, (right panel) vertical structure of the first baroclinic mode (right), $\Phi_1(z)$, at the positions marked with colored x's (at latitudes 60.5°S, 45.5°S, 30.5°S, 15.5°S, 0.5°S, 14.5°N, 29.5°N, and 44.5°N, and longitude 150°W). The lines are color-coded with dashed lines indicating the northern hemisphere and solid lines the southern hemisphere.

an upper boundary condition is required. We have opted to vertically average over the top 50m when computing the mean gradients in Equation (1.6). The rest of the mean ocean state is taken below $z_T = -50$m, similar to Stammer (1997). See Appendix A.7 for further details of the numerical discretization.

4.3.1 Linear calculations using an ocean atlas

Deformation scale

First, the density and stratification are computed using temperature and salinity. From the stratification, the deformation wavenumbers λ_m and baroclinic interior modes are computed by solving the Sturm-Liouville problem in Equation (2.7). A global map of the first deformation *radius* (λ_1^{-1}) is shown in Figure 4.10. The vertical structure of the first baroclinic normal mode is plotted on the right for

selected latitudes at 150°W in the Pacific Ocean, color-coded by the color of the x's and using solid (dashed) lines in the southern (northern) hemisphere respectively. The stratification tends to be more surface intensified at lower latitudes, where $\Phi_1(z = 0)$ tends toward values near 4, and less surface intensified at high latitudes, where $\Phi_1(z = 0)$ is between 2 and 3. Note that the colormap saturates near the equator as deformation radii tend towards infinity. Figure 4.10 may be compared with Figure 6 in Chelton et al. (1998) or Figure 1 in Smith (2007), which use different datasets but obtain very similar radii[2].

Observations of oceanic currents and QGPV gradients

Next the mean geostrophic currents and QGPV gradients are computed from the density using thermal wind balance. Figure 4.11 shows an example of zonally averaged (from 170°W to 120°W) mean geostrophic zonal velocity and the associated meridional QGPV gradient Q_y, with black contours marking zero. Note that the QGPV gradient is nondimensionalized by the value of the planetary vorticity gradient, β, at 30°, and that colors are saturated in the Q_y plot. The important point to note is that ∇Q is clearly not well approximated by β. The salient features of the Q_y plot include: (1) the zero crossing at 1 km depth in the ACC, just below the zonal jet which is responsible for significant baroclinically unstable growth and a steering level at depth, as reported in Smith and Marshall (2008), (2) the near surface zero crossings at low latitudes may contain baroclinic Charney instabilities, (3) the western boundary currents near 40°N (and the zero crossings below them), and (4) the convectively unstable regions in high latitudes where bottom water formation occurs.

[2]The deformation radius is approximately given by the vertical integral of the stratification(Chelton et al., 1998) so it is not particularly sensitive to dataset noise.

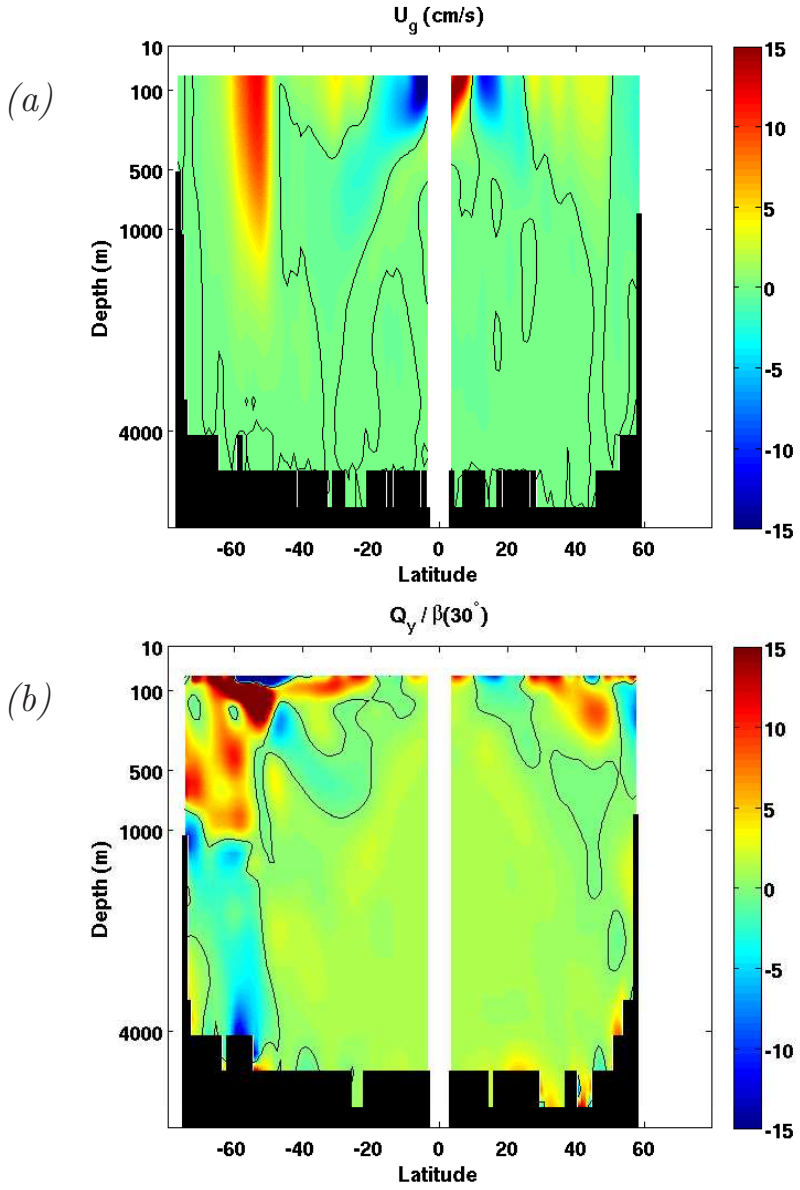

Figure 4.11: (Upper panel) Mean zonal velocity U, zonally averaged from 170°W to 120°W in the Pacific. (Lower panel) Meridional QGPV gradient zonally averaged over the same region. The PV gradient is normalized by the value of the planetary vorticity gradient, β, at 30 degrees. Note that the zero contour is indicated by black contours and that the color axis is saturated.

Baroclinic growth rates

To solve for the linear baroclinic growth rates, one first discards all quadratic advection terms, as in Equation (2.14a) but retaining meridional dependence and the QGPV gradients induced by the flow. Then one may either use a layered (or level) formulation as in Equation (2.1) (see also Appendix A.7 or Smith, 2007) which discretizes the QGPV using centered finite differences, or use the linearization of the surface-modal formulation in Appendix A.2. In both formulations a wave solution is assumed for the streamfunction, which results in a generalized eigenvalue problem, with the largest imaginary part of the eigenvalues being the growth rate. In the layered formulation the eigenvectors are "shear modes" which depend on z, while in the surface-modal formulation the eigenvectors give projections of the shear modes onto the interior and surface modes.

Figure 4.12 shows global maps, computed using the layered formulation, of the baroclinic growth rate. The upper panel shows the maximum growth rate, computed over a 100×50 grid in wavenumber space $(k, \ell) \in \{[-10\lambda_1, -0.1\lambda_1] \cup [0.1\lambda_1, 10\lambda_1]\} \times [0, 10\lambda_1]$ at each (lat,lon) position[3] The lower panel shows the maximum zonal growth rates, *i.e.,* when $\ell = 0$. Minimum time scales are $\sim$5 days in the major eddying regions: the ACC, Gulf Stream, and the Kuroshio (although the Kuroshio is a bit weaker). Outside of the major eddying regions the time scales on the order of 50 to 100 days. The decrease going from the upper plots to the lower plots gives an indication of the importance of nonzonal flow. Some high latitude regions have exceptionally high growth rates because they are bottom water forming regions with very low stratification at depth. The area below the jet in the ACC in Figure 4.11 is a good example of this.

[3]The lower half plane in (k, ℓ)–space is symmetric since the dynamic variables are real.

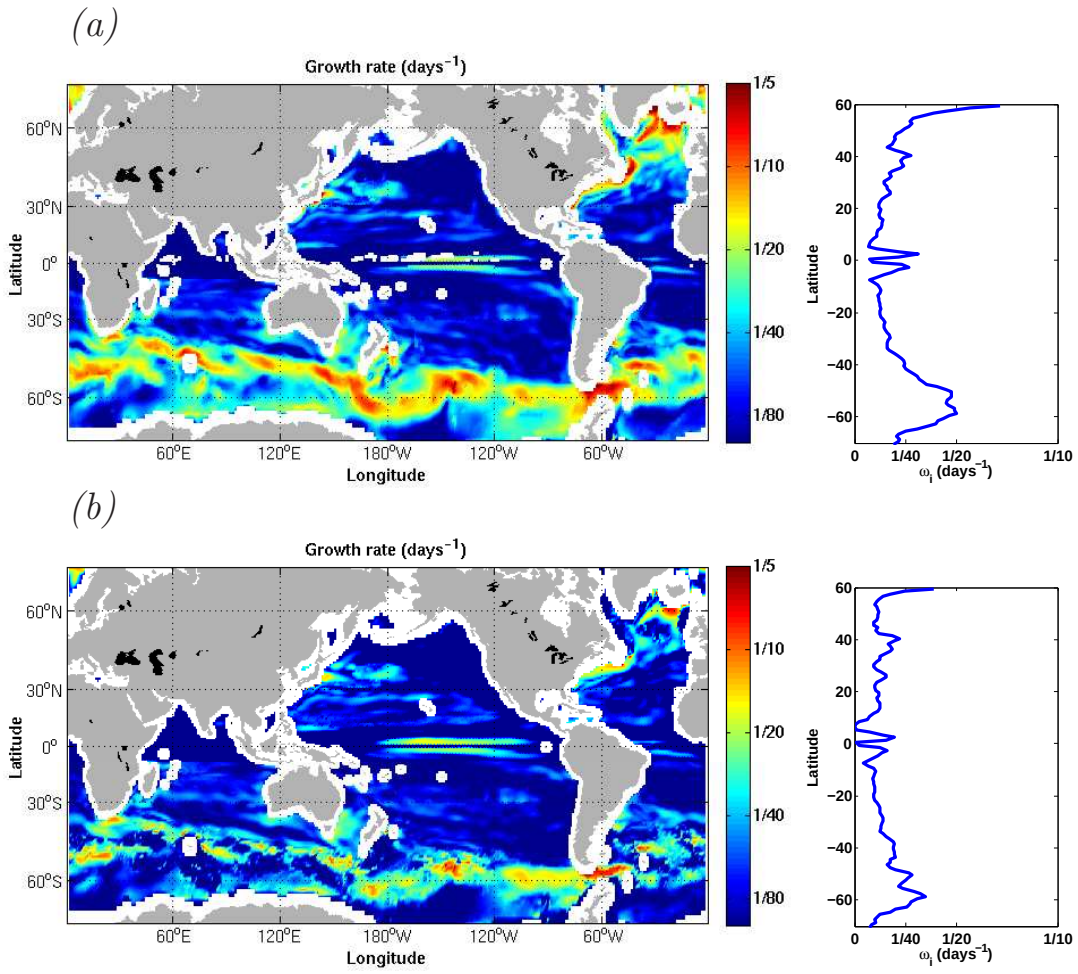

Figure 4.12: (Upper panel) Maximum baroclinic growth rates over a grid in (k, ℓ)–space. See text for details of the wavenumber grid. (Lower panel) Maximal growth rates given $\ell = 0$. Zonal averages are shown on the right.

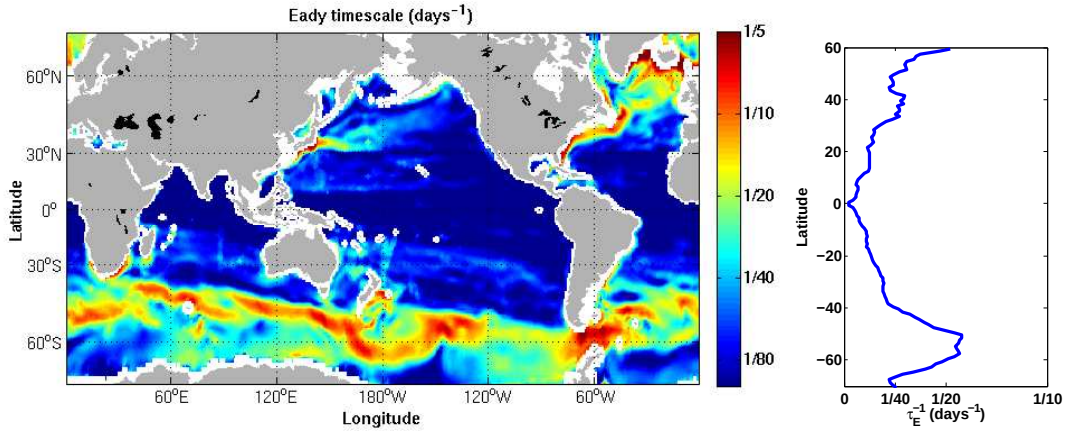

Figure 4.13: An alternative measure of the baroclinic growth rate, the "Eady time scale".

As an alternative measure of baroclinic growth rate, Smith (2007); Stammer (1997); Treguier et al. (1997) considered the "Eady time scale" τ_E, where

$$\tau_E^{-1} = f\sqrt{\frac{1}{6H}\int_{-H}^{0}\frac{dz}{\mathrm{Ri(z)}}}, \qquad \text{where} \qquad \mathrm{Ri(z)} = \frac{\mathrm{N}^2}{\mathrm{U_z^2 + V_z^2}}$$

is the Richardson number. The global map of the inverse of the "Eady time scale" in Figure 4.13 shows that it is consistent with the linear baroclinic growth rate, although perhaps slightly larger. The most obvious difference between Figure 4.13 and Figure 4.12 is the lack of the low latitude bands as $f \to 0$ near the equator. This is because the baroclinic growth rate contains surface trapped, small scale instabilities that are smoothed over by the vertical integral in the "Eady time scale" measure.

Figure 4.14 shows the length scales associated with the growth rates in Figure 4.12, normalized by the deformation scale at each location. The most unstable

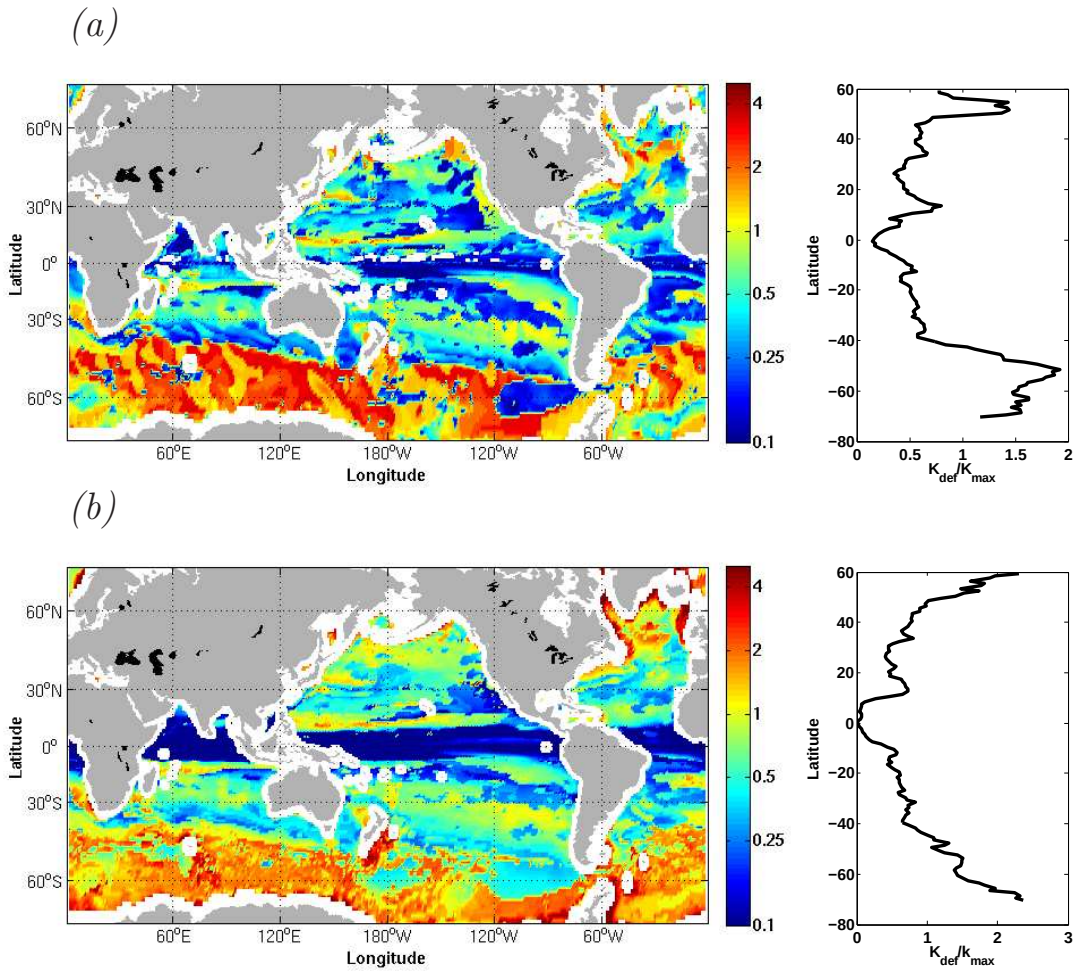

Figure 4.14: (Upper panel) Length scales of maximal growth rates in Figure 4.12 nondimensionalized by the deformation scale, *i.e.*, $\lambda_1/K_{\max}$. (Lower panel) As above but for $\ell = 0$.

length scales in the major eddying regions tend to be on the order of, or larger than, the deformation scale, and their vertical structures (not shown) tend to deep, first baroclinic. Outside of the major eddying regions the most unstable growth occurs at scales smaller than the deformation scale, and the vertical structure tends to be shallow, or surface trapped.

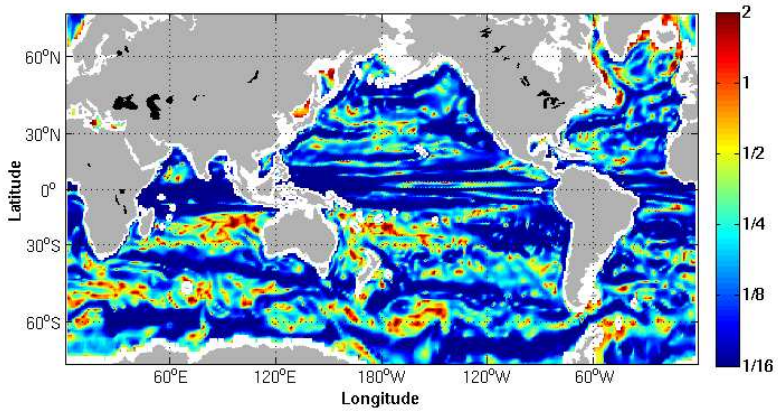

Figure 4.15: The transition length scale computed using Equation (4.4) nondimensionalized by the deformation scale, *i.e.,* λ_1/K_t, see text for details. Note that the color axis is saturated at the small (blue) end.

4.3.2 Global map of transition scale

Figure 4.15 shows a global map of the transition scale given by Equation (4.4), nondimensionalized by the deformation scale, *i.e.,* λ_1/K_t, computed from the Forget (2008) ocean atlas. The transition scale appears to be negatively correlated with maximum baroclinic growth rate, although there are notable exceptions. The eddying regions tend to have large growth rates, which are at large horizontal scales with deep, first baroclinic vertical structure. In much of these regions the transition scale λ_1/K_t is quite small. Conversely, the maximum growth rate in the non-eddying regions tends to be weaker, at smaller horizontal scales, and surface trapped. Consistent with this, the predicted transition length scale for the transition from QG to SQG dynamics is larger in such regions, most notably East and West of Australia. Le Traon (1993) and Stammer (1997) have showed that the SSH spectra are steeper in the Gulf Stream compared to the mid-Atlantic,

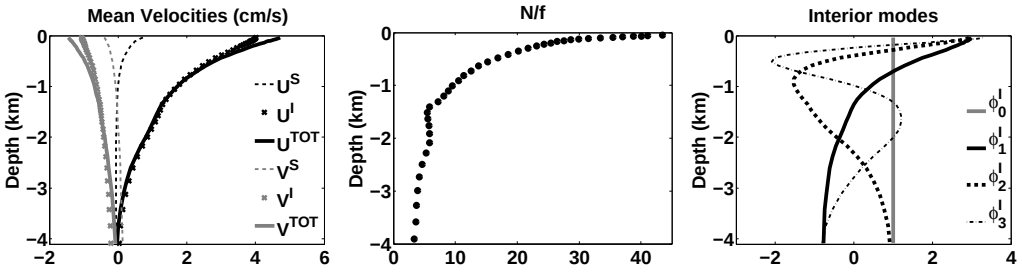

Figure 4.16: Mean state at 130°E, 60°S. (Left panel) Mean velocity. Solid lines are the total zonal (black) and meridional (gray) velocities, and dashed lines are the component of the flow due to the surface gradient, and x's are the component of the flow due interior shear. (Middle panel) The stratification nondimensionalized by the local Coriolis frequency N/f. (Right panel) The first four neutral modes.

suggesting that surface modes, which would have shallower SSH spectral slopes, may be less important in the Gulf Stream[4].

4.3.3 Simulation at a location in the ACC

To validate the scaling for the transition wavenumber we consider an example nonlinear simulation at 130°E, 60°S in the ACC. The mean velocities, stratification (normalized by the local Coriolis frequency), and the first four neutral modes at 130°E, 60°S are shown in Figure 4.16. Being in the ACC this region is dominated by zonal flow that is primarily first baroclinic. There is a kink in the stratification just below 1km which is likely a source of instability at depth.

[4]Note that the observed SSH spectral slopes also tend to be uniformly shallower than theory predicts. Le Traon et al. (2008) argues for SSH spectral slopes of $K^{-11/3}$ in the main eddying regions, which would correspond to a $K^{-5/3}$ KE slope, as in SQG. Meanwhile Stammer (1997) argues for a slope "close to K^{-5} toward smaller scales", although none of the spectra he shows are steeper than K^{-4}. Stammer and Böning (1992) did however show K^{-5} in the Gulf Stream and slopes as shallow as K^{-2} away from East of the Gulf Stream. Le Traon (1993) obtained K^{-4} in the Gulf Stream and approximately K^{-3} away from the Gulf Stream.

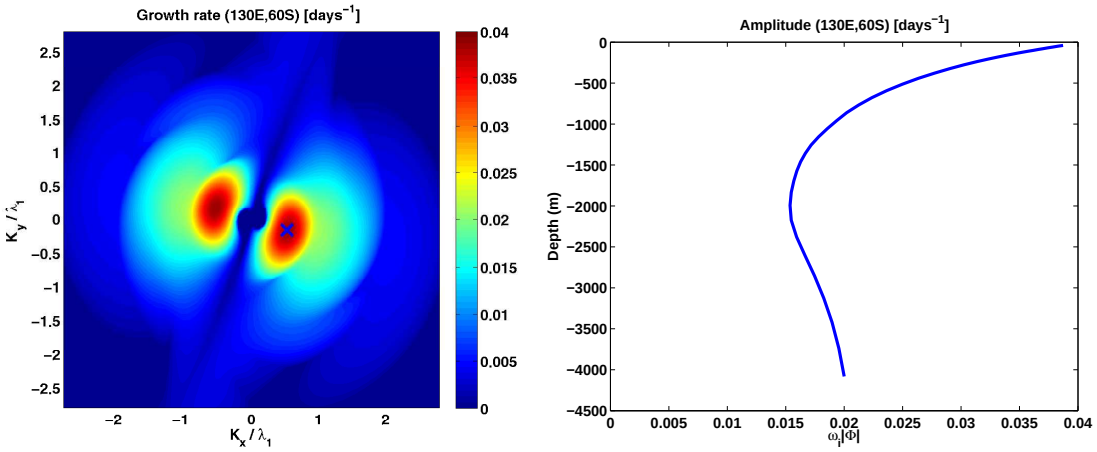

Figure 4.17: (Left panel) Linear baroclinic growth rate at 130°E, 60°S. (Right panel) Amplitude of the vertical structure of the dominant baroclinic instability, multiplied by the growth rate $\omega_i|\Phi(z)|$. The vertical structure is 62% first baroclinic, 22% second baroclinic and 13% is due to the top surface mode.

Linear instability

Indeed, computing the linear baroclinic growth rate in (k, ℓ)–wavenumber space, Figure 4.17 shows that the dominant instability is larger than the deformation scale, has about a 25 day time scale and its orientation is close to zonal. The right panel of Figure 4.17 shows that the vertical structure of the dominant instability is mostly in the first baroclinic mode (62%), with significant contributions from the second baroclinic mode (22%) and the top surface mode (13%)[5].

Nonlinear simulation

Given that the baroclinic forcing is primarily in the first baroclinic mode near the deformation scale, we expect that dynamics at the deformation scale should also

[5]The modal percentages are calculated as the absolute value of each modal weight divided by the 2-norm of the vector of all the modal weights.

be dominated by the first baroclinic mode. Figure 4.18 shows that this is indeed the case. Plotted are the KE spectra at the surface of the relevant modes from a simulation with 512^2 horizontal resolution and 8 interior vertical modes. Near

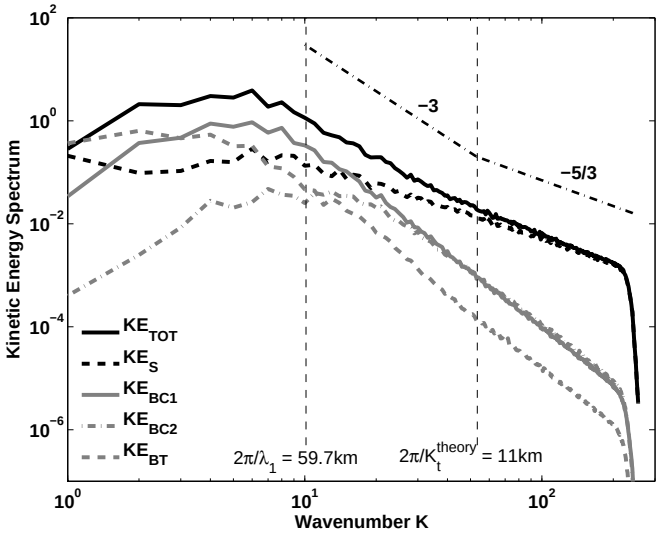

Figure 4.18: Kinetic energy spectra of the various interior modes (gray lines) and surface mode (black dashed line) at the surface at 130°E, 60°S. The total KE spectra at the surface (solid black line) transitions near the predicted scale, which is $2\pi K_t^{-1} = 11$km.

the deformation scale the first baroclinic mode (solid gray line) dominates, but the surface mode (black dashed line) dominates toward small scales and the barotropic mode (gray dashed line) dominates at the largest scales. The total KE spectrum also transitions from K^{-3} to $K^{-5/3}$ at roughly the scale predicted by the theory.

Figure 4.19 shows the KE (solid line) and APE (dashed line) spectral fluxes, as defined by Equations (4.2) and (4.3), at the surface for the simulation at 130°E, 60°S. Both fluxes are consistent with an SQG cascade (Capet et al., 2008); at small scales where the surface mode dominates the forward flux of APE is equal to the KE flux at the surface plus a APE to KE conversion term.

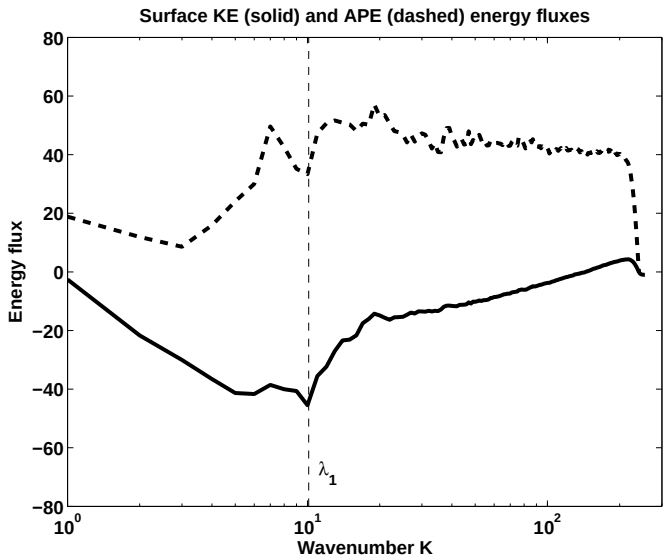

Figure 4.19: Spectral fluxes of KE (solid) and APE (dashed) at the surface for simulation at 130°E, 60°S.

4.4 Conclusions

The SMQG model was applied to the ocean to determine which dynamics, interior QG or surface QG, dominate at the surface. First, modal energy interactions were investigated in freely decaying turbulence to determine how the surface mode interacts with interior modes, which led to a slight amendment to the most likely interactions predicted by Fu and Flierl (1980). With exponential stratification the barotropic mode is suppressed, so energy in higher baroclinic modes is preferentially deposited into the first baroclinic mode. Energy in surface modes preferentially interacts with either the barotropic mode at large scales and the first baroclinic mode at deformation scales. Surface modes likely also interact with higher baroclinic modes at higher wavenumbers, though the effect, if present, is small and does not alter the spectral slope of the surface kinetic energy spectrum.

Energy spectra and fluxes indicate that the surface dynamics are largely SQG-

like at small scales, and agree with the findings of Capet et al. (2008). The transition scaling derived in Chapter 3, is refined in Equation 4.4 and shown to hold for highly non-uniform stratification. Applying this diagnostic to the World Ocean, Figure 4.15, indicates that the magnitude of surface modes ought to be comparable to interior modes in many regions. However, there appears to be an anti-correlation between regions with large transition scales (*i.e.,* prominent surface mode regions) in Figure 4.15 and regions with large baroclinic growth rates in Figure 4.12(a), although there are exceptions in convective regions in the ACC and North Atlantic near 60°N. The length scale of maximum growth in these highly unstable baroclinic regions, Figure 4.14(a), is also quite large, indicative of deep Eady-Green type instabilities. On the other hand, less baroclinically unstable regions appear to be dominated by shallow Charney type instabilities, which is consistent with SQG-like flow. These findings are also consistent with observational findings that show steeper SSH spectra in the main eddying regions and shallower SSH spectra in other regions, however all of the SSH observations are biased towards shallower spectral slopes than balanced turbulence theory predicts[6] (Stammer and Böning, 1992; Le Traon, 1993).

[6]The shallower than expected SSH spectral slopes observed in much of the world ocean are not understood. Observational error and noise might contribute, especially away from the main eddying regions where SSH anomalies are weaker.

Chapter 5

Interpretation of ocean surface phase propagation observations

In the previous chapters we used our surface-modal formulation to predict transitions between steep and shallow kinetic energy spectra downscale of the deformation scale. We showed that high vertical resolution or an analytical inversion are required to resolve the downscale surface dynamics because their vertical-horizontal aspect ratio remains constant toward small scales. In Chapter 4 we applied our transition scaling to the world ocean to predict whether the surface turbulence at deformation scales and below is dominated by interior modes or surface modes. In this chapter, we consider westward phase propagation which, for most latitudes, is typically observed at scales above the deformation scale (Chelton et al., 2007), where interior QG dynamics and surface QG dynamics are indistinguishable because they both possess $K^{-5/3}$ inverse cascades. Our goal here is to determine whether the observed phase propagation is due to linear waves or nonlinear turbulence.

First we review the noteable observation of westward phase propagation of SSH anomalies by Chelton and Schlax (1996), and the various theories that have since been proposed in the literature. In Section 5.2 we compare first baroclinic Rossby wave phase speeds calculated with the Forget (2008) ocean atlas with observed altimetric phase speeds provided by Chris Hughes. We repeat the calculations of Chelton and Schlax (1996) and Killworth and Blundell (2005) with mean flow and stratification, and topographic slopes, arriving at a conclusion consistent with Chelton et al. (2007) – in mid-latitudes, phase speeds predicted by long-wave linear theory are typically faster than observed phase speeds. In Section 5.3, where possible, we fit the phase speeds predicted by the linear model to observed phase speeds by adjusting the horizontal scale of the waves. We obtain a marked meridional variation in the scale of the fitted waves: equatorwards of $\pm 30^\circ$ the implied scale is large and gradually decreases with latitude, having an implied Rhines wavelength of about 600km. Polewards of of $\pm 30^\circ$ the linear fit begins to fail, and eventually fitted scales match the deformation scale. In section 5.4 we interpret our result via a comparison of turbulent and wave timescales. Finally we estimate the critical latitude at which waves give way to turbulence by making use of surface eddy velocities from drifter data, provided by Nikolai Maximenko.

5.1 Background

Altimetric observations of sea surface height (SSH) of the ocean show westward propagating phase anomalies in all of the major oceans except the Antarctic Circumpolar Current (ACC), the Kuroshio and the Gulf Stream, where the propagation is eastward. Chelton and Schlax (1996) attempted to understand these

observations in terms of linear, first baroclinic Rossby waves in a resting ocean and in the long-wave limit. They found that observed phase speeds were larger than predicted by theory outside the tropics by as much as a factor of two (see, for example, the introduction of Colin de Verdière and Tailleux, 2005, who review an extensive literature on the subject). Chelton et al. (2007) recently observed that SSH variability appears to be nondispersive and consistent with the behavior of nonlinear eddies in many regions of the world ocean, particularly poleward of 25°, in western basins and in the ACC. Some of the discrepancy between the observations and linear theory can be resolved by including mean flow and topography (Killworth et al., 1997; Dewar and Morris, 2000; Killworth and Blundell, 2005; Maharaj et al., 2007). We find that the "fit" of linear theory to observations at high latitudes is not as successful as at low latitudes. However, the downstream phase speed observed in the ACC is captured rather well. Less satisfying, is the mismatch of best fit speeds to observations in the 40° to 50° latitude bands. Killworth and Blundell (2005) appear to obtain a closer fit there, the reasons for which are not clear to us.

A number of authors adopt the planetary geostrophic approximation (Dewar, 1998, appendix; Killworth and Blundell, 1999, 2003; Colin de Verdière and Tailleux, 2005) and so automatically make the long-wave approximation by neglecting relative vorticity. Others have considered Rossby basin modes in the quasi-geostrophic approximation (Cessi and Primeau, 2001; LaCasce and Pedlosky, 2004). As noted by Killworth and Blundell (2005), all such calculations implicitly assume production of waves at the eastern boundary, yet their ray tracing calculations through the observed hydrography indicate that such waves are generally unable to cross the basin. Instead, Killworth and Blundell (2007) investigate

the assumption that waves are produced throughout the ocean via local forcing by winds, buoyancy exchange or baroclinic instability of the mean state; they put this assumption to use by computing the dispersion relation at each lateral position, assuming local forcing and horizontal homogenity (i.e. doubly-periodic boundary conditions for each $1^\circ \times 1^\circ$ section, the 'local approximation').

Both Killworth and Blundell (2007) and (Smith, 2007) (in a similar analysis) find that the oceans are rife with baroclinic instability, occurring at or below the deformation scale, thus providing a ready source of energy, cascading upscale from below, for the waves and turbulence seen at the ocean's surface. Indeed both altimeter observations and numerical ocean models provide evidence of an inverse spectral flux of kinetic energy from the deformation scale up to an arrest wavelength of order 500–1000 km, which decreases with latitude but does not scale closely with the deformation scale (Scott and Wang, 2005; Schlösser and Eden, 2007). Such an inverse cascade[1] is possibly the result of nonlinear interactions in geostrophic turbulence. The inverse cascade can be arrested or slowed before reaching the basin scale by Rossby waves (Rhines, 1975), stratification $N^2(z)$ (when energy is contained in baroclinic modes, particularly if N^2 is surface intensified as in the ocean — see Fu and Flierl, 1980; Smith and Vallis, 2001) or dissipative processes (Arbic and Flierl, 2004; Thompson and Young, 2006). It is not yet clear which of these processes, if any of them, sets the ultimate arrest scale.

Rhines (1975) theorized that, because the eddy timescale increases as the spatial scale grows in the inverse cascade, a transition will occur at the spatial

[1]The inverse cascade observed by Scott and Wang (2005) presented a conundrum since up to 70% of the variability at the ocean surface is contained in the first baroclinic mode (Wunsch, 1997) and it was thought that first baroclinic energy should cascade towards the Rossby radius. However Scott and Arbic (2007) showed in simulations of two-layer baroclinic turbulence, that while the total energy in the first baroclinic mode cascades towards the Rossby radius, the kinetic energy moves upscale.

scale where the eddy timescale matches that of Rossby waves with the same spatial scale. The transition scale, commonly referred to as the Rhines scale, is $L_R \sim (2u_\mathrm{t}/\beta)^{1/2}$, where u_t is the square root of the eddy kinetic energy (which, in the two-dimensional system considered, is the only energy). It is at this spatial scale, Rhines suggested, that the turbulent energy is shunted into either jets or waves, or both, depending on the strength and homogeneity of the eddy field. Numerical experiments presented in Rhines' paper demonstrate that, even when the eddies are energetic enough to form jets, Rossby waves may also be energized. Vallis and Maltrud (1993) refined the idea of a wave-turbulence crossover by noting that while the Rhines effect cannot halt the cascade alone, it inhibits energy transfer into a dumbbell-shaped region around the origin in wavenumber space, which leads to the generation of zonally elongated flow. There is some evidence for zonal jet formation in the ocean (Maximenko et al., 2005; Richards et al., 2006), perhaps a signature of the Rhines effect, in addition to the observations of waves by Chelton and Schlax (1996) and Chelton et al. (2007).

Recent research (Theiss, 2004; Smith, 2004b) has suggested that, on the giant gas planets, turbulent generation at small scales should result in jet formation in regions equatorward of some critical latitude, and a more isotropic eddy field in regions poleward of that critical latitude. Scott and Polvani (2007) confirmed that a critical latitude for jet formation does arise in direct numerical simulations of forced-dissipitave shallow-water turbulence on the sphere. Theiss (2006) extends the idea further by replacing β with the mean flow-dependent meridional potential vorticity (PV). Specifically, he derives a "generalized" Rhines scale, which includes the effect of mean shears, and a corresponding critical latitude, polewards of which jets do not form.

Following on these ideas, Eden (2007) analyzed eddy length scales in the North Atlantic Ocean both via satellite altimetry and an eddy resolving primitive equation model. At high latitudes, he shows evidence that eddy scales vary with the Rossby deformation radius, consistent with Stammer (1997), while at low latitudes eddy scales are consistent with a generalized Rhines scale. That is, eddies scale with the smaller of the deformation radius and the Rhines scale, with a critical latitude near 30°N, where the deformation scale is similar to the Rhines scale.

In this Chapter we reinterpret sea surface height (SSH) signals in the context of the aforementioned theoretical ideas. Specifically, we avoid the issue of jet formation, but assume that below a critical latitude baroclinic eddies transform some of their energy into Rossby waves, and that these waves dominate the surface height field. At higher latitudes, where Rossby wave frequencies are too small to be excited by the inverse cascade, the surface height field remains turbulent. We investigate this hypothesis as follows. Following Killworth and Blundell (2007), we compute the local Rossby wave dispersion, but rather than make the long-wave approximation, we adjust the horizontal scale of first baroclinic waves to best-fit the observed phase speeds, and thereby infer a length scale for the waves. In the tropics the fitted wavelength is close to both the Rhines scale and previously observed SSH scales. Outside the tropics, it is either impossible to match the observed phase speeds with Rossby wave speeds at any wavelength (probably because linear theory is inadequate) or the fitted wavelength lies near the deformation scale. Using surface drifter data to estimate the eddy timescale and energy level, we show that at high latitudes the turbulent timescale is faster than the Rossby wave timescale, so turbulence dominates, but at low latitudes the Rossby wave and turbulent timescales overlap, enabling the excitation of waves by turbulence.

In Section 5.2 we compare first baroclinic Rossby wave phase speeds calculated with the Forget (2008) ocean atlas with observed altimetric phase speeds provided by Chris Hughes. We repeat the calculations of Chelton and Schlax (1996) and Killworth and Blundell (2005) with mean flow and stratification, and topographic slopes. We arrive at a conclusion consistent with Chelton et al. (2007) – in mid-latitudes, phase speeds predicted by long-wave linear theory are typically faster than observed phase speeds. In Section 5.3, where possible, we fit the phase speeds predicted by the linear model to observed phase speeds by adjusting the horizontal scale of the waves. We obtain a marked meridional variation in the scale of the fitted waves: equatorwards of $\pm 30^\circ$ the implied scale is large and gradually decreases with latitude, having an implied Rhines wavelength of about 600km. Polewards of of $\pm 30^\circ$ the linear fit begins to fail, and eventually fitted scales match the deformation scale. In section 5.4 we interpret our result via a comparison of turbulent and wave timescales. Finally we estimate the critical latitude at which waves give way to turbulence by making use of surface eddy velocities from drifter data, provided by Nikolai Maximenko. In Section 5.5 we conclude.

5.2 Linear Rossby waves

Rossby waves result from the material conservation of potential vorticity (PV) in the presence of a mean gradient. As a parcel moves up or down the background mean PV gradient, its own PV must compensate, generating a restoring force toward the initial position. The result is a slow, large-scale westward propagating undulation of mean PV contours. Mean currents change the structure

of the waves in two ways: by altering the background PV gradient (sometimes so much so that β is negligible), and by Doppler shifting the signal. A number of authors (Killworth et al., 1997; Dewar and Morris, 2000; Killworth and Blundell, 2005; Maharaj et al., 2007) have shown that the straightforward inclusion of the mean thermal-wind currents in the linear Rossby wave problem leads to a much closer agreement between the observed phase speeds and theory. Here we take an approach closest to Killworth and Blundell (2007) (see also Smith, 2007) and compute phase speeds in the local quasi-geostrophic approximation, using the full background shear and stratification in a global hydrographic dataset. Our focus, however, is on attempting to fit the linear results to the satellite data and thereby determining the limitations of linear wave theory when mean effects are fully included, and characterizing the scale of the waves that are consistent with the observed phase speeds. We now briefly outline the approach, relegating details to the Appendix A.7.

We assume, away from coasts, that the Rossby wave and eddy dynamics of the ocean at each latitude, longitude coordinate may be represented by the linearized inviscid quasi-geostrophic equations on a β-plane with slowly varying local mean velocity(see Pedlosky, 1984)[2]. In the interior, linear QG potential vorticity is linearly advected by the mean flow

$$\partial_t q + \mathbf{U} \cdot \nabla q + \mathbf{u} \cdot \nabla Q = 0, \qquad -H < z < 0, \tag{5.1}$$

where $\mathbf{U} = U(x, y, z)\hat{\mathbf{x}} + V(x, y, z)\hat{\mathbf{y}}$ is the local mean velocity, $q = \nabla^2\psi +$

[2]Note that in this Chapter we will use a layered formulation in the vertical since we are concerned with waves at or above the deformation scale. At these large horizontal scales, surface dynamics will be resolved by the layered formulation.

$(f^2/N^2\psi_z)_z$ is the quasi-geostrophic potential vorticity (QGPV), f is the local Coriolis parameter, H is the local depth of the ocean, $N^2(z) = -(g/\rho_0)d\overline{\rho}/dz$, and the eddy velocity is $\mathbf{u} = -\psi_y\hat{\mathbf{x}} + \psi_x\hat{\mathbf{y}}$. The mean QGPV gradient ∇Q, includes horizontal shear[3], and is given by

$$\nabla Q = \left[V_{xx} - U_{yx} + \left(\frac{f^2}{N^2}V_z\right)_z\right]\hat{\mathbf{x}} + \left[\beta + V_{xy} - U_{yy} - \left(\frac{f^2}{N^2}U_z\right)_z\right]\hat{\mathbf{y}}. \tag{5.2}$$

At the rigid lid upper boundary buoyancy is linearly advected

$$\partial_t b + \mathbf{U}\cdot\nabla b + \mathbf{u}\cdot\nabla B = 0, \qquad z = 0, \tag{5.3}$$

where the buoyancy anomaly is defined as $b = f\psi_z = -g\rho/\rho_0$, the mean buoyancy is $B = -g\overline{\rho}/\rho_0$, so the mean buoyancy gradient, via thermal wind balance, is $\nabla B = fV_z\hat{\mathbf{x}} - fU_z\hat{\mathbf{y}}$. Slowly varying bottom topography is included using the approach of Smith (2007), using the Smith and Sandwell (1997) global seafloor topography dataset; see the appendix for details.

Assuming a wave solution $\psi(x,y,z,t) = \Re\{\hat{\psi}(z)\exp[i(kx+\ell y-\omega t)]\}$, and likewise for q and b, one obtains the linear eigenvalue problem,

$$(\mathbf{K}\cdot\mathbf{U} - \omega_n)\ \hat{b}_n = (\ell B_x - kB_y)\ \hat{\psi}_n, \qquad z = 0, \tag{5.4a}$$

$$(\mathbf{K}\cdot\mathbf{U} - \omega_n)\ \hat{q}_n = (\ell Q_x - kQ_y)\ \hat{\psi}_n, \qquad -H < z < 0, \tag{5.4b}$$

where $\mathbf{K} = (k,\ell)$, and $\hat{\psi}_n$ is the n^{th} eigenvector, sometimes called a 'vertical shear mode', and $\hat{q}_n$ and $\hat{b}_n$ are linear functions of $\hat{\psi}_n$. (The hat notation implies dependence on the wavenumber $\mathbf{K}$, which is suppressed for clarity). The eigenvalues

[3]Horizontal shears of the mean state contribute little to ∇Q (Smith, 2007), but we retain them in our calculations for completeness.

ω_n are the frequencies of the wave solutions, with the real part resulting in phase propagation and imaginary parts, if they exist, producing growth or decay of the wave. The problem is discretized in the vertical using a layered formulation; in the discretized case, there are as many shear modes as there are layers. The expressions for the discrete surface buoyancy $\hat{b}$ and $\hat{q}$ in terms of $\hat{\psi}$, and other details of the discretization can be found in Appendix A.7, and in Smith (2007).

Equation (5.4) is solved by first considering the neutral modes, which diagonalize the vertical derivatives in the stratification operator as follows. For a resting ocean ($\mathbf{U} = 0$, implying $B_x = B_y = Q_x = 0$ and $Q_y = \beta$), Equation (5.4) reduces to the standard Rossby wave dispersion relation

$$\omega_m = \frac{-k\beta}{K^2 + K_m^2}, \tag{5.5}$$

where $K = |\mathbf{K}|$ and K_m is the m^{th} deformation wavenumber, which is given by the following Sturm Liouville problem

$$\frac{d}{dz}\left(\frac{f^2}{N^2}\frac{d\Phi_m}{dz}\right) = -K_m^2\Phi_m, \qquad \left.\frac{d\Phi_m}{dz}\right|_{z=0} = \left.\frac{d\Phi_m}{dz}\right|_{z=-H} = 0. \tag{5.6}$$

The eigenfunctions Φ_m are often called the 'neutral modes'; they form an orthonormal basis of the vertical structure in a resting ocean.

The mean velocity and buoyancy fields are computed from the ocean atlas of Forget (2008), as described in Appendix A.7, and these are used to construct the mean buoyancy and PV gradients. At each lateral position in the ocean, we then compute the neutral modes and their deformation scales from (5.6), as well as ω_n and $\hat{\psi}_n$ from the complete dispersion relation (5.4). We denote the zonal phase

speed of this mode as

$$c_{\mathrm{R}} = \frac{\omega_n}{k}.$$

5.2.1 Observations of phase propagation from altimetry

In the long-wave, resting ocean limit, the dominant first baroclinic mode has a westward phase speed given by equation (5.5) with $\mathbf{K} = 0$, so $c_{\mathrm{R}} = \beta/K_1^2$. A zonal average of the long-wave phase speed is computed over the central pacific (170°W to 120°W), and plotted against latitude in Figure 5.1. Also plotted are phase propagation observations provided by C. Hughes (2007, personal communication), zonally averaged over the same range. Speeds at latitudes 20°S and 20°N are well captured by the classic long Rossby wave solution. However departures are observed at both low latitudes and high latitudes. Observed speeds reach a maximum near ±5°. Poleward of 20° the Rossby wave solution diverges from the observations, reaching roughly a factor of two (Chelton and Schlax, 1996), and eastward propagation in the ACC region is also not captured. Figure 5.2 shows global maps of phase speed, "wavelikeness" and amplitude from Hughes' dataset.[4] Wavelikeness measures the precision of the distribution of phase speeds computed via a Radon transform at a given latitude, so one can already see from Figure 5.2 that low latitudes propagate mostly at coherent phase speeds while high latitudes exhibit a larger spread of propagation speeds, likely indicating a more turbulent

[4]The observed propagation speeds were calculated by Hughes from SSH observations in the following way. First, thin longitude (5 degrees) and tall time (11.5 years) strips are bandpassed filtered in time from 5 to 57 weeks, then zonally averaged (at each time) and the annual and semiannual cycles are removed. A Radon transform was then performed by shifting each longitude such that signals traveling at a speed c line up horizontally, summing over longitude and taking the standard deviation in time. A "wavelikeness" parameter is also computed as the peak value of the Radon transform divided by its mean. Based on advice from Hughes we have filtered out observations with wavelikeness less than 1.5. Figure 5.2 shows global maps of the observed phase speed, wavelikeness (with black contour at 1.5), and a measure of wave amplitude.

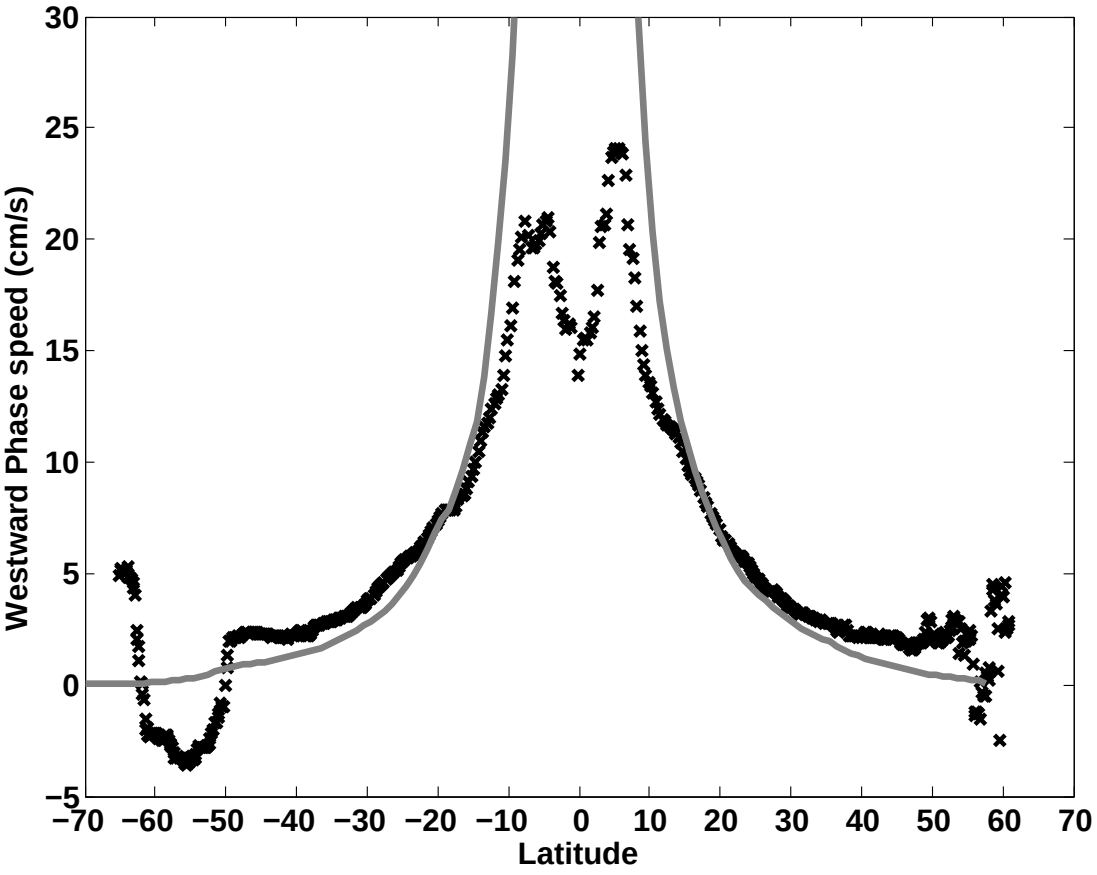

Figure 5.1: Westward phase speed estimated from Hughes' data averaged from 170°W to 120°W (black x's) plotted against the standard linear, first baroclinic, long Rossby wave phase speed (solid line), computed from the Forget (2008) atlas.

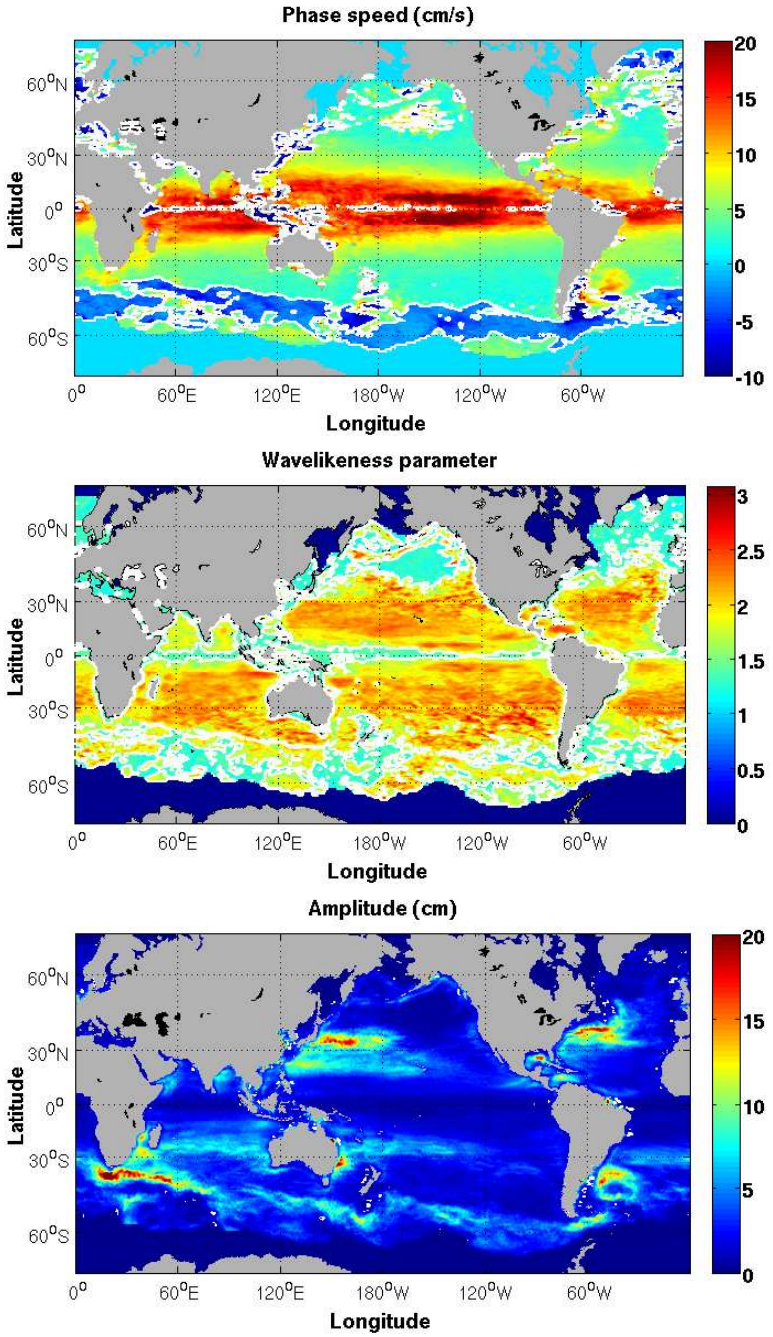

Figure 5.2: Hughes' analysis of surface altimetric data. Phase speed (upper panel) "wavelikeness" (middle panel — see text for details), with contour at 1.5 to differentiate regions that are wavelike and not wavelike, and a measure of amplitude (lower panel).

flow.

5.2.2 Applicability of linear theory

We now consider the effects of including $\mathbf{U}$ and ∇Q, as estimated from the Forget (2008) atlas, using the dispersion relationship (5.4) then setting $\mathbf{K} = 0$ (i.e. the long-wave approximation). For each location we choose the vertical shear mode $\hat{\psi}_n$ whose real part projects the most onto the first neutral mode $\Phi_z(z)$ after its mean is subtracted and it is normalized[5].

The zonally averaged (from (170°W to 120°W) phase speeds are represented by the solid gray line in Figure 5.3. The observed central Pacific phase speeds from Figure 5.1 are also replotted for comparison. The long-wave limit predicts speeds which are too fast in low latitudes and typically (but not always) too slow in high latitudes. It is pleasing, however, to now observe eastward propagation in the ACC, a consequence of downstream advection by the mean current.

The assumed spatial scale of the waves also affects the predicted phase speeds. The same computation described above, but with deformation-scale waves ($\mathbf{K} = K_1\hat{\mathbf{x}}$), gives the dashed gray line in Figure 5.3. Assuming the deformation scale as a lower limit for the wavelength of the observed waves, the solid and dashed lines in Figure 5.3 bracket the range of values one can obtain for the phase speed from linear theory. We address this range of possibilities more fully in the next section.

[5]Specifically, we choose $\hat{\psi}_n$ such that

$$\max_n \int \Phi_1 \left(\hat{\psi}_n - \overline{\hat{\psi}_n}\right) dz \Big/ \int \left(\hat{\psi}_n - \overline{\hat{\psi}_n}\right)^2 dz.$$

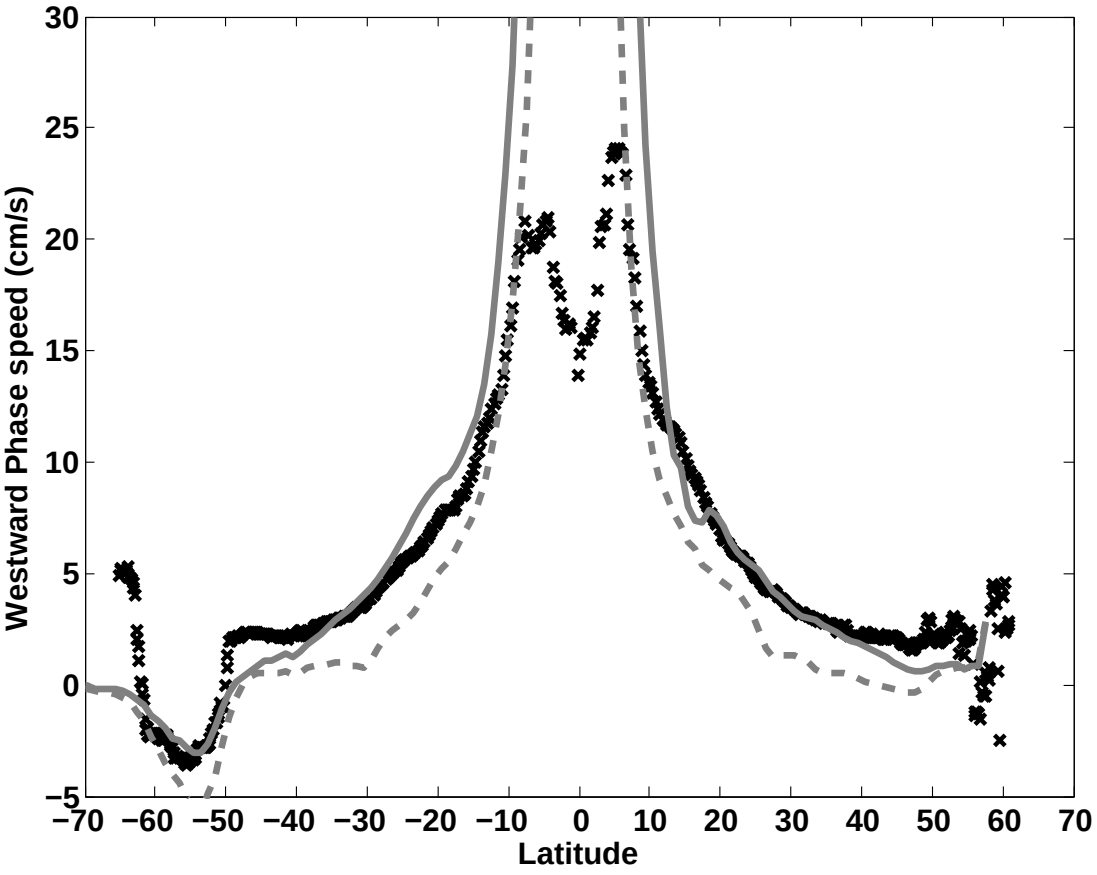

Figure 5.3: Hughes' phase speed observations (black x's) compared to linear theory in the presence of a mean current: long-waves (gray solid line) and deformation scale waves (gray dashed line).

5.3 Fitting linear model phase speeds to observations

Traditionally, the long-wave approximation has been used when interpreting altimetric signals in terms of Rossby wave theory. The influence of horizontal scale on Rossby wave speed has largely been neglected, except for calculations assuming uniform wavelengths of 500 km and 200 km reported in Killworth and Blundell (2005). Chelton et al. (2007) argue that the propagation of the observed SSH variability is due to eddies rather than Rossby waves, and remark that, equatorward of 25°, eddy speeds are slower than the zonal phase speeds of nondispersive baroclinic Rossby waves predicted by the long-wave theory. Here we show, however, that such a difference in speed can be accounted for by linear Rossby waves when their wavelengths are chosen appropriately.

Using Equation (5.4) in its most general form, including bottom topography, Figure 5.4 shows both the best-fit phase speeds (left) and the wavelengths associated with those phase speeds (right) for a zonal average from 170°W to 120°W in the Pacific (upper panel) and a global zonal average (lower panel). We have assumed that the fitted waves have an east-west orientation ($\ell = 0$). Setting $k = \ell$ makes little difference in the fitted wavelength, which is consistent with the finding in Killworth and Blundell (2005) of a weak dependence of phase velocity on orientation. In the fitted wavelengths plots, the black x's correspond to individual latitudes, the solid gray curve is a smoother version of the black x's[6], and the thin

[6]The fitted wavelengths are smoothed across latitudes using a 1-1-1 smoother defined by:

$$\lambda_i' = (\lambda_{i-1} + \lambda_i + \lambda_{i+1})/3,$$

where λ_i is the wavelength at latitude i and λ_i' is the smoothed value.

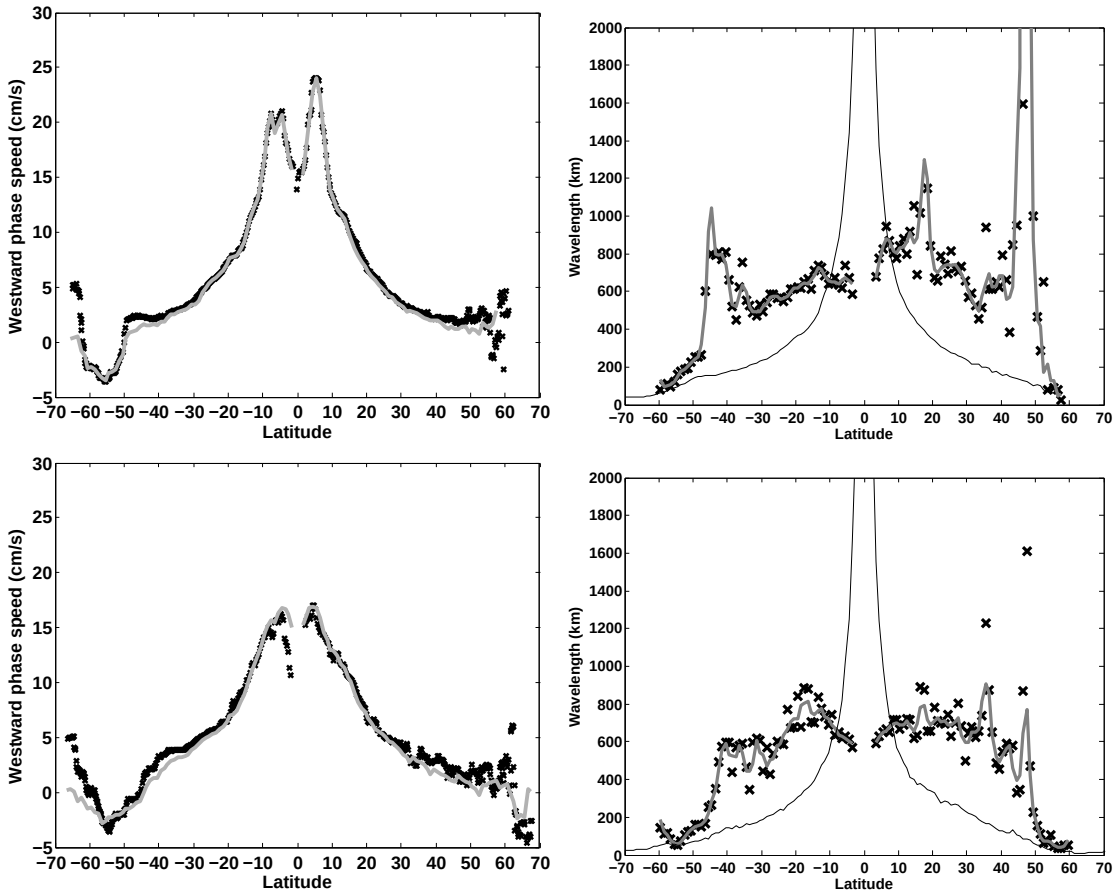

Figure 5.4: Top left: Phase speeds according to linear theory (solid gray line) adjusted to give the best match to Hughes' data (black x's). The fit is done for a zonal average over 170°W to 120°W in the Pacific. Top right: Fitted wavelengths at each latitude (black x's, gray line is a smoothed version) along with the deformation scale (thin solid line). Bottom panels: As in the top panels but zonally averaged across all oceans.

black line is the first deformation wavelength. The fitted wavelengths typically lie between 600 km and 800 km in the tropics out to about 30°, with little or no dependence on the deformation wavelength. Note that the baroclinic Rhines scale (not shown) is roughly constant in the tropics, with a wavelength between 500km and 700km, and diverges to infinity when the turbulent velocity surpasses the longwave resting phase speed near ±20° (see below). There is a gap in fitted wavelength around ±40° where the linear theory fails to capture the observed phase speeds. At high latitudes, the best-fit is obtained assuming scales near the deformation scale. The inability to fit the phase speeds at higher latitudes is suggestive that the 'wave' signal is not linear in those regions. Clearly, though, the inclusion of wavelengths that result from a best-fit of theoretical to observed phase speeds results in a greatly improved match between linear theory and observations.

Figure 5.5 shows the importance of the planetary vorticity gradient β relative to the effect of mean flow $\mathbf{U}$ on the mean QGPV gradient ∇Q. Using the length scales computed by the best-fit algorithm, we plot the phase speeds that result from setting $\beta = 0$ while keeping the observed $\mathbf{U}$ (thick dashed-dotted line), as well as the phase speeds that result from setting $\mathbf{U} = 0$ and $\nabla Q = \beta\hat{\mathbf{y}}$ (thin dashed line). [The solid gray line and black x's are the same as those plotted in the upper left panel of Figure 5.4.] The planetary gradient β is crucial in the tropics, while in the subtropics $\mathbf{U}$ becomes increasingly important, particularly from 35°S to 20°S, where the mean shear accounts for much of the factor-of-two phase speed error discussed in Chelton and Schlax (1996). At high latitudes the Doppler shift caused by $\mathbf{U}$ is crucial in capturing the downstream propagation in the ACC. Figure 5.5 also shows the effect of bottom topography on phase speed. Killworth and Blundell (2003) and Maharaj et al. (2007) showed that topography

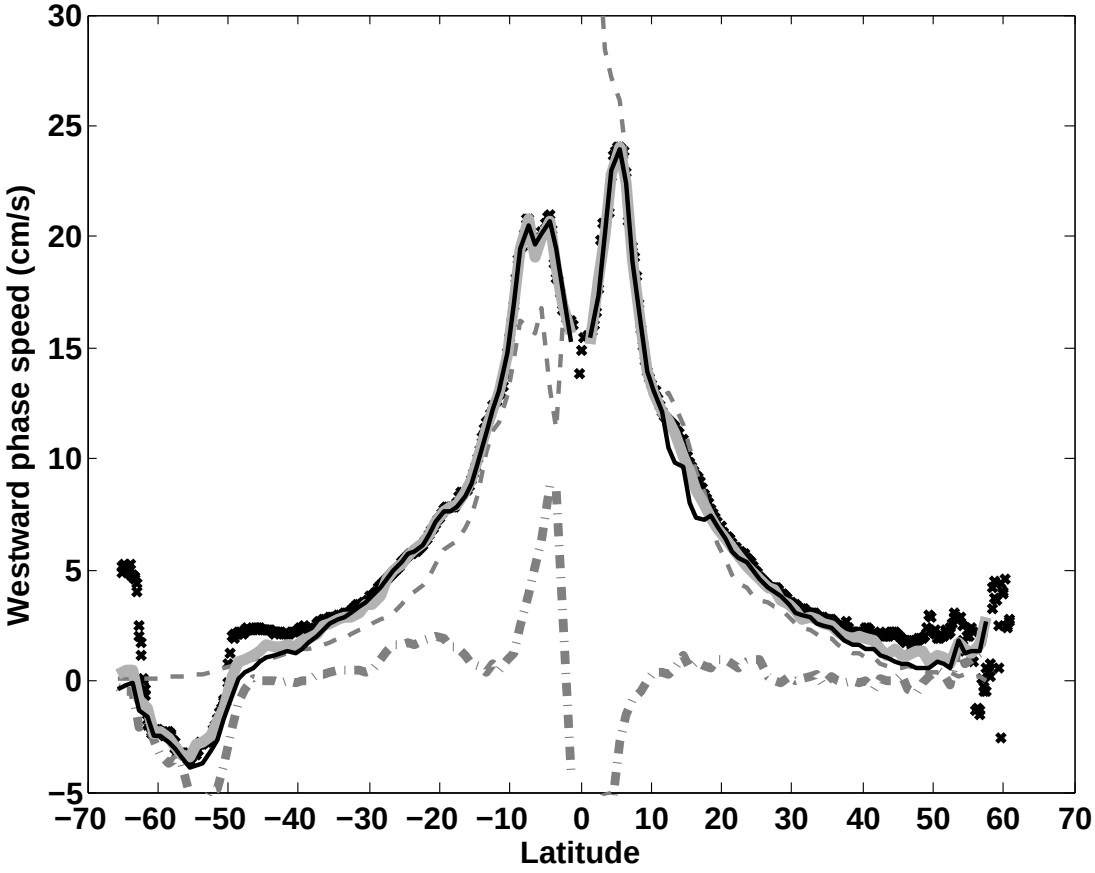

Figure 5.5: The effects of β, mean currents and topography on the prediction of phase speed from linear theory. The thick gray line corresponds to the full theory with mean flow $\mathbf{U}$, β, and bottom topography. The thin black line contains $\mathbf{U}$ and β but excludes topography. The thin dashed line only contains β and no mean flow, while the thick dash-dotted line contains only $\mathbf{U}$. In all cases the best-fit horizontal scales are used (the x's and thick gray solid line are identical to those in the top left panel of Figure 5.4).

is only important in the presence of a mean flow. Here the best fit phase speeds with mean flow and a flat bottom (thin black line) are compared with the best fit speeds with topography (thick gray line). The fit is slightly better from 40° to 50° but the addition of topography is still not enough to completely fit the observations.

5.4 Wavelike and turbulent regimes in the ocean

A plausible interpretation of the results presented in Section 5.3 is that in low latitudes, baroclinic eddies give their energy to linear Rossby waves, whereas at high latitudes Rossby waves are less easily generated, and the SSH field remains dominated by eddies. This can be understood in terms of a matching, or otherwise, of turbulent and wave timescales, as discussed in the barotropic context by Rhines (1975) and Vallis and Maltrud (1993), and in a (first-mode) baroclinic context applied to the gas planets by Theiss (2004), Smith (2004b) and Theiss (2006). The central idea of the Rhines effect is that, as eddies grow in the inverse cascade, their timescale slows, and when this timescale matches the frequency of Rossby waves with the same spatial scale, turbulent energy may be converted into waves, and the cascade will slow tremendously. When this idea is applied to a putative interaction with *baroclinic* Rossby waves, there is the added complication that frequencies tend toward 0 at large scale (see Figure 5.6). In this case, only sufficiently weak eddies have timescales, at any wavelength, that intersect the Rossby wave dispersion curve.

For illustrative purposes, one can estimate the wavenumber at which the intersection occurs by assuming a turbulent dispersion relationship of the form

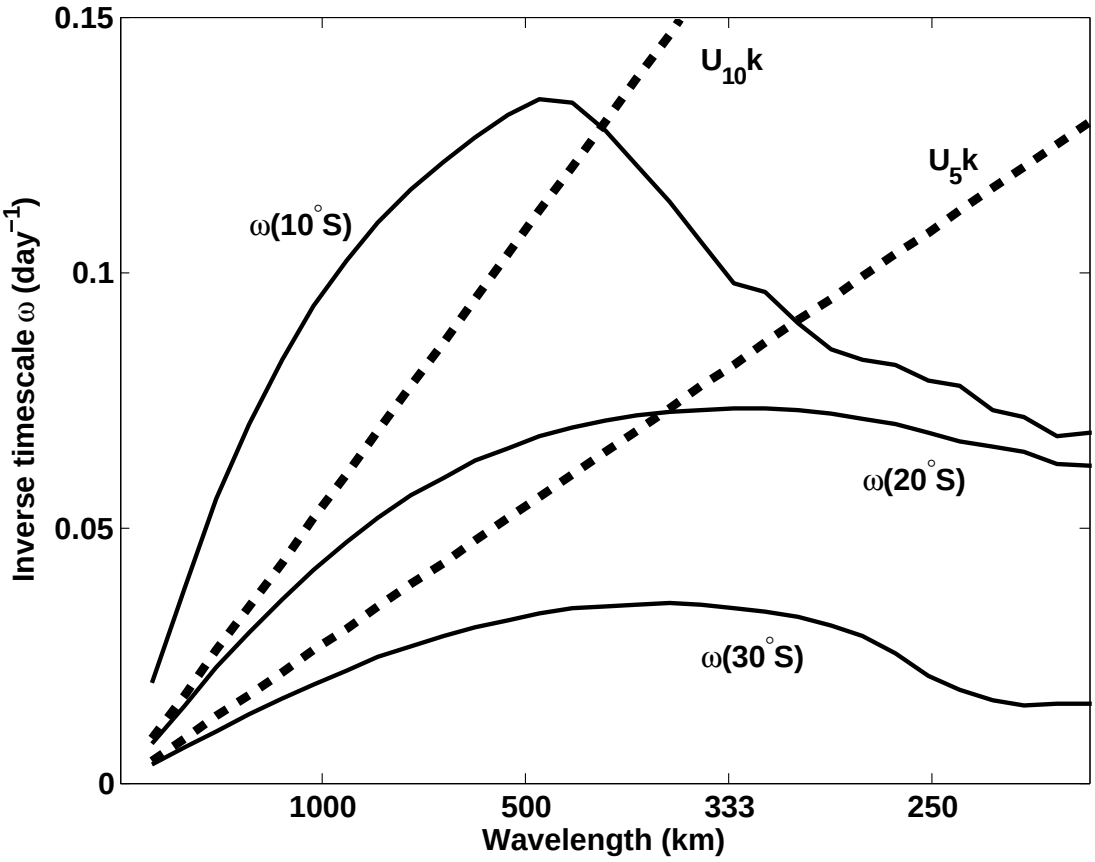

Figure 5.6: Dispersion relations for fitted phase speeds as a function of zonal wavelength (with meridional wavenumber $\ell = 0$) for latitudes in the South Pacific ($10°S$, $20°S$ and $30°S$), compared with $\omega_t = ku_t$ with two values of u_t: 5 and 10 cm s^{-1} (dashed lines).

$\omega_{\mathrm{t}} = ku_{\mathrm{t}}$, where u_{t} is the turbulent velocity scale (the square root of the appropriate eddy kinetic energy). Setting this equal to the absolute value of the approximate Rossby wave frequency ($\omega_{\mathrm{R}} \simeq -kQ_y/(K^2 + K_1^2)$ assuming that Q_x is small and U is either small or constant in z), we have (dividing by k)

$$u_{\mathrm{t}} \sim \frac{Q_y}{K_1^2 + K^2}. \tag{5.7}$$

Solving for K gives the relationship $K^2 = Q_y/u_{\mathrm{t}} - K_1^2$, for which there is a real solution only if $Q_y/u_{\mathrm{t}} > K_1^2$. At fixed Q_y and K_1, the implication is that waves can be generated (and the cascade inhibited) only when the turbulent energy is sufficiently small. On the other hand, assuming a constant u_{t}, and noting that Q_y (through its dependence on β) and K_1 (which is proportional to f) are dependent on latitude, the relationship (5.7) implies the existence of a critical latitude, polewards of which no intersection is possible.

Let us now see what the data suggests about a relationship like (5.7). We replace the approximate Rossby wave dispersion relation with the frequencies from (5.4), using the fitted Rossby wave scales described in the previous section. The idea is illustrated in Figure 5.6, which shows zonally averaged Rossby wave frequency curves $\omega_{\mathrm{R}}(k)$, plotted against zonal wavelength, at three latitudes in the tropical Pacific Ocean. Two hypothetical eddy frequency curves $\omega_{\mathrm{t}} = ku_{\mathrm{t}}$ (dashed lines) are added for comparison, with $u_{\mathrm{t}} = 10$ cm s^{-1} and $u_{\mathrm{t}} = 5$ cm s^{-1}. At 10°S the eddy frequency curves intersect the Rossby wave frequencies at relatively small wavelengths, indicating that observed tropical SSH length scales are certainly in the wave region. On the other hand, at 30°S even the 5 cm s^{-1} curve fails to intersect $\omega_{\mathrm{R}}(k)$. We thus expect little wavelike activity outside the tropics.

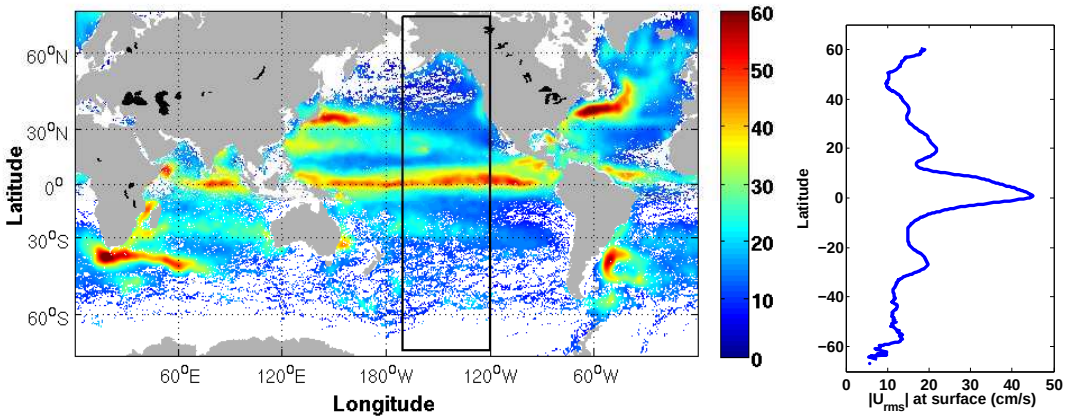

Figure 5.7: Root mean square eddying surface velocities (left) from N. Maximenko's drifter data, and zonal average thereof (right).

We can improve the frequency comparison test further by using observations of surface drifter speeds to obtain estimates of u_{t}. A global map of the root mean square (rms) of the surface drifter data

$$u_{\mathrm{rms}}(0) = \sqrt{|\mathbf{u}'_{\mathrm{drifter}}(z=0)|^2}$$

(courtesy of Nikolai Maximenko) is shown Figure 5.7, with its zonal average over 170°W to 120°W (the region within the rectangle) plotted on the right. The zonal average is strongly peaked at the equator, and more constant at extra-tropical latitudes. However, this may not be indicative of the distribution of depth-integrated eddy kinetic energy, since the surface velocity gives no information about the vertical structure of eddying motion. Additional assumptions are necessary to extract the relevant eddy velocity scale.

Wunsch (1997) showed that, away from the equator, eddy velocities are primarily first-baroclinic, with a smaller projection onto the barotropic mode, while nearer the equator, motions tend to have a more complex vertical structure, pro-

jecting onto many higher modes, approaching equipartition. Expanding $\mathbf{u}'_{\rm drifter}(z)$ in the neutral modes (5.6), we have

$$\mathbf{u}'_{\rm drifter}(z) = \sum_{m=0}^{\mathcal{N}-1} \Phi_m(z)\mathbf{u}_m.$$

Following Wunsch (1997), we extract the vertical structure at each location by assuming that *the rms velocity projects entirely onto the first baroclinic mode*, which gives $u_1 = u_{\rm rms}(0)/\Phi_1(0)$. We take the relevant eddy velocity scale to be the root vertical-mean square velocity, thus

$$u_{\rm t} = \left[\frac{1}{H}\int_{-H}^{0} u_{\rm rms}(z)^2\, dz\right]^{1/2} = u_{\rm rms}(0)/\Phi_1(0)$$

where we have used the orthonormality of the neutral modes.[7] The scaling by the first baroclinic mode has the effect of reducing the estimated turbulent velocity scale in regions of strongly surface intensified stratification, such as near the equator. In these regions, the first baroclinic mode itself is quite surface intensified, so $\Phi_1(0)$ can be considerably larger than one (see the modal structure in Figure 4.10). Physically, if the first neutral mode, onto which all the motion is assumed to project, is very surface intensified, then eddy velocities are weak at depth, so the total turbulent velocity estimate is diminished.

[7]Suppose, instead of assuming that all the energy was in the first baroclinic mode, we imagined that $U(z)$ projected equally onto the barotropic and first baroclinic mode. Then

$$u_{\rm t} = \left[\frac{1}{H}\int u_{\rm rms}(z)^2\, dz\right]^{1/2} = \frac{u_{\rm rms}(0)}{1+\Phi_1(0)}\left[\frac{1}{H}\int (1+\Phi_1(z))^2 dz\right]^{1/2} = \frac{\sqrt{2}\; u_{\rm rms}(0)}{1+\Phi_1(0)},$$

since the modes are orthonormal. In the world ocean $2 \le \Phi_1(0) \le 4$, so the ratio of this projected value to one which is entirely first baroclinic, as assumed in the text, is $0.94 \le \sqrt{2}\Phi_1(0)/[1+\Phi_1(0)] \le 1.13$. An assumption of equipartition among $\mathcal{N}$ vertical modes unambiguously *reduces* $u_{\rm t}$, roughly by a factor of roughly $\sqrt{\mathcal{N}}$.

Figure 5.8 shows the eddy velocity scale $u_{\rm t}$ and zonal Rossby phase speed $c_{\rm R}$ zonally averaged over 170°W to 120°W and plotted against latitude. These are essentially the left hand and equivalent right hand sides of Eq. (5.7). Our Figure 5.8 is similar to Fig. 3 of Theiss (2006) for Jupiter, except that here our dispersion relation is computed from the full vertical structure of the mean flow, rather than just the first baroclinic component (because of the dominance of the first baroclinic mode, however, the first baroclinic calculation is rather similar — not shown). Note that $u_{\rm t}$ is nearly constant with latitude, varying between and 5 and 10 cm s^{-1} — the strong equatorial values have been reduced, through projection onto the surface-intensified first baroclinic mode, as explained above (if one assumed equipartition, the velocity estimate in the equatorial region would be reduced even further). In contrast, the (Doppler-shifted) Rossby wave speed varies markedly, exceeding 20 cm s^{-1} in the tropics and falling toward zero at higher latitudes (and even becoming prograde in the ACC). The cross-over between the two curves occurs at a latitude of roughly ±25°. Note that since we have assumed that the turbulent velocity scale $u_{\rm t}$ is entirely in the first baroclinic mode, the crossover latitudes should be considered as lower bounds.

The lower plot in Figure 5.8 shows the ratio of linear phase speeds $c_{\rm R}$ to the eddy velocity scale $u_{\rm t}$, with dashed lines denoting $c_{\rm R}/u_{\rm t} = 2$ and $1/2$. Theiss (2006) shows that stormy regions on Jupiter are highly correlated with regions where this ratio is less than one. Notably, ±25° is also the crossover latitude between linear wavelike behavior and nonlinear eddies found by Chelton et al. (2007). Outside this latitude band, first-baroclinic Rossby wave timescales cannot match the turbulent timescales implied by $u_{\rm t}$. Note that this would not preclude the formation of the mid-latitude zonal jets observed by Maximenko et al. (2005)

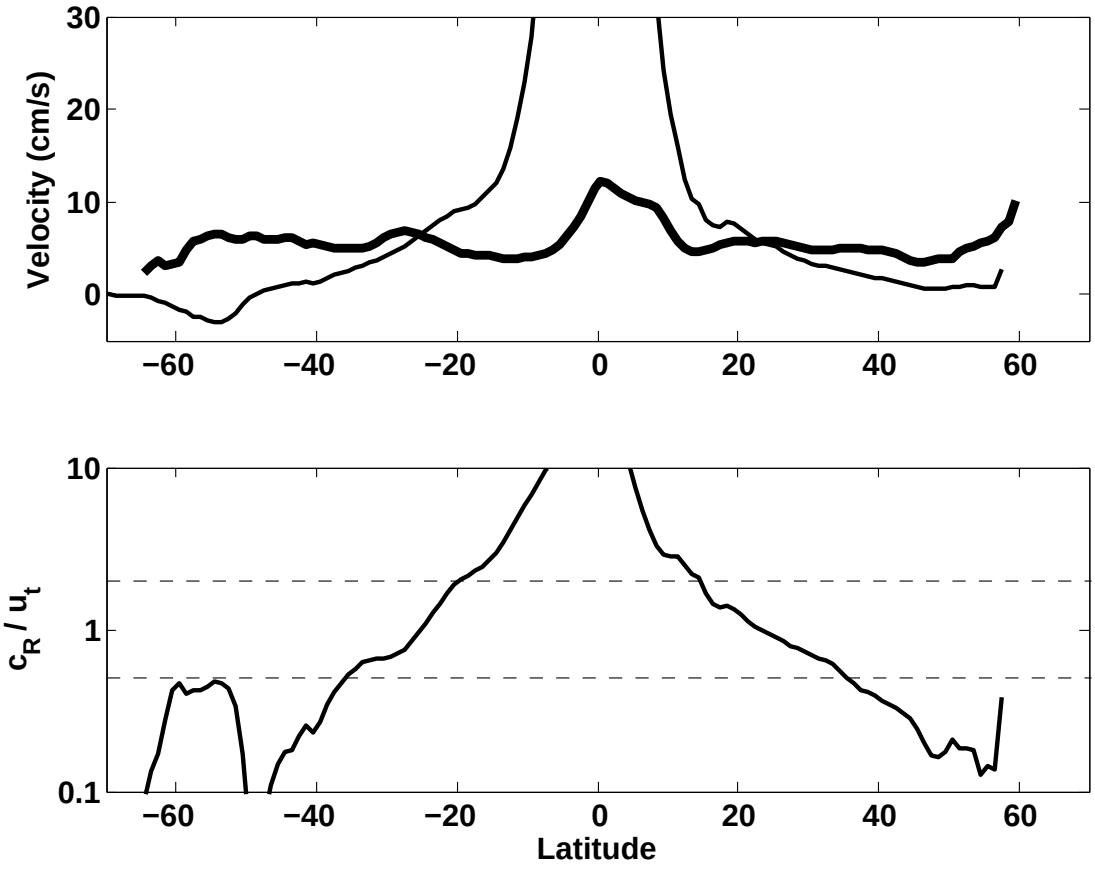

Figure 5.8: Top: Doppler shifted long-wave phase speed (thin black line), versus the root mean square of the eddy velocity u_{t} (thick gray line) from Maximenko's drifter data. It has been assumed that the eddy velocity is entirely in the first baroclinic mode. Bottom: The ratio $c_{\mathrm{R}}/u_{\mathrm{t}}$ with dashed curves at ratios 1/2 and 2.

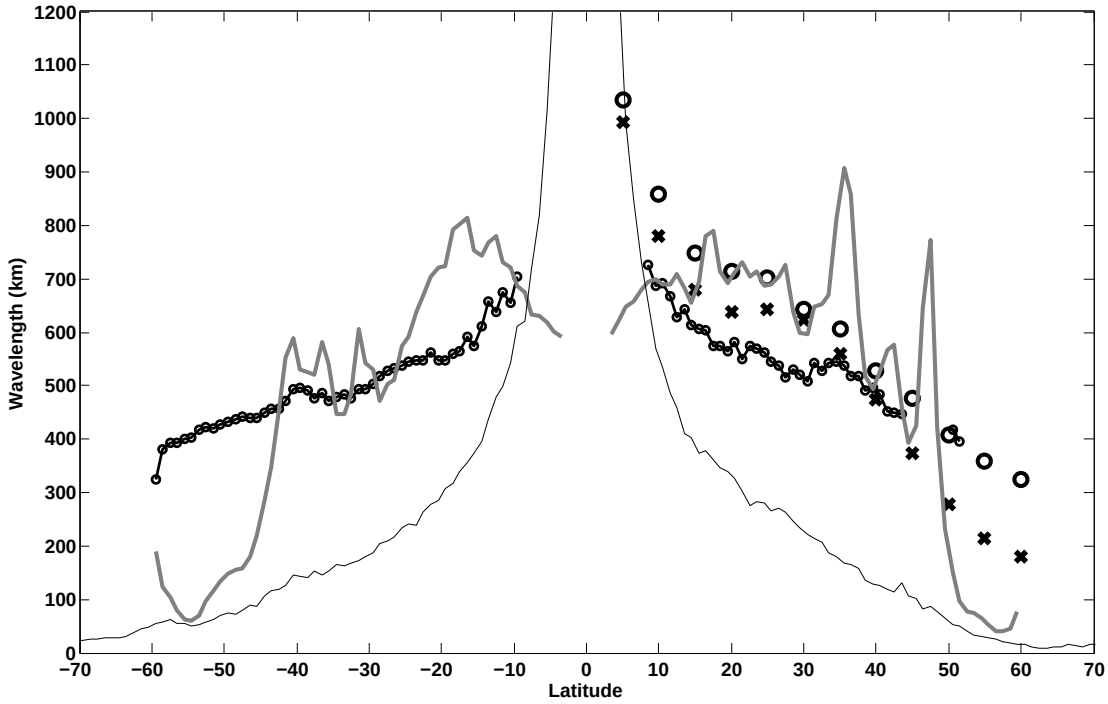

Figure 5.9: Comparison of fitted wavelengths over the global ocean (gray curve, taken from the bottom-right of Figure 5.4) with Eden's observed (black o's) and simulated (black x's) wavelengths, Chelton's observed wavelengths (black circles with solid line) and the deformation wavelength (thin black line).

and Richards et al. (2006): since barotropic Rossby waves are possible, turbulent energy can still accumulate around the dumbbell of Vallis and Maltrud (1993).

Finally we return to a consideration of the spatial scales obtained by fitting linear Rossby wave theory to observed phase speeds, as in Figure 5.4. A global zonal average of the fitted wavelengths is plotted against latitude in Figure 5.9. Also plotted are both observed (black o's) and simulated (black x's) eddy wavelengths in the North Atlantic from Eden (2007), as well as globally observed wavelengths (small circles with line) from Chelton et al. (2007)[8]. The deformation wavelength (thin black line) is also plotted for reference. At low latitudes all of the scales are

[8]Chelton provides eddy diameters, and here these are multiplied by π to give wavelengths.

in close agreement, while the fitted wavelength diverges from the observed eddy scales at latitudes poleward of about $\pm 30°$. This is also the latitude where Eden's scales transition from a flatter Rhines scaling to a steeper deformation scaling. In the Southern Ocean there is a transition from westward propagation to eastward propagation upon entering the ACC region. Finally we note that, in contrast to Eden (2007), Chelton's data do not exhibit a clear transitional latitude between Rhines scaling and deformation scaling. The reasons for this remain unclear.

5.5 Conclusions

We have revisited the interpretation of altimetric phase speed signals in terms of linear Rossby wave theory. Given observations of the interior $\mathbf{u}$ and ∇Q fields (courtesy of Forget, 2008), and assuming quasi-geostrophic theory, we adjusted the lateral scale of linear waves to best fit altimetric observations of westward phase propagation. We find that the implied scales have a well-defined meridional structure. In low latitudes the waves have a scale of 600 km or so, broadly consistent with an appropriately defined Rhines scale. In high latitudes it is more difficult to fit linear theory to the observations, but our attempts to do so imply a scale that is much smaller than in the tropics, closer to the local Rossby deformation scale. There is a rather abrupt transition from low-latitude to high-latitude scaling at $\pm 30°$. These results are broadly consistent with observed and modeled eddy scales, as reported in Eden (2007).

We put forward an interpretation of the reported results in terms of the interaction between turbulence and waves. Over vast regions of the ocean, at scales on or close to the Rossby deformation scale, baroclinic instability converts available

potential energy to kinetic energy of turbulent geostrophic motion. Non-linear interactions result in an upscale energy transfer. At low latitudes, where we observe that $u_{\rm t} < |c_{\rm R}|$, turbulent energy cascades upscale from below readily excites Rossby waves. At higher latitudes, where $u_{\rm t} > |c_{\rm R}|$, turbulence cannot readily excite waves because of the weak overlap in timescales between turbulence and waves. Making use of surface drifter observations, we estimate that the latitude at which waves give way to turbulence coincides with that at which $u_{\rm t} \sim |c_{\rm R}|$, and is found to be $\pm 30^{\circ}$ or so, roughly consistent with the transition from waves to non-linear eddies recently highlighted by Chelton et al. (2007).

Chapter 6

Conclusion

In this thesis we have attempted to explain mesoscale observations in the atmosphere and ocean that classic GFD theory has so far failed to explain. The goal from the outset was to derive a quasi-geostrophic model that accurately and efficiently captures the interaction between surface QG dynamics and the interior QG dynamics.

We developed a formalism, called surface-modal QG (SMQG), which decomposes the geostrophic streamfunction into components due to surface temperature perturbations at the upper (ψ^T) and lower (ψ^B) boundaries, and potential vorticity perturbations in the interior (ψ^I). SMQG has the advantage that each of the streamfunction components can be independently diagnosed to arbitrary accuracy, via modal inversion relations which are constant in time.

Using the SMQG formalism we demonstrated, in a nonlinear Eady model, that while the typical layered QG formulations contain both surface and interior dynamics, they fail to properly resolve the small scales if the horizontal and vertical resolutions are not matched via the Prandtl ratio, N/f. On the other hand when

the horizontal and vertical resolutions match, the layered formulation converges to the Blumen (1978) model. Similarly, layered and modal linear instabilities converge to each other given sufficient vertical resolution.

Next we applied the SMQG formalism to the atmospheric energy spectrum. We found that truncating the interior vertical structure to just the barotropic and first baroclinic modes (the TMTS model) was sufficient to reproduce much of the Nastrom and Gage (1985) kinetic energy spectrum at the upper boundary of our model. Note however that the TMTS model is an incomplete and idealized model of the atmosphere in many respects. It provides a downscale source of energy near the surface which allows for a small scale $K^{-5/3}$ spectrum, but does not rule other mechanisms, such loss of balance or stratified turbulence, from contributing to the spectrum or dissipating energy at small scales.

Using SMQG we derived a scaling law for the wavenumber K_t at which steep spectrally sloped (K^{-3}) interior dynamics yield to shallow spectrally sloped ($K^{-5/3}$) surface dynamics. We applied our scaling law to mean geostrophic currents derived from a new ocean atlas (Forget, 2008) in order to assess whether the ocean's surface dynamics are dominated by temperature anomalies (surface QG) or potential vorticity anomalies (interior QG). Conventional wisdom suggests that the interior modes, specifically the barotropic and first baroclinic modes, dominate the surface in the mesoscales. However, recent work has challenged this view, arguing that the surface mode dominates the surface dynamics. Our transition scale diagnostic suggests that there is a great deal of variability throughout the World Ocean. The main western boundary currents and much of the ACC appear to be dominated by interior modes, while many other regions contain significant surface mode contributions. Consistent with our transition scale diagnostic, the western

boundary currents and the ACC have instabilities with large growth rates, large horizontal scale, and deep vertical structure. Conversely, away from these regions the instabilities usually have weaker growth rates and smaller scales.

Finally we considered the westward propagation of SSH anomalies as seen by satellite altimetry. We found that this propagation is consistent with linear Rossby wave propagation in low latitudes, but not in high latitudes. In particular, between 40° and 50° neither mean flow nor bottom topographic extensions to the classical QG Rossby wave theory are sufficient to produce waves fast enough to recover the observed phase speed. We concluded that these higher latitudes must reflect turbulence.

Appendix A

Implementation details

A.1 Time stepping and enstrophy filtering

Time stepping in the spectral model is performed via a classic leap-frog scheme with an implicit enstrophy filter applied to damp out small scales. In the case of hyperviscous dissipation of order s, the equations of motion at the bottom, interior and top all have the advective form

$$\frac{\partial \alpha}{\partial t} = -J(\psi, \alpha) + \mathcal{F} - \mathcal{D} + (-1)^{s/2+1}\nu_s \nabla^s \alpha, \tag{A.1}$$

where ν_s is the hyperviscous coefficient which on depends the flow velocity and resolution but is the same for the bottom, interior and top at any given time, and $\mathcal{F}$ and $\mathcal{D}$ are external forcing and dissipation respectively. In spectral space the hyperviscous dissipation is

$$H = (-1)^{s/2+1}\nu_s \nabla^s \rightarrow -\nu_s K^s, \tag{A.2}$$

where $K = |\mathbf{K}|$. The leap-frog scheme advances time via

$$\frac{\alpha^{n+1} - \alpha^{n-1}}{2\delta_t} = R^n + H(K)\alpha^{n+1}, \tag{A.3}$$

where R^n contains the advection, forcing and dissipation terms at time n and δ_t is the time step. Solving for α^{n+1} gives an expression for the filter

$$\alpha^{n+1} = \left(2\delta_t R^n + \alpha^{n-1}\right) F(K), \qquad \text{where} \qquad F(K) = \left(1 + 2\delta_t \nu_s K^s\right)^{-1}. \tag{A.4}$$

The time step is tuned via dt_{tune} such that the Courant number (Courant et al., 1928) is sufficiently small

$$\delta_t = dt_{\text{tune}} \frac{\Delta x}{\max(|u|, |v|)}. \tag{A.5}$$

The viscous coefficient is chosen so that the maximum dissipation is only a function of resolution

$$\nu_s = \frac{FT_{\text{tune}}}{2dt_{\text{tune}}} \frac{\max(|u|, |v|)}{K_{\max}^s}, \tag{A.6}$$

where FT_{tune} is a filter tuning parameter that is chosen such that the filter only significantly impacts the highest resolved wavenumbers. The hyperviscous filter is then

$$F(K) = \left[1 + FT_{\text{tune}} \Delta x \left(\frac{K}{K_{\max}}\right)^s\right]^{-1}, \tag{A.7}$$

so we have $F(0) = 1$ and $F(K_{\max}) = 1/(1 + FT_{\text{tune}}\Delta x)$ which approaches unity as $\Delta x \to 0$.

In all of the simulations presented here, an exponential cutoff filter (Smith, 2004a) was used instead of a hyperviscous filter. The exponential cutoff filter

mimics the hyperviscous filter but is explicitly restricted to act only on $K > K_c \gtrsim 2K_{\max}/3$. The exponential cutoff filter is defined as

$$F_{\text{ec}}(K) = \begin{cases} \left[\frac{1}{1+FT_{\text{tune}}\Delta x}\right]^{\left(\frac{K-K_c}{K_{\max}-K_c}\right)^s} & , \quad K > K_c \\ 1 & , \quad K \leq K_c. \end{cases} \tag{A.8}$$

A.2 Linearization of equations the SMQG equations

Linearization of (2.11) and (2.12) yields a set of $\mathcal{N}+2$ linear differential equations

$$\partial_t \hat{\psi}^T = -i\boldsymbol{K} \cdot \left[\boldsymbol{U}(H)\hat{\psi}^T - \nabla^\perp \Theta^T \hat{\psi}|_{z=z_T} \phi^T(K, z_T)/\phi_z^T(K, z_T)\right], \tag{A.9a}$$

$$\partial_t \hat{\psi}^B = -i\boldsymbol{K} \cdot \left[\boldsymbol{U}(0)\hat{\psi}^B - \left(\nabla^\perp \Theta^B - ir\boldsymbol{K}\right)\hat{\psi}|_{z=z_B} \phi^B(K, z_B)/\phi_z^B(K, z_B)\right], \tag{A.9b}$$

$$\partial_t \hat{\psi}_n = -i\boldsymbol{K} \cdot \left[\frac{\Gamma \boldsymbol{U}^S \langle\hat{\psi}\rangle_n}{K^2+\lambda_n^2} + \sum_m \frac{\langle U\rangle_{mn}(K^2+\lambda_m^2)\hat{\psi}_m - \langle\hat{\psi}\rangle_{mn}\lambda_m^2 \boldsymbol{U}_m}{K^2+\lambda_n^2}\right] + \frac{ik\beta\langle\hat{\psi}\rangle_n}{K^2+\lambda_n^2}, \tag{A.9c}$$

which become an eigenvalue problem once a linear wave of the form $\mathrm{e}^{i\boldsymbol{K}\cdot(\boldsymbol{x}-\boldsymbol{c}t)]}$ is inserted for each modal and surface component of the streamfunction.

A.3 Green's function for the mean fields in the TMTS equations

The mean velocity $U(z)$ must solve

$$\Gamma U \equiv s\frac{d^2U}{dz^2} = \beta - Q_y, \quad U_z(H) = -\Theta_y^T, \quad U_z(0) = -\Theta_y^B, \tag{A.10}$$

and so we seek a Green's function $G(z,\xi)$ that satisfies

$$\Gamma G(z,\xi) = \delta(z-\xi), \quad G_z(H,\xi) = G_z(0,\xi) = 0.$$

There is a function $G(z,\xi)$ that satisfies this problem, but is not a standard Green's function. The generalized Green's function

$$\mathcal{G}(z,\xi) = \begin{cases} -\frac{N^2H}{f^2}\left[\frac{1}{2}(z/H)^2 + \frac{1}{2}(1-(\xi/H))^2 - \frac{1}{6}\right], & z \in (0,\xi) \\ -\frac{N^2H}{f^2}\left[\frac{1}{2}(\xi/H)^2 + \frac{1}{2}(1-(z/H))^2 - \frac{1}{6}\right], & z \in (\xi,H). \end{cases}$$

yields a solution for $U(z)$ that is augmented by an arbitrary constant, C:

$$\begin{aligned} U(z) &= \int_0^H \mathcal{G}(z,\xi)[\beta - Q_y(\xi)]\, d\xi + s\mathcal{G}(z,H)\Theta_y^T - s\mathcal{G}(z,0)\Theta_y^B + C \\ &= \int_0^H \mathcal{G}(z,\xi)w(\xi)\, d\xi + C \end{aligned} \tag{A.11}$$

where w is the standardizing function

$$w(z) = \beta - Q_y(z) + s\Theta_y^B\delta(z) - s\Theta_y^T\delta(z-H)$$

which must satisfy $\int_0^H w(z)\,dz = 0$ (Butkovskii, 1982, pg. 30). Using the expansion $U(z) = U^{\rm bc}\phi(z) + U^S(z)$, and equations (3.1) and (A.10),

$$\beta - Q_y(z) = -\lambda^2 U^{\rm bc}\phi(z) + \Gamma U^S.$$

Using this expression in (A.11), a few lines of computation reveals that

$$-\int_0^H \mathcal{G}(z,\xi)\Gamma U^{\rm I}\,d\xi = -U^{\rm bc}\int_0^H \mathcal{G}(z,\xi)\Gamma\phi(\xi)\,d\xi = U^{\rm bc}\phi(z),$$

as it should, and

$$U^S(z) = \int_0^H \mathcal{G}(z,\xi)\Gamma U^S\,d\xi + s\mathcal{G}(z,H)\Theta_y^B - s\mathcal{G}(z,0)\Theta_y^B + C.$$

Demanding that $\Gamma U^S = \text{const}$, $\langle w\rangle = 0$ and $\langle U^S\rangle = 0$ then yields $C = 0$ and the form stated in (3.6) follows (note that $\int_0^H G(z,\xi)\,d\xi = 0$).

A.4 Details of the TMTS equations

In forming the barotropic and baroclinic modal Eqs. (3.8c) and (3.8d), interaction coefficients between the vertical structure functions ϕ arise. Using the expressions for $\phi^{\rm t,b}$ in (3.3) we have

$$\langle\phi^{\rm t}\rangle = \langle\phi^{\rm b}\rangle = \frac{1}{H}\int_0^H \frac{\cosh(\mu z/H)}{\cosh\mu}dz = \mu^{-1}\tanh\mu.$$

Notice that because the surface modes have both vertical and horizontal dependence, the interaction terms involving surface functions are functions of μ. We can form the other interaction terms using $\phi(z)$ from (3.2), and computing the

integrals:

$$\langle\phi\phi^{\rm t}\rangle = -\langle\phi\phi^{\rm b}\rangle = \frac{1}{H}\int_0^H \sqrt{2}\cos(\pi z/H)\frac{\cosh(\mu z/H)}{\cosh\mu}dz = -\frac{\sqrt{2}\,\mu}{\mu^2+\pi^2}\ \tanh\mu,$$
$$\langle\phi\phi\phi^{\rm t}\rangle = \langle\phi\phi\phi^{\rm b}\rangle = \frac{1}{H}\int_0^H 2\cos^2(\pi z/H)\frac{\cosh(\mu z/H)}{\cosh\mu}dz = \frac{2}{\mu}\frac{\mu^2+2\pi^2}{\mu^2+4\pi^2}\ \tanh\mu.$$

Since $\hat{\psi}(z) = \hat{\psi}^{\rm bt} + \phi(z)\hat{\psi}^{\rm bc} + \phi^{\rm t}(z)\hat{\psi}^{\rm t} + \phi^{\rm b}(z)\hat{\psi}^{\rm b}$ the barotropic projection is simply the vertical average

$$\langle\hat{\psi}\rangle = \hat{\psi}^{\rm bt} + \langle\phi^{\rm t}\rangle\hat{\psi}^{\rm t} + \langle\phi^{\rm b}\rangle\hat{\psi}^{\rm b}.$$

where the baroclinic term has vanished since $\langle\phi\rangle = 0$. Summarizing, the projections of the total streamfunction onto various internal modes are

$$\langle\hat{\psi}\rangle = \hat{\psi}^{\rm bt} + \gamma_0\ \left(\hat{\psi}^{\rm t} + \hat{\psi}^{\rm b}\right), \qquad \gamma_0 \equiv \mu^{-1}\tanh\mu$$
$$\langle\phi\hat{\psi}\rangle = \hat{\psi}^{\rm bc} - \gamma_1\ \left(\hat{\psi}^{\rm t} - \hat{\psi}^{\rm b}\right), \qquad \gamma_1 \equiv \frac{\sqrt{2}\,\mu}{\mu^2+\pi^2}\ \tanh\mu$$
$$\langle\phi\phi\hat{\psi}\rangle = \hat{\psi}^{\rm bt} + \gamma_2\ \left(\hat{\psi}^{\rm t} + \hat{\psi}^{\rm b}\right), \qquad \gamma_2 \equiv \frac{2}{\mu}\frac{\mu^2+2\pi^2}{\mu^2+4\pi^2}\ \tanh\mu.$$

We must also compute interactions between the mean shear components and vertical mode structures. Interactions between the baroclinic mode ϕ and the surface shear (3.6) are given by

$$\langle\phi U^S\rangle = \frac{1}{H}\int_0^H \sqrt{2}\cos(\pi z/H)U^S(z)dz = \frac{\sqrt{2}H}{\pi^2}(\Theta_y^{\rm t} + \Theta_y^{\rm b}),$$
$$\langle\phi\phi U^S\rangle = \frac{1}{H}\int_0^H 2\cos^2(\pi z/H)U^S(z)dz = -\frac{H}{4\pi^2}(\Theta_y^{\rm t} - \Theta_y^{\rm b}).$$

The projections of the mean velocity that appear in (3.8) are then

$$\langle \phi U \rangle = U^{\rm bc} + \frac{\sqrt{2}H}{\pi^2}(\Theta_y^{\rm t} + \Theta_y^{\rm b})$$
$$\langle \phi\phi U \rangle = -\frac{H}{4\pi^2}(\Theta_y^{\rm t} - \Theta_y^{\rm b}).$$

A.5 Linearization of the TMTS equations

The linear instability calculation is performed by linearizing the TMTS equations as follows. Neglecting the nonlinear terms in (3.8), assuming a wave solution

$$(\hat{\psi}^{\rm t}, \hat{\psi}^{\rm b}, \hat{\psi}^{\rm bt}, \hat{\psi}^{\rm bc}) = \mathfrak{Re}(\hat{\varphi}^{\rm t}, \hat{\varphi}^{\rm b}, \hat{\varphi}^{\rm bt}, \hat{\varphi}^{\rm bc})\mathrm{e}^{-i\omega t},$$

and considering only zonal wave instabilities ($\ell = 0$), so that the phase speed is $c = \omega/k$, we obtain

$$\begin{aligned}
c\hat{\varphi}^{\rm t} &= U(H)\hat{\varphi}^{\rm t} + H\Theta_y^T(\mu\tanh\mu)^{-1}(\hat{\varphi}^{\rm bt} - \sqrt{2}\hat{\varphi}^{\rm bc} + \hat{\varphi}^{\rm t} + \hat{\varphi}^{\rm b}\mathrm{sech}\,\mu)\\
c\hat{\varphi}^{\rm b} &= U(0)\hat{\varphi}^{\rm b} - H\left(\Theta_y^B + ir\frac{K^2}{k}\right)(\mu\tanh\mu)^{-1}(\hat{\varphi}^{\rm bt} + \sqrt{2}\hat{\varphi}^{\rm bc} + \hat{\varphi}^{\rm t}\mathrm{sech}\,\mu + \hat{\varphi}^{\rm b})\\
c\hat{\varphi}^{\rm bt} &= \langle\phi U\rangle\mu^{-2}(\mu^2+\pi^2)\hat{\varphi}^{\rm bc} - (\beta - \Gamma U^S)K^{-2}\left[\hat{\varphi}^{\rm bt} + \gamma_0(\hat{\varphi}^{\rm t} + \hat{\varphi}^{\rm b})\right]\\
&\quad - U^{\rm bc}\lambda^2K^{-2}\left[\hat{\varphi}^{\rm bc} - \gamma_1(\hat{\varphi}^{\rm t} - \hat{\varphi}^{\rm b})\right]\\
c\hat{\varphi}^{\rm bc} &= \langle\phi U\rangle\mu^2(\mu^2+\pi^2)^{-1}\ \hat{\varphi}^{\rm bt} + \langle\phi\phi U\rangle\hat{\varphi}^{\rm bc}\\
&\quad - (\beta - \Gamma U^S)K^{-2}\mu^2(\mu^2+\pi^2)^{-1}\left[\hat{\varphi}^{\rm bc} - \gamma_1(\hat{\varphi}^{\rm t} - \hat{\varphi}^{\rm b})\right]\\
&\quad - U^{\rm bc}\lambda^2K^{-2}\mu^2(\mu^2+\pi^2)^{-1}\left[\hat{\varphi}^{\rm bt} + \gamma_2(\hat{\varphi}^{\rm t} + \hat{\varphi}^{\rm b})\right].
\end{aligned}$$

which is a 4×4 eigenvalue problem with $(\hat{\varphi}^{\rm t}, \hat{\varphi}^{\rm b}, \hat{\varphi}^{\rm bt}, \hat{\varphi}^{\rm bc})$ the eigenvector and the phase speed c the eigenvalue.

A.6 Surface modes with exponential stratification

With exponential stratification of the form

$$N^2(z) = \frac{\exp(z/\delta_c)}{\delta_c F}$$

on $z \in [-1, 0]$ the surface modes in (2.8) and (2.9) are given by

$$\phi^T(K,z) = \exp(z/2\delta_c)\frac{K_0(\Upsilon_{-1})I_1(\Upsilon_z) + I_0(\Upsilon_{-1})K_1(\Upsilon_z)}{I_0(\Upsilon_{-1})K_1(2\delta_c\mu_e) + I_1(2\delta_c\mu_e)K_0(\Upsilon_{-1})}$$

and

$$\phi^B(K,z) = \exp((1+z)/2\delta_c)\frac{K_0(2\delta_c\mu_e)I_1(\Upsilon_z) + I_0(2\delta_c\mu_e)K_1(\Upsilon_z)}{I_0(2\delta_c\mu_e)K_1(\Upsilon_{-1}) + I_1(\Upsilon_{-1})K_0(2\delta_c\mu_e)},$$

where K_0, K_1, I_0 and I_1 are modified Bessel functions and $\mu_e = K/\sqrt{\delta_c F}$, $\Upsilon_z = 2\delta_c\mu_e \exp(z/2\delta_c)$, and $\Upsilon_{-1} = 2\delta_c\mu_e \exp(-1/2\delta_c)$. Therefore the surface-modal gradients used to invert the surface streamfunctions are

$$\bar{\phi}^T(K,0) = \left.\frac{d\phi^T}{dz}\right|_0 = \mu_e \frac{I_0(2\delta_c\mu_e)K_0(\Upsilon_{-1}) - I_0(\Upsilon_{-1})K_0(2\delta_c\mu_e)}{K_0(\Upsilon_{-1})I_1(2\delta_c\mu_e) + I_0(\Upsilon_{-1})K_1(2\delta_c\mu_e)}$$

and

$$\bar{\phi}^B(K,-1) = \left.\frac{d\phi^B}{dz}\right|_{-1} = -\mu_e \exp(-1/2\delta_c)\frac{I_0(2\delta_c\mu_e)K_0(\Upsilon_{-1}) - I_0(\Upsilon_{-1})K_0(2\delta_c\mu_e)}{K_0(2\delta_c\mu_e)I_1(\Upsilon_{-1}) + I_0(2\delta_c\mu_e)K_0(\Upsilon_{-1})}.$$

A.7 Mean State Calculation from the Forget Atlas and Discretization of Linear Problem

The Forget (2008) ocean atlas contains up to 50 layers (of thicknesses Δ_j) of potential temperature and salinity data at each (lat, lon) coordinate. We first compute annually averaged global potential temperature and salinity fields, and from these compute a neutral density field $\overline{\rho}$ using locally referenced pressure. Thermal wind balance is then used to compute the mean velocity field $\mathbf{U}$, assuming a level of no motion at the bottom of the ocean (see the appendix of Smith, 2007, for details). We define the top 5 layers, which are each 10 m thick, as a mixed layer of depth $h \equiv 50$ m. The mean buoyancy gradients $\nabla B = -(g/\rho_0)\nabla\overline{\rho}$ at the surface are averaged over the defined mixed layer, and then related to vertical shears via thermal wind

$$U_z(z_0) = -\frac{1}{fh}\int_{-h}^{0} B_y \, dz, \quad V_z(z_0) = \frac{1}{fh}\int_{-h}^{0} B_x \, dz.$$

The surface velocities themselves are obtained by averaging the velocities from the ocean atlas over h, viz.

$$U(z_0) = \frac{1}{h}\int_{-h}^{0} U \, dz, \quad V(z_0) = \frac{1}{h}\int_{-h}^{0} V \, dz. \tag{A.13}$$

The linear problem is discretized, at each lateral location, onto the N_z discrete depths z_j of the data computed from the Forget atlas. The discrete surface buoyancy is given by

$$\hat{b}_m(z_0) = f\frac{\hat{\psi}_m(z_0) - \hat{\psi}_m(z_1)}{\Delta_0}.$$

and the discrete PV is

$$\hat{q}_m(z_j) = \frac{f^2}{\Delta_j}\left[\frac{\hat{\psi}_m(z_{j-1}) - \hat{\psi}_m(z_j)}{B(z_{j-1}) - B(z_j)} - \frac{\hat{\psi}_m(z_j) - \hat{\psi}_m(z_{j+1})}{B(z_j) - B(z_{j+1})}\right] - K^2\hat{\psi}_m(z_j),\ \ j = 1..N_z{-}1.$$

The mean QGPV gradients $Q_x(z_j)$ and $Q_y(z_j)$ are given by (5.2), using the same vertical discretization, and simple horizontal finite differences to compute x and y derivatives. At the bottom, $\hat{q}_m(z_{N_z}) = \hat{\psi}_m(z_{N_z}) = 0$. The discrete version of (5.4) is then solved as a single matrix eigenvalue problem, using Matlab.

Following Smith (2007), bottom topography is added using the Smith and Sandwell (1997) global seafloor topography dataset. At each latitude, longitude location in the calculation we linearly regress a best fit plane of the form $\eta(x, y) = \eta_0 + \alpha^x x + \alpha^y y$ using the surrounding $2^\circ \times 2^\circ$ section of topography. The slopes α^x and α^y are then added to the bottom (layer $\mathcal{N}$) QGPV gradient as

$$\nabla Q^{\text{topo}} = \frac{f}{\Delta_{\mathcal{N}}}\left(\alpha^x \hat{\mathbf{x}} + \alpha^y \hat{\mathbf{y}}\right).$$

References

Arbic, B. K. and G. R. Flierl, 2004: Baroclinically unstable geostrophic turbulence in the limits of strong and weak bottom ekman friction: Application to midocean eddies. *J. Phys. Oceanogr.*, **34**, 2257–2273.

Arbic, B. K. and R. B. Scott, 2008: On quadratic bottom drag, geostrophic turbulence, and oceanic mesoscale eddies. *J. Phys. Oceanogr.*, **38**, 84–103.

Barnier, B., B. L. Hua, and C. L. Provost, 1991: On the catalytic role of high baroclinic modes in eddy-driven large-scale circulations. *J. Phys. Oceanogr.*, **21**, 976–997.

Blumen, W., 1978: Uniform potential vorticity flow: Part I. Theory of wave interactions and two-dimensional turbulence. *J. Atmos. Sci.*, **35**, 774–783.

Bretherton, F. P., 1966: Critical layer instability in baroclinic flows. *Quart. J. Roy. Meteor. Soc.*, **92**, 325–334.

Butkovskii, A. G., 1982: *Green's functions and transfer functions handbook*. Halsted Press, New York.

Capet, X., P. Klein, B. L. Hua, G. Lapeyre, and J. C. McWilliams, 2008: Surface

kinetic energy transfer in surface quasi-geostrophic flows. *J. Fluid Mech.*, **604**, 165–174.

Cessi, P. and F. Primeau, 2001: Dissipative selection of low-frequency modes in a reduced gravity basin. *J. Phys. Oceanogr.*, **31**, 127–137.

Charney, J., 1947: Dynamics of long waves in a baroclinic westerly current. *J. Meteor.*, **4**, 135–162.

— 1948: On the scale of atmospheric motions. *Geophys. Publ. Oslo*, **17**, 1–17.

Charney, J. G., 1971: Geostrophic turbulence. *J. Atmos. Sci.*, **28**, 1087–1095.

— 1973: Planetary fluid dynamics. *Dynamic Meteorology*, P. Morel, ed., D. Rediel, 97–351.

Charney, J. G. and M. E. Stern, 1962: On the stability of internal baroclinic jets in a rotating atmosphere. *J. Atmos. Sci.*, **19**, 159–172.

Chelton, D. B., R. A. deSzoeke, M. G. Schlax, K. E. Naggar, and N. Siwertz, 1998: Geographical variability of the first baroclinic Rossby radius of deformation. *J. Phys. Oceanogr.*, **28**, 433–460.

Chelton, D. B. and M. G. Schlax, 1996: Global observations of oceanic Rossby waves. *Science*, **272**, 234–238.

Chelton, D. B., M. G. Schlax, R. M. Samelson, and R. A. de Szoeke, 2007: Global observations of westward energy propagation in the ocean: Rossby waves or nonlinear eddies? *Geophys. Res. Lett.*, **34**, L15,606.

Cho, J. Y. N. and E. Lindborg, 2001: Horizontal velocity structure functions in the upper troposphere and lower stratosphere 1. observations. *J. Geophys. Res.*, **106**, 10223–10232.

Cho, J. Y. N., R. E. Newell, and J. D. Barrick, 1999: Horizontal wavenumber spectra of winds, temperature, and trace gases during the pacific exploratory missions. Part II: Gravity waves, quasi-two-dimenaional turublence, and vertical modes. *J. Geophys. Res.*, **104**, 16297–16308.

Colin de Verdière, A. and R. Tailleux, 2005: The interaction of a baroclinic mean flow with long Rossby waves. *J. Phys. Oceanogr.*, **35**, 865–879.

Constantin, P., A. J. Majda, and E. Tabak, 1994: Formation of strong fronts in the 2-d quasigeostrophic thermal active scalar. *Nonlinearity*, **7**, 1495–1533.

Courant, R., K. Friedrichs, and H. Lewy, 1928: Über die partiellen deifferenzengleichungen der mathematischen physik. *Mathematische Annalen*, **100**, 32–74.

Davies, H. C. and C. H. Bishop, 1994: Eady edge waves and rapid development. *J. Atmos. Sci.*, **51**, 1930–1946.

Dewan, E. M., 1979: Stratospheric wave spectra resembling turbulence. *Science*, **204**, 832–835.

— 1997: Saturated-cascade similtude theory of gravity wave spectra. *JGR*, **102**, 29799–29817.

Dewar, W. K., 1998: On "too fast" baroclinic planetary waves in the general circulation. *J. Phys. Oceanogr.*, **28**, 500–511.

Dewar, W. K. and M. Y. Morris, 2000: On the propagation of baroclinic waves in the general circulation. *J. Phys. Oceanogr.*, **30**, 2637–2649.

Eady, E. T., 1949: Long waves and cyclone waves. *Tellus*, **1**, 33–52.

Eden, C., 2007: Eddy length scales in the North Atlantic Ocean. *J. Geophys. Res.*, **112**, C06,004.

Ertel, H., 1942: Ein neuer hydrodynamischer erhaltungssgatz. *Die Naturwissenschaften*, **30**, 543–544.

Ertel, H. and C.-G. Rossby, 1949: A new conservation theorem of hydrodynamics. *Geofisica Pura e Appl.*, **14**, 189–193.

Flierl, G. R., 1978: Models of vertical structure and the calibration of two-layer models. *Dyn. Atmos. Oceans*, **2**, 341–381.

Forget, G., 2008: Mapping observations in a dynamical framework: A 2004-2006 ocean atlas. *Submitted to* J. Phys. Oceanogr..

Fox-Kemper, B., R. Ferrari, and R. Hallberg, 2008: Parameterization of mixed layer eddies. Part I: Theory and diagnosis. *J. Phys. Oceanogr.*, **38**, 1145–1165.

Fox-Rabinovitz, M. and R. S. Lindzen, 1993: Numerical experiments on consistent horizontal and vertical resolution for atmospheric models and observing systems. *Mon. Wea. Rev.*, **121**, 264–271.

Fu, L. L. and G. R. Flierl, 1980: Nonlinear energy and enstrophy transfers in a realistically stratified ocean. *Dyn. Atmos. Oceans*, **4**, 219–246.

Gao, X. and J. W. Meriwether, 1998: Mesoscale spectral analysis of in situ horizontal and vertical wind measurements at 6km. *J. Geophys. Res.*, **103**, 6397–6404.

Gill, A. E., J. S. A. Green, and A. J. Simmons, 1974: Energy partition in the large-scale ocean circulation and the production of mid-ocean eddies. *Deep-Sea Res.*, **21**, 499–528.

Gkioulekas, E. and K. Tung, 2007a: Is the subdominant part of the energy spectrum due to downscale energy cascade hidden in quasi-geostrophic turbulence? *Discret. Contin. Dyn. Syst. Ser. B.*, **7**, 293–314.

— 2007b: A new proof on net upscale energy cascade in 2d and qg turbulence. *JFM*, **576**, 173–189.

Green, J. S. A., 1960: A problem in baroclinic instability. *Quart. J. Roy. Meteor. Soc.*, **86**, 237–251.

Grianik, N., I. M. Held, K. S. Smith, and G. K. Vallis, 2004: The effects of quadratic drag on the inverse cascade of two-dimensional turbulence. *Phys. Fluids*, **16**, 1–16.

Hamilton, K., Y. O. Takahashi, and W. Ohfuchi, 2008: The mesoscale spectrum of atmospheric motions investigated in a very fine resolution global general circulation model. *J. Geophys. Res.*, doi:10.1029/2008JD009785.

Hart, J. E., 1979: Finite amplitude baroclinic instability. *Annu. Rev. Fluid Mech.*, **11**, 147–172.

Heifetz, E., J. Methven, B. J. Hoskins, and C. H. Bishop, 2004: The counter-propagating Rossby-wave perspective on baroclinic instability. II: Application to the Charney model. *Quart. J. Roy. Meteor. Soc.*, **130**, 233–258.

Held, I. M., R. T. Pierrehumbert, S. T. Garner, and K. L. Swanson, 1995: Surface quasi-geostrophic dynamics. *J. Fluid. Mech.*, **282**, 1–20.

Hoskins, B. J., M. E. McIntyre, and A. W. Robertson, 1985: On the use and significance of isentropic potential vorticity maps. *Quart. J. Roy. Meteor. Soc.*, **111**, 877–946.

Hua, B. L. and D. B. Haidvogel, 1986: Numerical simulations of the vertical structure of quasi-geostrophic turbulence. *J. Atmos. Sci.*, **43**, 2923–2936.

Juckes, M. N., 1994: Quasigeostrophic dynamics of the tropopause. *J. Atmos. Sci.*, **51**, 2756–2768.

Killworth, P. D. and J. R. Blundell, 1999: The effect of bottom topography on the speed of long extratropical planetary waves. *J. Phys. Oceanogr.*, **29**, 2689–2710.

— 2003: Long extratropical planetary wave propagation in the presence of slowly varying mean flow and bottom topography. Part I: The local problem. *J. Phys. Oceanogr.*, **33**, 784–801.

— 2005: The dispersion relation of planetary waves in the presence of mean flow and topography. part ii: Two-dimensional examples and global results. *J. Phys. Oceanogr.*, **35**, 2110–2133.

— 2007: Planetary wave response to surface forcing and to instability in the presence of mean flow and topography. *J. Phys. Oceanogr.*, **35**, 2110–2133.

Killworth, P. D., D. B. Chelton, and R. A. D. Szoeke, 1997: The speed of observed and theoretical long extratropical planetary waves. *J. Phys. Oceanogr.*, **29**, 1946–1966.

Kitamura, Y. and Y. Matsuda, 2006: The k_h^{-3} and $k_h^{-5/3}$ energy spectra in stratified turbulence. *Geophys. Res. Lett.*, **33**, L05809.

Klein, P., B. L. Hua, G. Lapeyre, X. Capet, S. L. Gentil, and H. Sasaki, 2008: Upper ocean turbulence from high-resolution 3d simulations. *J. Phys. Oceanogr.*, **38**, 1748–1763.

Koshyk, J. and K. P. Hamilton, 2001: The horizontal kinetic energy spectrum and spectral budget simulated by a high-resolution troposphere-stratosphere-mesosphere gcm. *J. Atmos. Sci.*, **58**, 329–348.

Koshyk, J. N., K. P. Hamilton, and J. D. Mahlman, 1999: Simulation of $k^{-5/3}$ mesoscale spectral regime in the GFDL SKYHI general circulation model. *Geophys. Res. Lett.*, **26**, 843–946.

Kraichnan, R., 1967: Inertial ranges in two-dimensional turbulence. *Phys. Fluids*, **10**, 1417–1423.

— 1971: Inertial-range in two- and three-dimensional turbulence. *J. Fluid Mech.*, **47**, 525–535.

LaCasce, J. H. and J. Pedlosky, 2004: The instability of Rossby basin modes and the oceanic eddy field. *J. Phys. Oceanogr.*, **34**, 2027–2041.

Lapeyre, G., 2008: What mesoscale signal does the altimeter reflect? on the decomposition in baroclinic modes and on a surface-trapped mode. *Submitted to* J. Phys. Oceanogr..

Lapeyre, G. and P. Klein, 2006: Dynamics of the upper oceanic layers in terms of surface quasigeostrophy theory. *J. Phys. Oceanogr.*, **36**, 165–176.

Le Traon, P. Y., 1993: Comments on "Mesoscale variability in the Atlantic Ocean from Geosat altimetry and WOCE high resolution numerical modeling". *J. Phys. Oceanogr.*, **23**, 2729–2732.

Le Traon, P. Y., P. Klein, B. L. Hua, and G. Dibaroure, 2008: Do altimeter wavenumber spectra agree with the interior or surface quasigeostrophic theory? *J. Phys. Oceanogr.*, **38**, 1137–1142.

Lilly, D. K., 1989: Two-dimensional turbulence generated by energy sources at two scales. *J. Atmos. Sci.*, **45**, 2026–2030.

Lindborg, E., 1999: Can the atmospheric kinetic energy spectrum be explained by two-dimensional turbulence? *J. Fluid Mech.*, **388**, 259–288.

— 2005: The effect of rotation on the mesoscale energy cascade in the free atmosphere. *Geophys. Res. Lett.*, **32**, L01809.

— 2007: Horizontal wavenumber spectra of vertical vorticity and horizontal divergence in the upper troposphere and lower stratosphere. *J. Atmos. Sci.*, **64**, 1017–1025.

Lindzen, R., 1994: The Eady problem with zero pv gradient but beta unequal to zero. *J. Atmos. Sci.*, **51**, 3221–3226.

Lindzen, R. S. and M. Fox-Rabinovitz, 1989: Consistent horizontal and vertical resolution. *Mon. Wea. Rev.*, **117**, 2575–2583.

Lorenz, E. N., 1955: Available potential energy and the maintenance of the General Circulation. *Tellus*, **7**, 157–167.

Maharaj, A. M., P. Cipollini, N. J. Holbrook, P. D. Killworth, and J. R. Blundell, 2007: An evaluation of the classical and extended Rossby wave theories in explaining spectral estimates of the first few baroclinic modes in the South Pacific Ocean. *Ocean Dynamics*, **57**, 173–187.

Marenco, A., V. Thouret, P. Nédélec, H. Smith, M. Helten, D. Kley, F. Karcher, P. Simon, K. Law, J. Pyle, G. Poschmann, R. V. Wrede, C. Hume, and T. Cook, 1998: Measurement of ozone and water vapor by airbus in-service aircraft: the mozaic airborne program, an overview. *J. Geophys. Res.*, **103**, 25631–25642.

Maximenko, N. A., B. Bang, and H. Sasaki, 2005: Observational evidence of alternative zonal jets in the world ocean. *Geophys. Res. Lett.*, **32**, L12607:1–4.

McKiver, W. J. and D. G. Dritschel, 2008: Balance in non-hydrostatic rotating stratified turbulence. *J. Fluid Mech.*, **596**, 201–219.

Muraki, D. J. and C. Snyder, 2007: Vortex dipoles for surface quasigeostrophic models. *J. Atmos. Sci.*, **64**, 2961–2967.

Muraki, D. J., C. Snyder, and R. Rotunno, 1999: The next-order corrections to quasigeostrophic theory. *J. Atmos. Sci.*, **56**, 1547–1560.

Nastrom, G. D. and K. S. Gage, 1985: A climatology of atmospheric wavenumber spectra of wind and temperature observed by comercial aircraft. *J. Atmos. Sci.*, **42**, 950–960.

Orszag, S. A., 1971: Numerical simulation of incompressible flows within simple boundaries: Accuracy. *J. Fluid Mech.*, **146**, 21–43.

Pedlosky, J., 1964: The stability of currents in the atmosphere and ocean. Part I. *J. Atmos. Sci.*, **21**, 201–219.

— 1984: The equations for geostrophic motion in the ocean. *J. Phys. Oceanogr.*, **14**, 448–455.

— 1987: *Geophysical Fluid Dynamics*. Springer, New York, 2nd edition, 710 pp.

Phillips, N. A., 1951: A simple three-dimensional model for the study of large-scale extratropical flow patterns. *J. Meteor.*, **8**, 381–394.

Rhines, P. B., 1975: Waves and turbulence on a β-plane. *J. Fluid. Mech.*, **69**, 417–443.

Richards, K. J., N. A. Maximenko, F. O. Bryan, and H. Sasaki, 2006: Zonal jets in the Pacific Ocean. *Geophys. Res. Lett.*, **33**, L03605.

Schlösser, F. and C. Eden, 2007: Diagnosing the energy cascade in a model of the north atlantic. *Geophys. Res. Lett.*, **34**, L02604.

Scott, R. B. and B. K. Arbic, 2007: Spectral energy fluxes in geostrophic turbulence: Implications for ocean energetics. *J. Phys. Oceanogr.*, **37**, 673–688.

Scott, R. B. and F. Wang, 2005: Direct evidence of an oceanic inverse kinetic energy cascade from satellite altimetry. *J. Phys. Oceanogr.*, **35**, 1650–1666.

Scott, R. K. and L. M. Polvani, 2007: Forced-dissipative shallow-water turbulence on the sphere and the atmospheric circulation of the giant planets. *J. Atmos. Sci.*, **64**, 3158–3176.

Skamarock, W. C., 2004: Evaluating mesoscale NWP models using kinetic energy spectra. *Mon. Wea. Rev.*, **132**, 3019–3032.

Skamarock, W. C. and J. B. Klemp, 2008: A time-split nonhydrostatic atmospheric model for weather research and forecasting applications. *J. Comput. Phys.*, **227**, 3465–3485.

Smith, K. S., 2004a: Comments on "The k^{-3} and $k^{-5/3}$ energy spectrum of atmospheric turbulence: Quasigeostrophic two-level model simulation". *J. Atmos. Sci.*, **61**, 937–942.

— 2004b: A local model for planetary atmospheres forced by small-scale convection. *J. Atmos. Sci.*, **61**, 1420–1433.

— 2007: The geography of linear baroclinic instability in earth's oceans. *J. Marine Res.*, **65**, 655–683.

Smith, K. S. and J. C. Marshall, 2008: Evidence for deep eddy mixing in the Southern Ocean. *Submitted to* J. Phys. Oceanogr..

Smith, K. S. and G. K. Vallis, 2001: The scales and equilibration of mid-ocean eddies: Freely evolving flow. *J. Phys. Oceanogr.*, **31**, 554–571.

— 2002: The scales and equilibration of mid-ocean eddies: Forced-dissipative flow. *J. Phys. Oceanogr.*, **32**, 1699–1721.

Smith, W. H. F. and D. T. Sandwell, 1997: Global seafloor topography from satellite altimetry and ship depth soundings. *Science*, **277**, 1957–1962.

Solomon, A. and R. S. Lindzen, 2000: The impact of resolution on a numerical simulation of the barotropic point jet. *J. Atmos. Sci.*, **57**, 3799–3816.

Spiegel, E. A. and G. Veronis, 1960: On the boussinesq approximation for a compressible fluid. *Astrophys. J.*, **131**, 442–447.

Stammer, D., 1997: Global characteristics of ocean variability estimated from regional TOPEX/Poseidon altimeter measurements. *J. Phys. Oceanogr.*, **27**, 1743–1769.

Stammer, D. and C. W. Böning, 1992: Mesoscale variability in the Atlantic Ocean from Geosat altimetry and WOCE high-resolution numerical modeling. *J. Phys. Oceanogr.*, **22**, 732–752.

Takahashi, Y., K. Hamilton, and W. Ohfuchi, 2006: Explicit global simulation of the mesoscale spectrum of atmospheric motions. *Geophys. Res. Lett.*, **33**, L12812.

Theiss, J., 2004: Equatorward energy cascade, critical latitude, and the predominance of cyclonic vortices in geostrophic turbulence. *J. Phys. Oceanogr.*, **34**, 1663–1678.

— 2006: A generalized rhines effect on storms on jupiter. *Geophys. Res. Lett.*, **33**, L08809.

Thompson, A. F. and W. R. Young, 2006: Scaling baroclinic eddy fluxes: Vortices and energy balance. *J. Phys. Oceanogr.*, **36**, 720–738.

Treguier, A. M., I. M. Held, and V. D. Larichev, 1997: On the parameterization of quasi-geostrophic eddies in primitive equation ocean models. *J. Phys. Oceanogr.*, **27**, 567–580.

Tulloch, R. and K. S. Smith, 2006: A new theory for the atmospheric energy spectrum: Depth-limited temperature anomalies at the tropopause. *Proc. Natl. Acad. Sci. U.S.A.*, **103**, 14690–14694.

Tulloch, R. T., J. C. Marshall, and K. S. Smith, 2008: Interpretation of the propagation of surface altimetric observations in terms of planetary waves and geostrophic turbulence. *submitted to J. Geophys. Res.*.

Tulloch, R. T. and K. S. Smith, 2008a: A note on the numerical representation of surface dynamics in quasigeostrophic turbulence: Application to the nonlinear eady model. *J. Atmos. Sci.*, **In press**.

— 2008b: Quasigeostrophic turbulence with explicit surface dynamics: Application to the atmospheric energy spectrum. *J. Atmos. Sci.*, **In press**.

Tung, K. K. and W. W. Orlando, 2003a: The k^{-3} and $k^{-5/3}$ energy spectrum of atmospheric turbulence: Quasigeostrophic two-level model simulation. *J. Atmos. Sci.*, **60**, 824–835.

— 2003b: On the differences between 2D and QG turbulence. *Discrete and Continuous Dynamical Systems B*, **3**, 145–162.

Vallis, G. K., 1996: Potential vorticity inversion and balanced equations of motion for rotating stratified flows. *Quart. J. Roy. Meteor. Soc.*, **122**, 291–322.

— 2006: *Atmospheric and Oceanic Fluid Dynamics: Fundamentals and Large-Scale Circulation*. Cambridge University Press, Cambridge, U.K., 745 pp.

Vallis, G. K. and M. E. Maltrud, 1993: Generation of mean flows and jets on a beta plane and over topography. *J. Phys. Oceanogr.*, **23**, 1346–1362.

Vallis, G. K., G. J. Shutts, and M. E. Gray, 1997: Balanced mesoscale motion and stratified turbulence forced by convection. *Quart. J. Roy. Meteor. Soc.*, **123**, 1621–1652.

Vanneste, J. and I. Yavneh, 2004: Exponentially small inertia-gravity waves and the breakdown of quasi-geostrophic balance. *J. Atmos. Sci.*, **61**, 211–223.

VanZandt, T. E., 1982: A universal spectrum of buoyancy waves in the atmosphere. *Geophys. Res. Lett.*, **9**, 575–578.

Wunsch, C., 1997: The vertical partition of oceanic horizontal kinetic energy. *J. Phys. Oceanogr.*, **27**, 1770–1794.

Wunsch, C. and R. Ferrari, 2004: Vertical mixing, energy, and the general circulation of the oceans. *Annu. Rev. Fluid Mech.*, **36**, 281–314.